



UNIVERSIDADE ESTADUAL DE CAMPINAS
INSTITUTO DE QUÍMICA

IGOR MESSIAS

**STUDY OF THE CORRELATION BETWEEN ACTIVITY AND STABILITY OF
METAL OXIDES AS ELECTROCATALYSTS FOR WATER REMEDIATION**

**ESTUDO DA CORRELAÇÃO ENTRE ATIVIDADE E ESTABILIDADE DE ÓXIDOS
METÁLICOS COMO ELETROCATALISADORES NA REMOÇÃO DE
CONTAMINANTES DE ÁGUA**

CAMPINAS
2024

IGOR MESSIAS

**STUDY OF THE CORRELATION BETWEEN ACTIVITY AND STABILITY OF
METAL OXIDES AS ELECTROCATALYSTS FOR WATER REMEDIATION**

**ESTUDO DA CORRELAÇÃO ENTRE ATIVIDADE E ESTABILIDADE DE ÓXIDOS
METÁLICOS COMO ELETROCATALISADORES NA REMOÇÃO DE
CONTAMINANTES DE ÁGUA**

Tese de Doutorado apresentada ao Instituto de Química da
Universidade Estadual de Campinas como parte dos requisitos
exigidos para a obtenção do título de Doutor em Ciências.

Doctor's Thesis presented to the Institute of Chemistry of the
University of Campinas as part of the requirements to obtain the
title of Doctor in Sciences.

Supervisor: Dr. Raphael Nagao de Sousa

**O arquivo digital corresponde à versão final da Tese defendida pelo aluno Igor
Messias e orientada pelo Prof. Dr. Raphael Nagao de Sousa.**

**CAMPINAS
2024**

Ficha catalográfica
Universidade Estadual de Campinas (UNICAMP)
Biblioteca do Instituto de Química
Simone Luiz Alves - CRB 8/9094

M563s Messias, Igor, 1993-
Study of the correlation between activity and stability of metal oxides as electrocatalysts for water remediation / Igor Messias. – Campinas, SP : [s.n.], 2024.

Orientador: Raphael Nagao de Sousa.
Tese (doutorado) – Universidade Estadual de Campinas (UNICAMP), Instituto de Química.

1. Óxidos metálicos. 2. Água - Poluição. 3. Eletrocatalise. 4. Amônia. I. Sousa, Raphael Nagao de, 1984-. II. Universidade Estadual de Campinas (UNICAMP). Instituto de Química. III. Título.

Informações Complementares

Título em outro idioma: Estudo da correlação entre atividade e estabilidade de óxidos metálicos como eletrocatalisadores na remoção de contaminantes de água

Palavras-chave em inglês:

Metallic oxides

Water - Pollution

Electrocatalysis

Ammonia

Área de concentração: Físico-Química

Titulação: Doutor em Ciências

Banca examinadora:

Raphael Nagao de Sousa [Orientador]

Fabio Henrique Barros de Lima

Ana Flavia Nogueira

Murilo Santhiago

Juliano Alves Bonacin

Data de defesa: 01-08-2024

Programa de Pós-Graduação: Química

Identificação e informações acadêmicas do(a) aluno(a)

- ORCID do autor: <https://orcid.org/0000-0002-9468-6263>

- Currículo Lattes do autor: <https://lattes.cnpq.br/2992479189758358>

BANCA EXAMINADORA

Prof. Dr. Raphael Nagao de Sousa (Orientador)

Prof. Dr. Fabio Henrique Barros de Lima (Universidade de São Paulo-Instituto de Química de São Carlos)

Profa. Dra. Ana Flavia Nogueira (IQ/UNICAMP)

Prof. Dr. Murilo Santhiago (LNNANO)

Prof. Dr. Juliano Alves Bonacin (IQ/UNICAMP)

A Ata da defesa assinada pelos membros da Comissão Examinadora, consta no SIGA/Sistema de Fluxo de Dissertação/Tese e na Secretaria do Programa da Unidade.

Este exemplar corresponde à redação final da Tese de Doutorado defendida pelo aluno **IGOR MESSIAS**, aprovada pela Comissão Julgadora em 1 de agosto de 2024.

Acknowledgments

I would like to thank Prof. Dr. Raphael Nagao for his supervision and for placing his trust in me and my work. I am grateful for the valuable scientific discussions, his patience, his insightful advice, and all the opportunities he has offered me, especially for giving me the chance to perform part of my PhD at Argonne National Laboratory. I would also like to thank Dr. Pietro Papa Lopes for receiving me in his group and for his supervision during my internship at Argonne National Laboratory in the USA.

To my parents Nilceia and Luiz for all their support, for being there in good and bad times, and for being examples of ethics, responsibility, kindness, perseverance, and love. And, to my brother Lucas for the moments of relaxation and discussion.

To my Fiancé and best friend Daniele, who always helps and comforts me in difficult times, and who also is part of my best moments and brings joy to my life.

I would like to express my gratitude to all my friends and colleagues in the ElectroEnergy group, for contributing to making my PhD journey pleasurable. Specially, I would like to express my gratitude to Maria, Adriana, Gabriel, Eduardo, Matheus e Victor for all the moments of joy, relaxation, and discussion. I extend my gratitude also to my friends and colleagues from Electrochemical Materials and Interfaces group, I'm thankful for all support. I would also like to express gratitude to all the collaborators and co-authors who have generously contributed their time, expertise, and support to the projects that I have worked on during my PhD.

This study was financed in part by the Coordenação de Aperfeiçoamento de Pessoal de Nível Superior - Brasil (CAPES) - Finance Code 001.

Resumo

A contaminação da água representa uma ameaça significativa para a organismos vivos. A ampla gama de produtos químicos introduzidos por atividades agrícolas, industriais e domésticas cria um desafio na busca por métodos confiáveis para remover esses contaminantes em matrizes complexas. Superar esses desafios é crucial para garantir o fornecimento de água limpa. Métodos eletroquímicos, incluindo redução e oxidação eletrocatalíticas, oferecem vantagens, tais como configurações adaptáveis para tratar diferentes fontes de água contaminada, controlabilidade de parâmetros e capacidade de degradar contaminantes específicos. Além disso, a utilização de energia renovável para alimentar esses sistemas, combinada com a conversão de poluentes como nitrato em amônia, oferece uma solução sustentável e descarbonizada para a produção de produtos químicos. No entanto, o processo eletrocatalítico ainda sofre com baixa eficiência, o que está intimamente relacionado aos eletrocatalisadores utilizados nessas reações. Além disso, alterações na composição e estrutura desses eletrocatalisadores podem impactar significativamente seu desempenho. Portanto, entender os processos que causam essas mudanças e potencialmente levam à falha do material é crítico para melhorar as propriedades dos materiais aplicados na remediação de água. Diante disto, nesta tese, serão apresentadas algumas reações de interesse para o desenvolvimento do processo eletroquímico de limpeza de água, os estudos serão especificamente sobre a compreensão da correlação entre a atividade e a estabilidade de óxidos metálicos. Na primeira parte do trabalho, descrita no Capítulo 2, monitoramos sistematicamente as alterações dinâmicas nas características químicas e morfológicas de nanocubos de Cu_2O durante a reação de eletroredução de nitrato em eletrólito alcalino. Com base nos resultados obtidos, a atividade e a seletividade dos nanocubos de Cu_2O não está relacionada a estrutura e composição inicial. Em vez disso, a emergência de uma superfície rica em Cu-OD, que se propaga de camadas mais superficiais para camadas subjacentes ao longo do tempo, acaba desempenhando um papel crucial no mecanismo de reação. Utilizando espectrometria de massa eletroquímica diferencial online (DEMS) e espectroscopia de infravermelho por transformada de Fourier in situ (FTIR), investigamos experimentalmente a presença de intermediários chave e subprodutos da reação de redução de nitrato. No Capítulo 3, foi utilizada a técnica eletrodo rotatório de disco anel (RRDE) para identificar e quantificar a geração de espécies reativas de oxigênio (ROS) como O_3 e H_2O_2 durante a oxidação da água. Através da análise da contribuição de corrente atribuída a cada espécie em potenciais definidos, isolamos a corrente parcial dessas espécies. No Capítulo 4 investigamos a correlação entre a produção de ROS e a corrosão de óxidos metálicos. Usando

o método desenvolvido no Capítulo 3, monitoramos in situ o desprendimento de oxigênio e a produção de peróxido de hidrogênio, enquanto a estabilidade do eletrodo foi avaliada usando um eletrodo de disco rotatório estacionário (SPRDE) ligado a um espectrômetro de massa de plasma acoplado indutivamente (ICP-MS). Nossos resultados demonstram a importância de entender a relação estrutura-atividade para estrategicamente projetar novos eletrocatalisadores para limpeza de água.

Abstract

Water contamination poses a significant threat to both environmental and human health. The wide range of chemicals introduced through agricultural, industrial, and domestic activities creates a challenge in finding reliable methods to remove these contaminants in complex matrices. Addressing this challenge is crucial for ensuring a clean water supply. Electrochemical methods, including electrocatalytic reduction and oxidation, offer several advantages such as adaptable setups for different contaminated water sources, controllability, and the ability to target specific contaminants. Additionally, utilizing renewable energy to power these systems, combined with converting pollutants such as nitrate to ammonia, offers a sustainable and decarbonized approach for chemical production. However, the electrocatalytic approach still suffers from low efficiency, which is closely related to the electrocatalyst materials used in these reactions. Additionally, changes in the composition and structure of these electrocatalysts can significantly impact their performance. Therefore, understanding the processes that cause these changes and potentially lead to material failure is critical for improving the properties of material applied for water remediation. In this thesis, some reactions essential to water remediation technology will be presented, with a focus on understanding the correlations between the activity and stability of metal oxides. In the first part of the work, described in the Chapter 2, we systematically monitored the dynamic alterations in the chemical and morphological characteristics of Cu₂O nanocubes (NCs) during nitrate electroreduction reaction (NO₃RR) in alkaline electrolyte. Based on the results obtained, the activity and selectivity of the initially well-defined Cu₂O NCs are not solely dependent on the initial structure. Instead, it underscores the emergence of an OD-Cu rich surface, evolving from near-surface to underlying layers over time, playing a crucial role in the reaction pathways. By employing online differential electrochemical mass spectrometry (DEMS) and in situ Fourier transform infrared spectroscopy (FTIR) we experimentally probed the presence of keys intermediates and byproducts of NO₃RR. In Chapter 3 we used the rotating ring disk electrode (RRDE) technique to identify and quantify the generation of reactive oxygen species (ROS) such as O₃ and H₂O₂ during the water oxidation. Through an examination of the current contribution attributed of each species across defined potential we isolated the partial current of these species. In Chapter 4 we investigated the correlation between the anodic production of reactive oxygen species (ROS) and the metal oxide corrosion. Using the method developed in Chapter 3, we monitored in situ the oxygen evolution and hydrogen peroxide, while the electrode stability was accessed by using a Stationary Probe Rotating Disk Electrode (SPRDE) attached to an inductively

coupled plasma mass spectroscopy (ICP-MS). Our findings demonstrate the importance of understanding the structure-activity relationship to strategize the design of new electrocatalysts for water remediation.

List of Figures

Figure 1.1. Schematic representation of direct and indirect organic oxidation.	22
Figure 1.2. Schematic representation of reaction pathways of nitrate electroreduction. Adapted from [29].....	24
Figure 1.3 Schematic representation of lattice oxygen evolution (LOER). Adapted from [39]	27
Figure 2.1. Structural and chemical characterization of the as-prepared Cu ₂ O NCs. A) SEM image of the Cu ₂ O NCs on the glassy carbon substrate. B) Particle size histogram acquired from the FESEM image. C) Bright field HAADF-STEM image and corresponding EDS maps of D) Cu and E) O elements.	38
Figure 2.2. A) AFM image capturing a 30 μm x 30 μm section of the Cu ₂ O NCs deposited on GC. B) Raman mapping of the 224 cm ⁻¹ signal of Cu ₂ O NCs deposited on GC. C) Raman spectra of the blue, green, and red regions and the large area region analyzed. D) High-resolution Cu 2p XPS spectra of the Cu ₂ O NCs. E) GIXRD pattern of Cu ₂ O NCs deposited on FTO substrate, Cu ₂ O and SnO ₂ . Cu ₂ O peaks are labeled with corresponding plane and SnO ₂ peaks are indicated by stars.	39
Figure 2.3. NO ₃ RR electrochemical performance of Cu ₂ O NCs. A) LSV curves of GC substrate (black) and Cu ₂ O drop cast on GC (orange) in 1.0 mol L ⁻¹ NaOH (dotted line) and 1.0 mol L ⁻¹ NaOH + 14 mmol L ⁻¹ NaNO ₃ (solid line). Scan rate of 50 mV s ⁻¹ . Electrochemically active surface area (ECSA) measurements. (B) Cyclic voltammograms of Cu ₂ O NCs at different scan rates (20 to 100 mV s ⁻¹) in 1.0 mol L ⁻¹ NaOH electrolyte. (C) linear relationship (black line) for the modulus of the average of double-layer current and the scan rate.	40
Figure 2.4. Ten successive cyclic voltammograms increasing the cathodic limit without (A) and with (B) 0.1 mol L ⁻¹ NaNO ₃ (scan rate 20 mV s ⁻¹). (C) and (D) highlight the two consecutive CVs where the Cu oxidation appears for the first time without and with NaNO ₃ respectively.	41
Figure 2.5. NO ₃ RR electrochemical performance of Cu ₂ O NCs. A) Potential-dependent NH ₃ yield rate (purple line) and FE of NO ₃ RR to NO ₂ ⁻ and NH ₃ of Cu ₂ O NCs in green and orange bars in 1.0 mol L ⁻¹ NaOH + 14 mmol L ⁻¹ NaNO ₃ . B) Chronoamperometry curves 1 h longer of Cu ₂ O NCs at different applied potentials from -0.1 V to -0.6 V vs. RHE in 1.0 mol L ⁻¹ NaOH with 14 mmol L ⁻¹ of NO ₃ ⁻ under magnetic stirring at 400 rpm.	42

Figure 2.6. A) Selectivity of NO_2^- and NH_3 at different potentials. C) ^1H nuclear magnetic resonance (NMR) spectra of the electrolyte after NO_3RR over Cu_2O NCs at -0.3 V vs. RHE using $^{14}\text{NaNO}_3$ and $^{15}\text{NaNO}_3$ as the nitrogen source.	43
Figure 2.7. NO_3RR electrochemical performance of Cu_2O NCs at -0.2 V vs. RHE over 10 hours in 1.0 mol L^{-1} NaOH + 14 mmol L^{-1} NaNO_3 . At the top image the orange bars correspond to NH_3 FE while the yield rate is represented by a black line. The current density over time is represented as a black line at the bottom image.	44
Figure 2.8. Structural and chemical characterization of the post-electrolysis Cu_2O NCs in 1.0 mol L^{-1} NaOH + 14 mmol L^{-1} NaNO_3 at -0.3 V vs. RHE after 1 hour. A) FESEM image of the Cu_2O NCs on the glassy carbon substrate. B) Bright field HAADF-STEM image and corresponding EDS maps of C) Cu and D) O elements.	45
Figure 2.9. A) AFM image capturing a 30 μm x 30 μm section of the Cu_2O NCs deposited on GC. B) Raman mapping of the 224 cm^{-1} signal of Cu_2O NCs deposited on GC and C) the spectra of a specific area and the entire region analyzed. D) high-resolution Cu 2p XPS spectra. E) GIXRD pattern of Cu_2O NCs deposited on FTO substrate. Cu, Cu_2O and SnO_2 standard are shown below.	46
Figure 2.10. In situ Raman spectra A) without (potential range: 0.8 to -0.4 V vs. RHE) and B) with 0.1 mol L^{-1} of NaNO_3 (potential range: 0.8 to 0 V vs. RHE) in 1.0 mol L^{-1} NaOH electrolyte. Pink marks highlight the peaks related to Cu_2O (145 , 520 , 630 cm^{-1}) and green ones highlight peaks.	48
Figure 2.11. A) in situ FTIR spectra of Cu_2O NCs in 1 mol L^{-1} NaOH electrolyte containing 14 mmol L^{-1} NaNO_3 . The peak centered at $1,190$ cm^{-1} related to $-\text{NH}_2$ from NH_2OH and the peak centered at 1690 cm^{-1} is related to NO_x adsorbed species both are highlighted in orange) online DEMS of Cu_2O NCs recorded in 1 mol L^{-1} NaOH + 14 mmol L^{-1} NaNO_3 as electrolyte. The applied potential vs. time is represented at the top, followed by the ionic current of possible ionic fragments presents in the reaction. The $m/z = 2$ corresponds to the dihydrogen fragment, while $m/z = 17$ represents ionic fragments from NH_3 and H_2O . Additionally, $m/z = 28$ (N_2), 29 (N_2H_2 or/and N_2H_4), 30 (N_2H_x or/and NO), and 33 (NH_2OH) correspond to ionic fragments of possible intermediates of NO_3RR	51
Figure 2.12. UV-vis spectrum of ammonia quantification by chronoamperometry at -0.30 V, -0.60 V and -0.90 V vs. RHE in 1.0 mol L^{-1} NaOH and 0.20 mol L^{-1} N_2H_4	52
Figure 2.13. Possible mechanism for NO_3RR by Cu_2O NCs electrocatalyst.	53

Figure 3.1. RRDE method to determine the collection efficiency (N) for gas and liquid products in 0.1 mol L ⁻¹ NaOH, scan rate 50 mv s ⁻¹ . A) calibration for gas using HER with polycrystalline Pt and, B) the collection efficiency for different rotation rates. C) Calibration for liquid products using Fe (CN) ₆ ^{3-/4-} redox couple and D) the collection efficiency for different rates.	58
Figure 3.2. A) Cyclic voltammograms on polycrystalline Pt in O ₂ -saturated 0.1 mol L ⁻¹ H ₂ SO ₄ (green lines), O ₃ -saturated 0.1 mol L ⁻¹ (blue lines) and Ar-saturated 0.1 mol L ⁻¹ H ₂ SO ₄ + 1 mmol L ⁻¹ H ₂ O ₂ (orange lines), at different rotation rates. B) highlighted current density regions at 0.4V, 0.94V and 1.2V vs RHE at 1600RPM. Scan rate: 50 mV s ⁻¹	59
Figure 3.3. Cyclic voltammograms on polycrystalline Pt in O ₃ -saturated 0.1 mol L ⁻¹ , at different rotation rates.at 1600RPM. Scan rate: 50 mV s ⁻¹ . The plotted currents are from the subtraction from the current densities measured under O ₂ saturation.	61
Figure 3.4. Simultaneous monitoring of electrode current (top, black), O ₃ selectivity (top middle plot), H ₂ O ₂ selectivity (bottom middle plot), and O ₃ selectivity (bottom plot) during a cyclic voltammetry experiment Pt(poly) in 0.1 mol L ⁻¹ H ₂ SO ₄ electrolyte. The scan rate for both RRDE was 50 mv s ⁻¹ , the rotation rate was 900RPM.	62
Figure 3.5. A) Absolute diffusion limiting current at 0.94V vs RHE in different pH's under O ₃ saturation. B) O ₃ bulk concentration determined by the Indigo method ¹⁰⁰ in different pH's...	63
Figure 4.1. Schematic representation of the Stationary Probe Rotating Disk Electrode (SPRDE) used in this work. Adapted from [43]	70
Figure 4.2. Cyclic voltammograms in O ₂ saturated 0.1 M NaOH (dashed lines) and 0.1 mol L ⁻¹ NaOH containing 1 mmol L ⁻¹ H ₂ O ₂ (under Ar) (solid lines) using polycrystalline Pt electrode, under mass transport control.....	76
Figure 4.3. Simultaneous monitoring of electrode current (top, black), O ₂ selectivity (top, middle plots), H ₂ O ₂ selectivity (bottom middle plots), and metal dissolution rates during a cyclic voltammetry experiment on A) PbO ₂ and B) TiO ₂ , surfaces in 0.1 mol L ⁻¹ NaOH electrolyte. The scan rate for both RRDE and in situ ICP-MS were 50 mv s ⁻¹	78
Figure 4.4. Simultaneous monitoring of electrode current (top, black), O ₂ selectivity (top, middle plots), H ₂ O ₂ selectivity (bottom middle plots), and metal dissolution rates during a cyclic voltammetry experiment on A) SnO ₂ and B) FTO, surfaces in 0.1 mol L ⁻¹ NaOH electrolyte. The scan rate for both RRDE and in situ ICP-MS were 50 mv s ⁻¹	79

Figure S2.1. Custom-made experimental setup for online DEMS measurements during nitrate electroreduction studies.	94
Figure S2.2. A) UV-vis spectra of NO_2^- and NH_3 quantifications. The inserts represent the linear relationship between maximum absorbance wavelength and species concentration for NH_3 at 657 nm and NO_2^- at 540 nm.	94
Figure S2.3. SEM images of the electrocatalyst A) before and B-C) after 1-hour of NO_3RR at -0.3 V vs. RHE in $1.0\text{ mol L}^{-1}\text{ NaOH}$ with 14 mmol L^{-1} of NaNO_3 at medium and high magnification, respectively. The red arrows indicate larger nanocubes particles domains.	95
Figure S2.4. A) Normalized in situ XANES spectra of Cu_2O NCs at different applied potentials in $1.0\text{ mol L}^{-1}\text{ NaOH}$ and 14 mmol L^{-1} , and the spectra of the standards Cu and Cu_2O ; B) the corresponding first derivative curves of the in situ XANES spectra; and C) dependence of the Cu K-edge energy as a function of the electrochemical potential.	95
Figure S2.5. Online DEMS of Cu_2O NCs recorded in $0.1\text{ mol L}^{-1}\text{ NaOH} + 14\text{ mmol L}^{-1}\text{ NaNO}_3$ electrolyte. A) Applied potential vs. time. B) Ionic current vs. time of the fragment $m/z = 18$ of H_2O molecules.	96
Figure S3.1. A) UV-vis spectra of Indigo calibration curve and B) representation of the linear relationship between maximum absorbance wavelength (600nm) and species concentration.	96
Figure S3.2. Koutecky-Levich plots for O_2 , O_3 and H_2O_2 at A) 400 mV, B) 940mV, and C) 1200 mV in different rotation rates. On Pt electrode in $0.1\text{ mol L}^{-1}\text{ H}_2\text{SO}_4$ electrolyte.	97
Figure S3.3. A) Cyclic voltammograms on polycrystalline Pt in O_2 -saturated $0.1\text{ mol L}^{-1}\text{ NaHCO}_3$ (green lines), O_3 -saturated 0.1 mol L^{-1} (blue lines) and Ar-saturated $0.1\text{ mol L}^{-1}\text{ NaHCO}_3 + 1\text{ mmol L}^{-1}\text{ H}_2\text{O}_2$ (orange lines), at different rotation rates. B) highlighted current density regions at 0.4V, 0.94V and 1.2V vs RHE at 1600RPM. Scan rate: 50 mV s^{-1}	98
Figure S3.4. A) Cyclic voltammograms on polycrystalline Pt in O_2 -saturated $0.1\text{ mol L}^{-1}\text{ Na}_2\text{CO}_3$ (green lines), O_3 -saturated 0.1 mol L^{-1} (blue lines) and Ar-saturated $0.1\text{ mol L}^{-1}\text{ Na}_2\text{CO}_3 + 1\text{ mmol L}^{-1}\text{ H}_2\text{O}_2$ (orange lines), at different rotation rates. B) highlighted current density regions at 0.4V, 0.94V and 1.2V vs RHE at 1600RPM. Scan rate: 50 mV s^{-1}	98
Figure S3.5. A) Cyclic voltammograms on polycrystalline Pt in O_2 -saturated $0.1\text{ mol L}^{-1}\text{ NaOH}$ (green lines), O_3 -saturated 0.1 mol L^{-1} (blue lines) and Ar-saturated $0.1\text{ mol L}^{-1}\text{ NaOH} + 1\text{ mmol L}^{-1}\text{ H}_2\text{O}_2$ (orange lines), at different rotation rates. B) highlighted current density regions at 0.4V, 0.94V and 1.2V vs RHE at 1600RPM. Scan rate: 50 mV s^{-1}	99

Figure S4.1. Digital images of 6mm disks electrodes, with the metal oxides layer on top of the disk substrates.....	100
Figure S4.2. SEM images of PbO ₂ on the left side and TiO ₂ on the right-side surface in different magnifications.	101
Figure S4.3. SEM images of SnO ₂ on the left side and FTO on the right-side surface in different magnifications.	102

List of Abbreviations and Acronyms

PFAS	Polyfluoroalkyl Substances
ROS	Reactive Oxygen Species
EAOP	Electrochemical Advanced Oxidation Process
NO ₃ RR	Nitrate Reduction Reaction
HER	Hydrogen Evolution Reaction
FE	Faradaic Efficiency
FTIR	Fourier Transform Infrared
DEMS	Differential Electrochemical Mass Spectrometry
BDD	Boron-Doped Diamond
EPA	U. S. Environmental Protection Agency
PFOA	Perfluorooctanoic Acid
PFOS	Perfluorooctanesulfonic acid
RRDE	Rotating Ring-Disk Electrode
SPRDE	Stationary Probe Rotating Disk Electrode
ICP-MS	Inductively Coupled Plasma Mass Spectrometry
OER	Oxygen Evolution Reaction
BF-STEM	Bright Field Scanning Transmission Electron Microscopy
EDX	Energy-Dispersive X-ray
AFM	Atomic Force Microscopy
XPS	X-ray Photoelectron Spectroscopy
SEM	Scanning Electron Microscope
RHE	Reversible Hydrogen Electrode
LSV	Linear Sweep Voltammetry

ECSA Electrochemical Active Surface Area

NMR Nuclear Magnetic Resonance

XAS X-ray Absorption Spectroscopy

XANES X-ray Absorption Near Edge Spectroscopy

NCs Nanocubes

GC Glassy Carbon

GIXRD Grazing Incidence X-Ray Diffraction

ORR Oxygen Reduction Reaction

2e⁻ WOR Two-Electrons Water Oxidation Reaction

CVs Cyclic Voltammograms

LOER Lattice Oxygen Evolution Reaction

BPA Bisphenol A

MO Metal Oxide

LROS Lattice Reactive Oxygen Species

List of symbols

n	Number of electrons
F	Faraday constant
m/z	Mass-to-charge ratios
Q	Charge
N	Collection efficiency
j_{O_3}	Partial current density for ozone
$j_{H_2O_2}$	Partial current density for hydrogen peroxide
j_{O_2}	Partial current density for oxygen
C	Correction factor for current density
$\mu_{x_i}^{eq}$	Chemical potential of a reactant or product
$\Delta G_{Dissolution}^R$	Gibbs free energy for metal dissolution
ΔG_{OER}^R	Gibbs free energy for OER
ΔG_{LOER}^R	Gibbs free energy for LOER
ΔG_{ROS}^R	Gibbs free energy for ROS
ΔG_{LROS}^R	Gibbs free energy for LROS

Contents

Chapter 1: General Introduction	20
1.1. Water Contaminants and water purification processes	21
1.2. Electroreduction of nitrate to Ammonia	23
1.3. Electrochemical advanced oxidation processes (EAOP).....	25
1.4. Structure-activity relationship of electrocatalysts for water remediation.....	26
1.5. Scope of the thesis	29
Chapter 2: Electrochemical reduction of nitrate to ammonia on Cu₂O nanocubes.....	30
2.1. Introduction.....	31
2.2. Methods.....	32
2.2.1 Synthesis of Cu ₂ O nanocubes (Cu ₂ O NCs)	32
2.2.2 Characterization.....	33
2.2.3 Electrochemical Measurements	33
2.2.4 Determination of NH ₃ and NO ₂ ⁻	34
2.2.5 Calculation of faradaic efficiency and the yield rate	35
2.2.6 In situ Fourier Transform Infrared Spectroscopy	35
2.2.7 Nuclear Magnetic Resonance	36
2.2.8 In situ Raman Spectroscopy	36
2.2.9 Online Differential Electrochemical Mass Spectrometry.	37
2.2.10 In situ X-ray Absorption and Spectromicroscopy	37
2.3. Results and Discussion.....	38
2.4. Conclusions.....	53
Chapter 3:Rotating Ring disk (RRDE) approach for detection of reactive oxygen species (ROS)	54
3.1. Introduction	55

3.2. Methods	55
3.2.1 Electrochemical measurements	55
3.2.2 RRDE Collection efficiency (N) determination	56
3.2.3 Ozone quantification.....	56
3.3. Results and Discussion.....	57
3.4. Conclusions.....	63

Chapter 4: Study of Metal oxides stability during reactive oxygen species generation

(ROS)	65
4.1. Introduction.....	66
4.2. Methods.....	67
4.2.1 Metal Oxides Preparation.....	67
4.2.2 Characterization	68
4.2.3 Electrochemical Measurements	68
4.2.4 Quantification of O ₂ and H ₂ O ₂ (RRDE).....	69
4.2.5 In situ Inductively Coupled Plasma Mass Spectrometry (ICP-MS)	69
4.3. Results and Discussion.....	70
4.4. Conclusions.....	79

Chapter 5: Final Remarks

5.1. General Conclusion.....	82
References.....	84
Appendix.....	94

Chapter 1: General Introduction

1.1. Water Contaminants and water purification processes

Life is possible because of water. Throughout the development of human civilizations, ensuring access to freshwater sources has consistently been a priority concern.¹ However, the rapid growth of the population and industrial activities has led to increased contamination of drinking water.² The World Health Organization estimates that approximately 1 billion people have no access to pure water.³ Consequently, the issue of insufficient safe drinking water has become one of the most pressing concerns worldwide. Addressing this issue entails reducing the release of contaminants and implementing strategies to remediate polluted water sources.²

Contaminants have the potential to alter the physical and chemical properties of water and can be readily identified.⁴ On the other hand, certain substances may not visibly change the aspect of water yet can be harmful to humans and animals. Pesticides, drugs, various organic and inorganic compounds, as well as heavy metals, have the potential to induce diseases through their exposure and subsequent accumulation in living organisms.^{2,4} Furthermore, certain pollutants such as nitrate (NO_3^-)⁵ and the polyfluoroalkyl substances (PFAS)⁶ are non-biodegradable, resulting in their persistence and accumulation in the environment over time. This characteristic poses a significant challenge in controlling these contaminants in water, necessitating the implementation of cost-effective strategies capable of removal of these compounds. In this regard, numerous technologies have been developed, conventionally based on chemical, biological, and physical processes.⁷ Although some conventional methods based on precipitation, adsorption, filtration, and solvent extraction are effective, they are unable to degrade or repurpose these contaminants resulting in the creation of separated pollution streams.⁷ Additionally, some of these methods require chemical inputs which can address complexity to the final separation process.⁵

Sustainable water remediation aims to address these complexities by minimizing the environmental impact and promoting eco-friendly alternatives.⁸ This includes incorporating green and sustainable approaches such as using renewable energy, reducing greenhouse gas emissions, and recovering valuable resources.⁹ In this regard, electrochemical water remediation has been considered a promising technology.¹⁰ Specifically, electrocatalysis has shown significant potential.⁵ Tuning experimental conditions, such as potential and pH, in these systems can enhance selectivity and efficiency for specific reactions, thereby avoiding unwanted products. This capability makes the technology an attractive option for sustainable water remediation.^{5,10}

Unlike the conventional methods for water cleaning, electrocatalysis is capable of recycling and/or degrading a wide range of pollutants, even in trace concentrations.^{11,12} By leveraging reduction reactions at the electrode-electrolyte interface, it is possible to convert NO_3^- contaminants into ammonia (NH_3), a crucial molecule for modern society primarily used in fertilizer production. Currently, ammonia is mainly produced through the Haber-Bosch process, which has a high energy demand and a significant CO_2 footprint.^{11,13} Thus, developing a sustainable NH_3 production method presents an opportunity to decarbonize the process and reduce its environmental impact.

Electrochemical oxidation reactions also play a crucial role in removing harmful pollutants, employing both direct oxidation at the electrode surface and indirect oxidation mediated by in-situ generated reactive oxygen species (ROS) through water splitting (Figure 1).¹⁴ This last approach is classified as an Electrochemical Advanced Oxidation Process (EAOP).⁷ In EAOP, highly reactive radicals, such as hydroxyl radicals ($\bullet\text{OH}$), are produced.¹⁵ These radicals possess high oxidative power, enabling them to degrade a wide range of persistent organic pollutants, including PFAS substances, into less harmful compounds.¹⁶ Additionally, through these oxidative reactions microplastics in water streams can be removed and repurposed.¹⁷ The electrochemical depolymerization process can generate a broad spectrum of monomers and dimers, which can be utilized as feedstocks for chemical synthesis, for example.¹⁸ This approach provides an electrified pathway to chemicals production.¹⁹

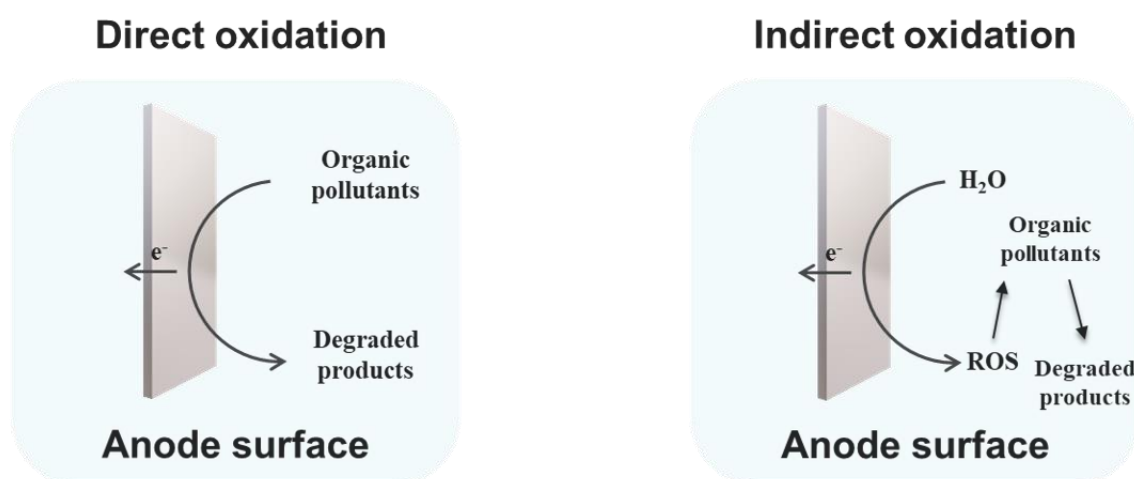


Figure 1.1. Schematic representation of direct and indirect organic oxidation.

Together, the understanding of electrochemical reduction and oxidation processes can offer a sustainable approach to water purification. This strategy not only addresses the urgent

need for cleaner water but also contributes significantly to reducing the environmental footprint of conventional processes. As such, advancing these electrochemical technologies holds great promise for achieving a more sustainable and environmentally friendly future.

1.2. Electroreduction of nitrate to Ammonia

The intensive use of nitrogenous fertilizers has disrupted the nitrogen cycle, as indicated by the accumulation of nitrate in water streams, leading to harmful consequences for both the environment and human health.²⁰ The electrochemical nitrate reduction reaction (NO₃RR) is acknowledged as a sustainable approach for reducing nitrate levels in contaminated water.^{21,22} Considering the increasing efforts to enable the use of renewable sources for electrical energy, electrochemical water remediation is a promising alternative to convert contaminants from polluted water to valuable products, especially ammonia (NH₃).^{13,23} Furthermore, NO₃RR to NH₃ is advantageous considering that ammonia can be used as an energy carrier due to the hydrogen content or even offer a decarbonized path for fertilizer production.^{24,25}

The conversion of nitrate to the main desired product NH₃ is a complex process involving the transfer of eight electrons for both deoxygenation and protonation of the nitrate.²⁶ The faradaic efficiency for NH₃ depends on the relative rates of side reactions that can convert NO₃⁻ to NO₂⁻, NO, NH₂OH, N₂O, or N₂ (Figure 2).²⁷ Additionally, at sufficiently high overpotentials the hydrogen evolution reaction (HER) can also occur, further diminishing the NO₃RR faradaic efficiency.²⁸ In terms of practical applications, this is a critical limitation due to HER being favored at the small nitrate concentration range (5-30 ppm) in real polluted sources.⁵ In this scenario, electrocatalyst engineering should consider the energy and reaction rates of the intermediates involved in these reactions to design materials that demonstrate enhanced selectivity for NO₃RR over HER.

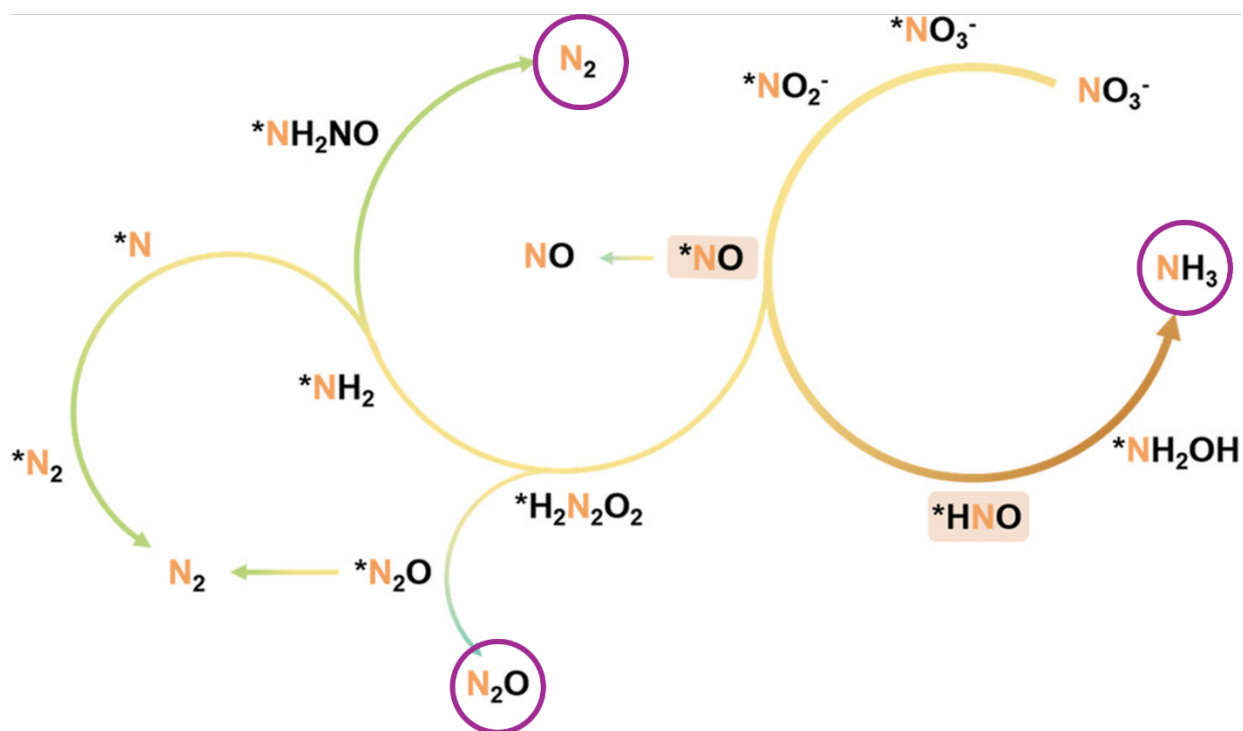


Figure 1.2. Schematic representation of reaction pathways of nitrate electroreduction. Reproduced with permission from [29]. Copyright 2023, Wiley–VCH.

Based on the on the nitrate reduction reactions (NO₃RR) activity, studies using copper (Cu) based materials have demonstrated high Faradaic efficiency (FE) for NH₃ production, a crucial molecule for modern society.²⁹ However, the NH₃ yield rate from NO₃RR remains insufficient compared to that achieved by the industrial Haber-Bosch process.²¹ This highlights the necessity for a fundamental understanding of the structure-activity relationship to guide the next steps in the sustainable production of ammonia. Such an understanding is essential for validating the feasibility of scaling up NO₃RR for industrial applications. To depict the reaction pathway, followed by theoretical simulations, in situ characterization methods such as in situ Raman spectroscopy,³⁰ in situ Fourier transform infrared (FTIR) spectroscopy,³¹ and online differential electrochemical mass spectrometry (DEMS)³² have been employed to monitor the electrode-electrolyte interface. Though these coupled techniques certain reaction intermediates, such as hydroxylamine (NH₂OH), can be identified, indicating possible mechanistic routes for the conversion of nitrate to ammonia.^{30,31} Additionally, the understanding of the dynamic evolution of the electrocatalyst is as important as the understanding of the reaction pathways, combined these two aspects play a crucial role in the selectivity and energy efficiency of the process.³⁰

1.3. Electrochemical advanced oxidation processes (EAOP)

As mentioned in section 1.1 Electrochemical advanced oxidation processes (EAOPs) have gained attention as a powerful technology for treatment of complex waste streams. The in-situ generation of ROS through the water oxidation on the anode surface represents an advantage over the conventional AOP, where is necessary the external input of O_3 or H_2O_2 is necessary to generate $OH\cdot$ radicals, for example.³³ Thus, AOP addresses capital and operating costs and is less effective in real water matrixes due to the presence of $\cdot OH$ scavengers. Among the active materials for ROS production, PbO_2 , SnO_2 TiO_2 and boron-doped diamond (BDD) are some of the more utilized. Comninellis et al.³⁴ classified these types of electrodes as “non-active” where the “active oxygen” species are physisorbed and are capable of nonselective oxidize organics more efficiently than the “active” electrodes. The “active” electrodes such as RuO_2 , IrO_2 , Pt, can access higher oxidation states thus when absorbed hydroxyl radicals interact with the anode, it changes the oxidation state. This resultant surface acts as mediator for the selective oxidation of organics. However, even the “non active” electrodes during the potential driven are susceptible to loss efficiency due the competing reactions such as OER.³⁴

Some of these oxides such as SnO_2 and TiO_2 presents low conductivity which can be improved by doping. However, some dopants can represent a concern in terms of toxicity. For example, a common dopant for SnO_2 electrode is Sb which is regulated by the U. S. Environmental Protection Agency (EPA) and its limit in drinking water is $6 \mu g L^{-1}$.³³ The environmental concern also extends to the use of PbO_2 as an electrode, as the EPA regulates a maximum limit of $15 \mu g L^{-1}$ of lead in drinking water.³³ Although experimental data show that Pb ion leaching is minimal,³⁵ it can still affect long-term operational applications. Hence, understanding the structural dynamics of these electrodes, which can release toxic metals into the environment, is critical to prevent an increase in water contamination levels.

Mass transport is one of the main limitations of the process, due to the trace concentration of certain pollutants, side reactions are favorable. To mitigate the diffusional limitations research has focused on the use of flow-systems. Le et al.³⁶ applied a Magnéli phase Ti_4O_7 reactive electrochemical membrane to oxidize Perfluorooctanoic acid (PFOA) and perfluorooctanesulfonic acid (PFOS). The contaminants were oxidized as they flowed throupermeatingembrane, achieving removal rates of approximately $3415 \pm 203 \mu mol m^{-2} h^{-1}$ for PFOA and $2436 \pm 106 \mu mol m^{-2} h^{-1}$ for PFOS at a permeate flux of $720 L m^{-2} h^{-1}$. This

demonstrates that the development of flow-through electrodes is an alternative with significant potential for advancing water treatment.³⁶

Another important parameter is the performance of the system, in order to avoid negative environmental impacts. Matrix effects, byproducts formation and electrode degradation are some variables that are prone to reduce the effectiveness of the technology.³³ Thus, research is needed to acquire fundamental information under operational conditions and apply this understanding to mitigate environmental impacts, thereby making EAOP technology economically competitive.

1.4. Structure-activity relationship of electrocatalysts applied for water remediation

Understanding the activity and stability of materials used in water remediation is fundamental for rational system design. The identity of the electrocatalyst and the number of active sites dictate the material's efficiency and selectivity. However, during operational conditions dynamic changes in the structure and composition will impact on the nature and availability of these actives' sites.³⁷ For example, during nitrate electroreduction to ammonia on 100 and 111 rich Cu_2O surfaces Anastasiadou and co-workers³⁸ identified that the catalyst suffers dissolution and redeposition process, leading to a significant surface reconstruction into nanoneedles after 3h operation. Another example comes from anodes for oxidation reactions. There are experimental and theoretical evidence that the OER mechanism is linked thermodynamically with the dissolution process of the catalyst, which causes the metal corrosion (Figure 3).³⁹⁻⁴¹

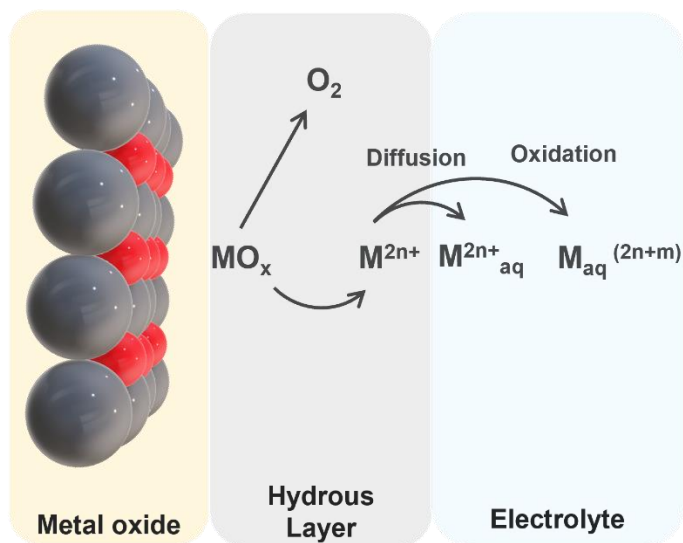


Figure 1.3 Schematic representation of lattice oxygen evolution (LOER). Adapted from [39]

These examples underscore the critical need to understand the impact changes on the electrocatalyst that can significantly impact reactions pathways. Since, changes in the electrocatalyst due to dissolution and redeposition processes can lead to the alteration or loss of active sites, potentially causing the electrocatalyst failure.³⁷ Predicting how and when these changes will affect the catalyst performance is challenging, as it is highly dependent on the specific experimental conditions of each system.³⁷ To address this, ex-situ and in-situ techniques should be combined to gain comprehensive insights into the behavior and stability of electrocatalysts.^{30,37} Ex-situ techniques allow for detailed characterization of the catalyst structure and composition before and after electrochemical testing, providing valuable information on morphological and structural changes, as well as detecting the formation of reactional products and by-products. On the other hand, in-situ techniques enable real-time monitoring of the electrocatalyst and reactional intermediates under operating conditions, capturing transient reactions that are crucial for understanding the relationship between activity and stability.^{42,43} For example, combining mass spectrometry with an electrochemical cell allows probing the formation of gaseous or volatile species during CO₂ reduction, which is important for mechanism determination.⁴⁴ Another example relies on the catalyst stability, which though ICP-MS is possible to accessed time resolved dissolution rate of electrocatalyst applied for different reactions.^{43,45}

Since most of the online and in-situ approaches are custom-made, a detailed description of how the electrochemical experiments were coupled with the analytical techniques will be provided in the experimental section of chapter 2 and 3.

1.5. Scope of the thesis

As discussed above, understanding activity-stability trends of electrocatalysts applied for water cleaning could aid in developing materials with better performance, making the technology economically viable and competitive with conventional methods. Additionally, this technology has the potential to serve as a sustainable method for producing valuable molecules, thereby helping to decarbonize processes. In this context, the main goal of this work is to study how reductive and oxidative electrochemical reactions, important for water remediation processes, impact electrocatalysts, particularly metal oxide. Despite electroreduction and electrooxidation reactions having related challenges, these are distinct processes. Therefore, the work presented will be divided into three chapters. The first will be related to the electroreduction of nitrate to ammonia on Cu_2O nanocubes. The goal was to investigate how changes in the structure and composition of the pristine catalyst affect the selectivity for ammonia production. To achieve this, we employed a combination of ex-situ and in-situ characterization techniques to probe the evolution of the electrocatalyst during the reaction. To analyze the molecular aspects, we used online DEMS to track reaction intermediates and obtain information about possible reaction pathways.

The second and the third part (chapter 3 and 4) are closely related. Chapter 3 will describe the development of a rotating ring-disk electrode (RRDE) method designed to differentiate between the production of O_2 , O_3 , and H_2O_2 during water oxidation in different electrolytes and pH conditions. The third part (Chapter 4) of this work will focus on studying the electrochemical generation of reactive oxygen species (ROS) by applying the method developed in Chapter 3 to metal oxides that are less active for oxygen evolution reaction (OER). Additionally, we will track the stability of these electrocatalyst by using a Stationary Probe Rotating Disk Electrode (SPRDE) coupled with ICP-MS, which allowed us to measure metal corrosion over time during ROS production. By assessing this information, we aim to validate whether the thermodynamic correlation between OER and metal corrosion extends to ROS generation.

**Chapter 2: Electrochemical reduction of nitrate to ammonia on Cu₂O
nanocubes**

2.1. Introduction

Copper (Cu) is an earth-abundant catalyst that has high activity and selectivity for NH₃ production, outperforming other transition metals, such as nickel, cobalt, and iron.⁴⁶⁻⁴⁸ This is due to the similarity between the energy levels of the d-orbital on Cu and the LUMO π^* of NO₃⁻. However, the hydrogen supply on the copper surface is proposed to be a limiting step for the follow hydrogenation of intermediates (e.g., *NO₂ and *NO), particularly at low overpotentials.⁴⁹ Nevertheless, pure Cu electrodes exhibit a considerable affinity for certain intermediates such as NO₂⁻ and NO, which causes surface poisoning.⁵⁰ As a result, an overpotential is required to overcome this barrier and fully convert NO₃⁻ to NH₃. Cu's performance has been improved though alloying Cu with catalytically active elements, such as Ni⁴⁶ and Sn⁵¹, or/and wrapping onto substrates (graphitized carbon⁵² and covalent triazine framework)⁵³. The Cu oxidation state also plays an important role in the efficiency of NH₃ production. Copper oxide-based catalysts have been shown to be more efficient at NO₃RR to ammonia. However at the operational pH and potential conditions proposed in the literature is expected that the oxide species are reduced to metallic Cu.⁵⁴ Several studies showcase the effectiveness of employing Cu/Cu₂O mixed phases to enhance the selectivity toward ammonia.^{32,55-57} The heightened performance is predominantly ascribed to the diminished energy barrier for *NO₃H and *NO₂H hydrogenation facilitated by Cu⁺ sites. However, these oxidized states (Cu²⁺/Cu⁺) are unstable during the NO₃RR being mostly converted to Cu⁰.⁵⁷ Throughout this process, structural changes may occur because of lattice oxygen loss, resulting in defects formation in the catalyst structure.³¹ Consequently, deformations in the regular arrangement of Cu atoms in the crystal lattice would impact the electronic structure of the catalyst surface, changing the energy associated with the adsorption and desorption processes.^{50,58,59} Therefore, a significant open question in the literature is whether the synthesized catalyst maintains its surface properties (such as morphology and chemical composition) during NO₃RR. In this sense, we have recently investigated the change in Cu₂O catalyst's oxidation state under NO₃RR conditions and the oxygen vacancies on the catalyst surface was attributed as the active site that boosts ammonia formation from -0.60 to -0.77 V vs. SHE, and at higher overpotentials (-1.10 V vs. SHE) Cu⁰ itself is the active site.³¹

The Cu oxide-based materials' structure activity/stability relationship towards NO₃RR is an important factor for NH₃ production. Considering Cu⁰ surface, previous experimental and theoretical works have demonstrated that the selectivity of ammonia reaction pathways depends on the Cu catalyst crystal orientation.^{26,60-62} Specifically, the atomic arrangement (111), copper's

most stable exposed surface, exhibits enhanced selectivity for ammonia over the (100) surface in neutral and alkaline electrolytes.^{26,60} This observation is associated with the larger free energy of H₂ than any step for NO₃RR.²⁶ In terms of kinetics, the improved performance of Cu(111) surfaces is linked to the lower overpotential to convert NO₃⁻ to NO₂⁻ than the (100) arrangement.²⁶ In contrast, certain reports attribute the higher ammonia selectivity to greater exposure of Cu(100) facets, thus the higher rate to convert NO₂⁻ to NH₂OH than the Cu(111).^{60,61,63} Considering these statements, the performance of Cu oxide-based catalysts featuring a preferential orientation, which are prone to structural changes induced by cathodic potential, would not be linked to the pristine catalytic surface. Instead, it could be closely tied to the reconstructed surface, leading to a misinterpretation of the reaction pathways. Consequently, there is a growing interest in comprehending the dynamic evolution of the Cu structure under operational conditions.^{38,49,64} It is crucial to unveil the relationship between activity and stability to design surfaces that demonstrate improved performance while maintaining their stability for the electrochemical reduction of nitrate to ammonia.

Herein, we provide a systematic experimental approach to understanding the structural and compositional evolution of a well-defined nanostructured Cu oxide-based catalyst during the nitrate electrochemical reduction to ammonia. We synthesized Cu₂O nanoparticles with cubic shape using a wet-chemical ligand-free method and tested their performance towards NH₃ production in an alkaline electrolyte. We showed that the catalyst presented a FE to ammonia of ~93% at -0.3 V vs. RHE. By combining in situ and ex situ techniques in the electrochemical experiments, we evaluate the impact of compositional and morphological changes of Cu₂O nanocubes surface on the intermediates distribution for ammonia production. Regarding stability, the catalyst maintained a high selectivity toward ammonia over 10 h electrolysis at -0.2 V vs. RHE. We also tracked the presence of key reaction intermediates with in situ FTIR and volatile products with the online DEMS to investigate the reaction mechanism. We found that NH₃ is mainly formed through NO hydrogenation, which leads to the formation of NH₂OH, furtherly converted into NH₃.

2.2. Methods

2.2.1 Synthesis of Cu₂O nanocubes (Cu₂O NCs)

The ligant-free Cu₂O nanocubes were prepared following the Herzog, A. *et al.*, 2021 work.^[1] First, 5 mL of a CuCl₂ solution (0.1 mol L⁻¹) and 15 mL of a NaOH solution (0.2 mol L⁻¹) were diluted in 200 mL of ultrapure and kept under magnetic stirring (500 rpm) for 5 minutes. Then 10 mL of an L-ascorbic acid solution (0.1 mol L⁻¹) was added to the mixture, and the solution was stirred for 60 minutes. To remove the unreacted chemicals and the OH⁻ excess the solution was washed and centrifuged three times, including two with an ethanol-water mixture (1:1) and one with pure ethanol. The resulting precipitate was then re-suspended in 10 mL of ethanol, resulting in a Cu₂O loading of 2 mg mL⁻¹.

2.2.2 Characterization

Particle morphology and chemical composition were determined by bright-field scanning transmission electron microscopy (BF-STEM) coupled with energy-dispersive x-ray (EDX) mapping in a FEI Titan Cubed Themis microscope (These measurements were conducted at Brazilian Nanotechnology National Laboratory (LNNano)). FEG-SEM micrographs were acquired in a FEI Quanta 250 microscope operating at 20.00 kV. The topography of the samples was examined with a FlexAFM with C3000 controller (Nanosurf, Switzerland) operating under dry atmosphere and with a Pt/Ir coated tip (EFM tip, Nanoworld, Switzerland), resonance frequency of 75 kHz and a constant force of 2.8 N m⁻¹. Surface composition was determined by X-ray Photoelectron (XPS)) (These measurements were conducted at Brazilian Nanotechnology National Laboratory (LNNano)) and the spectra were acquired in a Thermo Scientific K-alpha spectrometer (Al K α gun source, 300 μ m spot size, 50.0 eV pass energy, and 0.100 eV step size. Raman spectra and spectral images were collected in a Witec Alpha 300 micro-Raman confocal microscope (532 nm excitation laser and 20x objective lens)) (These measurements were conducted at University of Maringá). For the XPS and GIXRD characterization, Cu₂O NCs were drop-casted onto FTO substrate and dried in vacuum prior to the analysis (in the case of the pristine sample). The post-electrolysis sample was first washed with MilliQ water and then dried (in vacuum) before characterization. X-ray patterns were acquired in a Bruker D8 Advance Eco diffractometer (Cu K α , 8 keV).

2.2.3 Electrochemical Measurements

The electrochemical measurements were conducted by a Metrohm Autolab PGSTAT302N electrochemical workstation in a 2-compartment (H-type). The anodic and

cathodic compartments were separated by a Fuel Cell Store Fumasep FAB-PK-130 membrane. For the preparation of Cu₂O NCs working electrodes, 20 μL of the solution containing 2 mg mL^{-1} of the nanoparticles and 1% v/v of a NafionTM 5 wt% solution was drop-casted on a 5 mm diameter (0.196 cm^2 area) glassy carbon disk. The reference electrode was the reversible hydrogen electrode (RHE) and a platinum mesh (1.0 x 1.0 x 0.01 cm) counter electrode. To avoid any interference by changes in the bulk electrolyte pH a solution of 15 mL of a 1.0 mol L^{-1} NaOH was used in both cell compartments. Both compartments were degassed with ultra-high purity argon. To perform the nitrate reduction study, the linear sweep voltammetry (LSV) and chronoamperometry (CA) experiments were conducted by adding into the cathode compartment 14 mmol L^{-1} of nitrate. The potentiostatic test was carried out at different potentials (-0.2 to -0.6 V vs. RHE) for 1 h under a mass transport control with a rotation rate of 400 rpm. Chronoamperometric stability test was conducted at -0.2 V vs. RHE in 5 consecutive 2-h electrolysis in NaOH 1 mol L^{-1} and NaNO₃ 14 mmol L^{-1} . At each electrolysis, the electrolyte was collected for product quantification and renewed. During the electrolyte exchange, no potential was applied, and the electrode was minimally exposed to air. The electrochemical active surface area (ECSA) was determined using the double-layer capacitance (C_{dl}) (Figure S1), which was measured by cyclic voltammetry (CV) in the range of 20-100 mV s^{-1} in a non-faradaic potential region. The C_{dl} was obtained from the plot of current density against scan rate. Thus, the ECSA can be calculated according to the Equation 1:

$$\text{ECSA} = C_{dl} / C_s \quad (1)$$

The specific capacitance (C_s) for a flat surface is generally in the range of 20-60 $\mu\text{F cm}^{-2}$.²¹ In our work, we used it as 40 $\mu\text{F cm}^{-2}$.

2.2.4 Determination of NH₃ and NO₂⁻

The ultraviolet-visible (UV-vis) spectrophotometer was used to detect the ions in the electrolyte as reported by Costa et. al.³¹ NH₃ quantification was conducted using the indophenol blue method. 500 μL of the samples were in 2.5 mL of water. Then, 500 μL of an alkaline sodium salicylate solution (0.3 mol L^{-1} NaOH and 0.4 mol L^{-1} sodium salicylate), 50 μL of 1% sodium nitroprusside (1 % wt), and 50 μL of NaClO were added. The sample spectra were taken

from 500 to 800 nm and the maximum absorbance peak was identified at 657 nm. Nitrite was quantified by the Griess method. In detail, 500 μL of the sample was diluted with 2.5 mL of water and 1 mL of a chromogenic agent (Griess reagent) composed of 0.1 g of N-(1-naphthyl) ethylenediamine hydrochloride, 1.0 g of sulfanilamide, 2.94 mL of H_2PO_4) in 50 mL of was added. For nitrite detection, the UV-vis spectra were acquired in the range of 400 to 700 nm, and the wavelength at 540 nm was chosen to determine the sample concentration.

2.2.5 Calculation of faradaic efficiency and the yield rate

The Faradaic efficiency was measured by the charge consumed for produced ammonia and nitrite according to Equation 2:

$$FE = \frac{n \times F \times c \times V}{i \times t} \cdot 100\% \quad (2)$$

The yield of NH_3 was calculated using the Equation 3:

$$\text{Yield}_{\text{NH}_3} = \frac{c_{\text{NH}_3} \times V}{M_{\text{NH}_3} \times t \times m} \cdot 100\% \quad (3)$$

Where n is the number of electrons transferred (8 for NH_3 and 2 for NO_2^-), F is the Faraday constant (96500 C mol^{-1}), c is the concentration in mol L^{-1} , V is the catholyte volume (0.015 L), i is the total current, t is the electrolysis time, M_{NH_3} represents the ammonia molar mass and m is the catalyst loading on the electrode surface.

2.2.6 In situ Fourier Transform Infrared Spectroscopy

In situ Fourier Transform Infrared Spectroscopy (FTIR) experiments were carried out in a custom-made spectro-electrochemical cell (SEC) assembled on top of a CaF_2 window lined up on the top of a specular reflection accessory (Pike Technologies, model VeeMax II). The instrument used was a Shimadzu IR prestige-21 spectrometer equipped with a mercury-cadmium-telluride (MCT) detector refrigerated with liquid nitrogen. Platinum wire was used as a counter electrode and a reversible hydrogen electrode (RHE) as a reference. The working electrode (WE) was Cu_2O NCs deposited on a glassy carbon disk as described in the previous section ($d = 5 \text{ mm}$). The WE were assembled into the cell and pressed against the CaF_2 window to create a thin layer. The spectra were collected during chronoamperometry measurements in $1.0 \text{ mol L}^{-1} \text{ NaOH}$ and $20 \text{ mmol L}^{-1} \text{ NaNO}_3$ from 0.3 to -0.9 V vs. RHE with 100 mV intervals.

The FTIR spectra were obtained by external reflection from an average of 128 scans with a resolution of 4 cm^{-1} at each potential.

2.2.7 Nuclear Magnetic Resonance

$^{14}\text{NH}_4^+$ and $^{15}\text{NH}_4^+$ were quantified by ^1H Nuclear Magnetic Resonance (NMR). After 1 h longer electrolysis at -0.4 V vs. RHE , an aliquot of the electrolyte was collected and acidified to $\text{pH} = 3$ to ensure the conversion of all NH_3 to NH_4^+ . Then, $550\ \mu\text{L}$ was transferred to a 5 mm NMR tube, and $100\ \mu\text{L}$ D_2O was added to adjust the lock of the spectrometer. The ^1H NMR measurements were performed at room temperature on a Bruker AVANCE III NMR spectrometer, operating at 11.7 Tesla, observing ^1H nuclei at 500.13 MHz. The instrument was equipped with a direct detection probe. The ^{15}N isotope-labeling nitrate reduction experiments were conducted to validate that ammonia formation is exclusively fueled by the nitrate source. These experiments were analogous to the ^1H NMR procedure mentioned earlier, with the exception being the utilization of $\text{Na}^{15}\text{NO}_3$ (98 atom% ^{15}N) as the nitrate source. The spectra of ^1H NMR were acquired using pulse sequence zgpg30 (Bruker library) using the following parameters: 2s relaxation delay (d1), 4 dummy scans (ds), 1 k transients (ns), 4.089 s acquisition time, 64 k data points distributed over 8012 Hz spectral width. The spectra were processed by the application of an exponential multiplication free induction decay (FID) with a line broadening factor of 0.3 Hz, followed by Fourier transform with zero filling by a factor of 2.

2.2.8 In situ Raman Spectroscopy

In situ Raman spectroscopy was performed in a Renishaw InVia microscope (These measurements were conducted at University of Michigan), with a 633 nm laser. The spectro-electrochemical cell was assembled on top of a quartz window, in a three-electrode configuration cell: Cu_2O NCs ink ($40\ \mu\text{L}$) drop casted on Au (0.385 cm^2) as the working electrode, a platinum wire as a counter electrode, a leakless Ag/AgCl as a reference electrode. The spectrums were collected during chronoamperometry measurements in a 1.0 mol L^{-1} NaOH electrolyte with and without 0.1 mol L^{-1} NaNO_3 from 0.8 to -0.4 V vs. RHE with 100 mV steps. In situ Raman spectra were obtained by the accumulation of 16 scans, with 100% laser power, and 1 s exposure time.

2.2.9 Online Differential Electrochemical Mass Spectrometry.

Online Differential Electrochemical Mass Spectrometry (DEMS) experiments were conducted by coupling chronoamperometry (CA) measurements to the mass spectrometer to track possible gaseous or volatile species by their ionic currents of mass/charge (m/z) ratios generated along the electrochemical nitrate reduction in a potential range from -0.3 to 0.8 V *vs.* RHE. The DEMS setup consists of a two-stage differential pumping system, featuring two chambers with turbomolecular pumps, supported by one or more multistage root dry pumps or rotary vane pumps, which together form the high-vacuum system.⁴² The possible ionic species monitored were hydrogen (H_2), ammonia (NH_3), nitrogen (N_2), Diazenylium (N_2H), nitric oxide (NO), and hydroxylamine (NH_2OH) at $m/z = 2, 17, 28, 29, 30,$ and $33,$ respectively. The working electrode was 100 μL of the Cu_2O NCs ink drop casted on a carbon cloth (thickness of 410 μm from Fuel Cell Store) and a PTFE membrane (Gore-Tex, 0.02 μm pore size and 50 μm thickness) underneath, attached to a holder (PTFE), which was screwed to the stainless-steel flange and placed inside based on a custom-made electrochemical cell (Figure S2.1).⁴² The transport of species from the electrode/electrolyte interface to the high-vacuum system occurs through the vapor phase, driven by the pressure drop across the membrane interface.⁴² The exposed area of the working electrode to the solution was 0.38 cm^2 in all experiments. A platinum mesh and a reversible hydrogen electrode (RHE) were used as counter and reference electrodes, respectively. The experiments were conducted under Ar-saturated solutions kept under magnetic stirring (700 rpm). The electrolyte was 1.0 mol L^{-1} NaOH and 100 mmol L^{-1} of $NaNO_3$. Therefore, all reported ionic current values are relative and refer to changes from the initial baseline levels observed during the applied potential.

2.2.10 In situ X-ray Absorption and Spectromicroscopy

Synchrotron experiments were carried out at beamline Carnaúba/Sirius, at Tarumã station, using a beam size of 200 nm x 500 nm (nanoprobe) with an estimated flux of about 109 photons/second on the sample. Punctual in situ X-ray absorption spectroscopy (XAS) experiments were performed using a four-bounce Si(111) monochromator with energy resolution of 10^{-4} at a step of 0.5 eV. The punctual spectra and XANES maps were collected during chronoamperometry measurements with electrolyte containing 1.0 mol L^{-1} NaOH and 0.1 mol L^{-1} $NaNO_3$ from -0.4 to -1.0 V *vs.* RHE (at every 200 mV) using EC301 potentiostat

from Stanford Research Systems. For each measurement, the potential was applied for 10 minutes before the spectra acquisition.

2.3. Results and Discussion

2.3.1 Synthesis and Characterization of Cu₂O Nanocubes

Our as-prepared catalysts have a cubic shape and are predominantly in the Cu₂O phase. We synthesized Cu₂O nanocubes (NCs) by reducing copper chloride in a basic medium using ascorbic acid as the reducing agent.⁶⁵ We confirmed the cubic morphology of the particles (Figure 2.1A) through scanning electron microscopy (SEM). By counting the size of 100 particles, the size distribution revealed an average size of 48.0 ± 13.2 nm, as illustrated in the histogram (Figure 2.1B). Examining bright field high-angle annular dark-field scanning transmission electron image (BF-STEM, Figure 2.1C) and elemental mapping, we verified the homogeneous distribution of the elements Cu and O over the catalyst structure (Figure 2.1D-E).

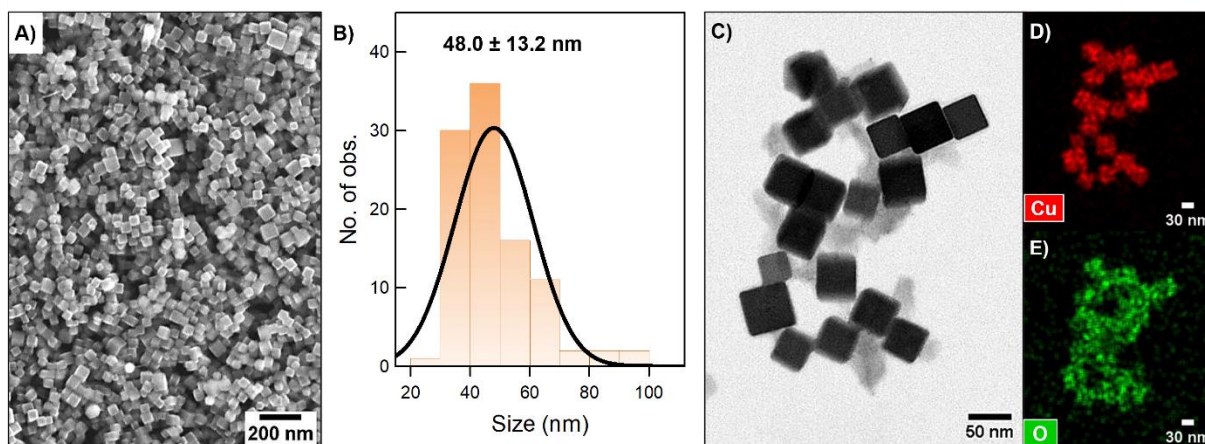


Figure 2.1. Structural and chemical characterization of the as-prepared Cu₂O NCs. A) SEM image of the Cu₂O NCs on the glassy carbon substrate. B) Particle size histogram acquired from the FESEM image. C) Bright field BF-STEM image and corresponding EDS maps of D) Cu and E) O elements.

Figure 2.2A displays the atomic force microscopy (AFM) measurement of a select area of the catalyst on the glassy carbon (GC) substrate. The micrograph revealed a homogeneous dispersion of the catalyst as a layer with approximately 0.60 μm height. To access the chemical state of the Cu₂O NCs and their surface composition we employed Raman spectroscopy and

XPS. The signal at 224 cm^{-1} is assigned to a characteristic second-order Raman-allowed mode of Cu_2O and Figure 2.2B shows the signal intensity distribution over a $30\text{ }\mu\text{m} \times 30\text{ }\mu\text{m}$ area from a fresh Cu_2O electrode is displayed. The spectrum of the colored regions in red, green, and blue are shown in Figure 2.2C in the same colors. Additionally, the spectrum of the total probed area is represented in black. The characteristic Cu_2O band (224 cm^{-1})⁶⁶ was observed in the green to red regions and especially in the large area spectra, as well as the D band of the glassy carbon substrate at 1359 cm^{-1} .⁶⁷ Figure 2.2D depicts the high-resolution Cu 2p XPS spectra, revealing two peaks attributed to Cu^+ (932.5 and 952.1 eV) and Cu^{2+} (at 934.1 and 954.0 eV).³² The presence of the Cu^{2+} oxidation state on the catalyst's surface would be related to the unavoidable air exposure of the sample during the transportation to the XPS analysis.³⁸ To confirm the crystalline phase of the as-prepared catalyst, we utilized ex situ grazing incidence X-ray diffraction (GIXRD) patterns. The X-ray diffraction spectra (Figure 2.2E) show characteristic peaks centered at $2\theta = 29.4, 36.3, 42.2, 61.3, 73.4,$ and 77.4° , attributed to the (110), (111), (200), (220), (311) and (222) planes of Cu_2O respectively. All the diffraction peaks are consistent with the Cu_2O crystal structures pattern. The remaining peaks in the spectra were attributed to the FTO substrate based on the SnO_2 crystal structure pattern.

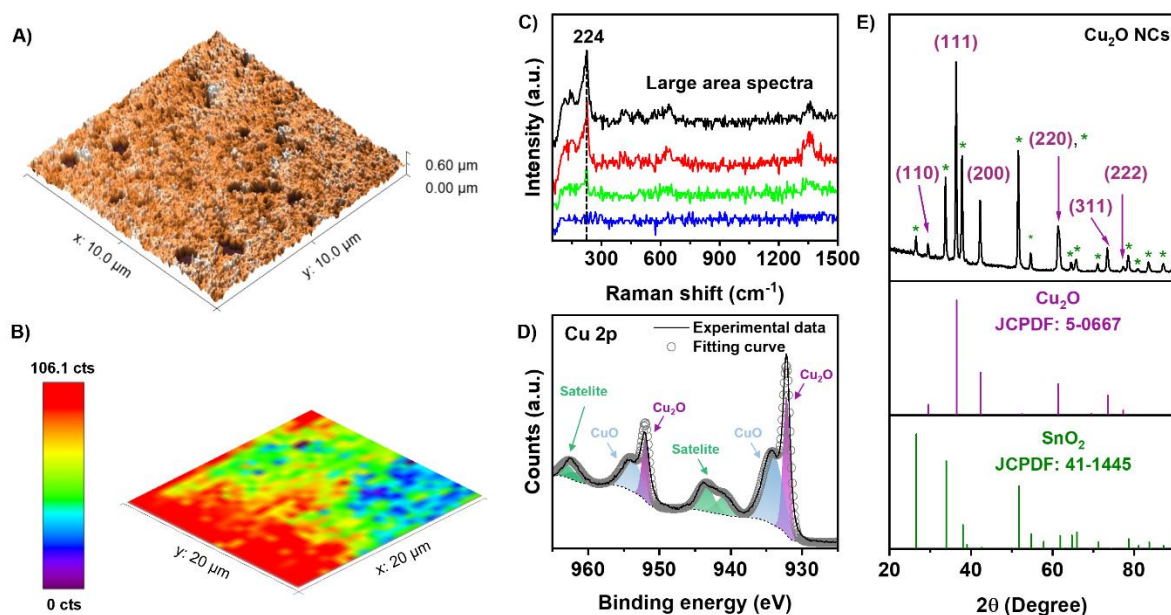


Figure 2.2. A) AFM image capturing a $30\text{ }\mu\text{m} \times 30\text{ }\mu\text{m}$ section of the Cu_2O NCs deposited on GC. B) Raman mapping of the 224 cm^{-1} signal of Cu_2O NCs deposited on GC. C) Raman spectra of the blue, green, and red regions and the large area region analyzed. D) High-resolution Cu 2p XPS spectra of the Cu_2O NCs. E) GIXRD pattern of Cu_2O NCs deposited on FTO substrate, Cu_2O and SnO_2 . Cu_2O peaks are labeled with corresponding plane and SnO_2 peaks are indicated by stars.

2.3.2 Electrochemical Performance for Nitrate Reduction Reaction

To investigate the electrocatalytic activity of NO₃RR to NH₃, we conducted LSV and chronoamperometry experiments using a glassy carbon electrode modified with Cu₂O NCs as the working electrode. Figure 2.3A (dashed orange and black lines) shows the LSV curve normalized by the ECSA of the electrocatalyst and its substrate (GC) in 1.0 mol L⁻¹ NaOH and with 14 mmol L⁻¹ NaNO₃. ECSA was determined by measuring the double-layer capacitance (Figure 2.3B and C). The glassy carbon shows negligible current with and without nitrate. On the other hand, the dropped cast Cu₂O NCs on the glassy carbon shows an enhancement in the cathodic current within the negative applied potential range. This increase becomes more pronounced at more negative potentials, potentially attributed to the HER and copper oxide reduction. In the presence of nitrate (Figure 2.3A (solid orange line)), a transient peak emerges between -0.3 and -0.4 V vs. RHE with five times higher current density than in the absence of nitrate. The cathodic current density decreases below -0.4 V vs. RHE, suggesting a surface site blockage for nitrogen-containing molecules caused by the adsorption of hydrogen.⁶⁸

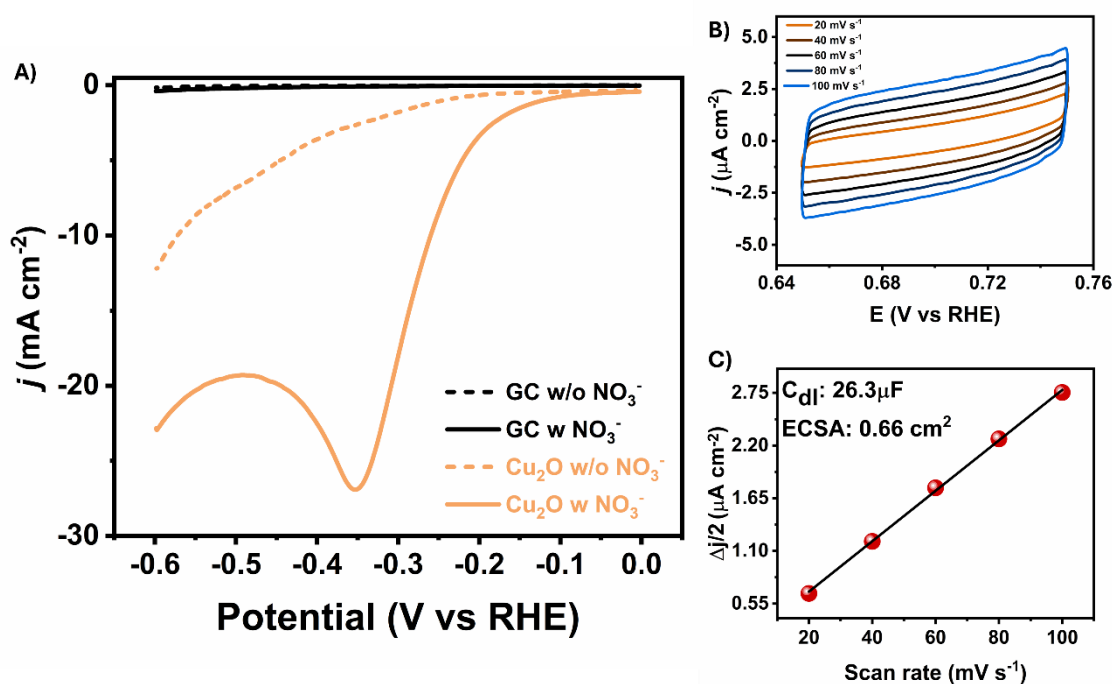


Figure 2.3. NO₃RR electrochemical performance of Cu₂O NCs. A) LSV curves of GC substrate (black) and Cu₂O drop cast on GC (orange) in 1.0 mol L⁻¹ NaOH (dotted line) and 1.0 mol L⁻¹ NaOH + 14 mmol L⁻¹ NaNO₃ (solid line). Scan rate of 50 mV s⁻¹. Electrochemically active surface area (ECSA) measurements. (B) Cyclic voltammograms of Cu₂O NCs at different scan

rates (20 to 100 mV s^{-1}) in 1.0 mol L^{-1} NaOH electrolyte. (C) linear relationship (black line) for the modulus of the average of double-layer current and the scan rate.

To verify the reduction of the Cu^{1+} species within the nitrate reduction potential range, we employed successive cyclic voltammograms, gradually increasing the cathodic limit by 100 mV, to determine the potential where the Cu^{1+} is converted to Cu^0 and an oxidation peak of the metallic copper starts to emerge by cycling the electrode back to the anodic region (Figure 2.4). We found that the Cu oxidation peak is first detected in the anodic scan after cycling the electrode from 0.3 to 0.2 V vs. RHE, which indicates that Cu_2O reduces within this potential range. In the presence of nitrate (14 mmol L^{-1} NaNO_3), the LSV of the Cu_2O NCs exhibits an onset potential of 0.1 V vs. RHE as illustrated in Figure 3B. Indicating that the Cu^{1+} species starts to reduce before the nitrate reduction.

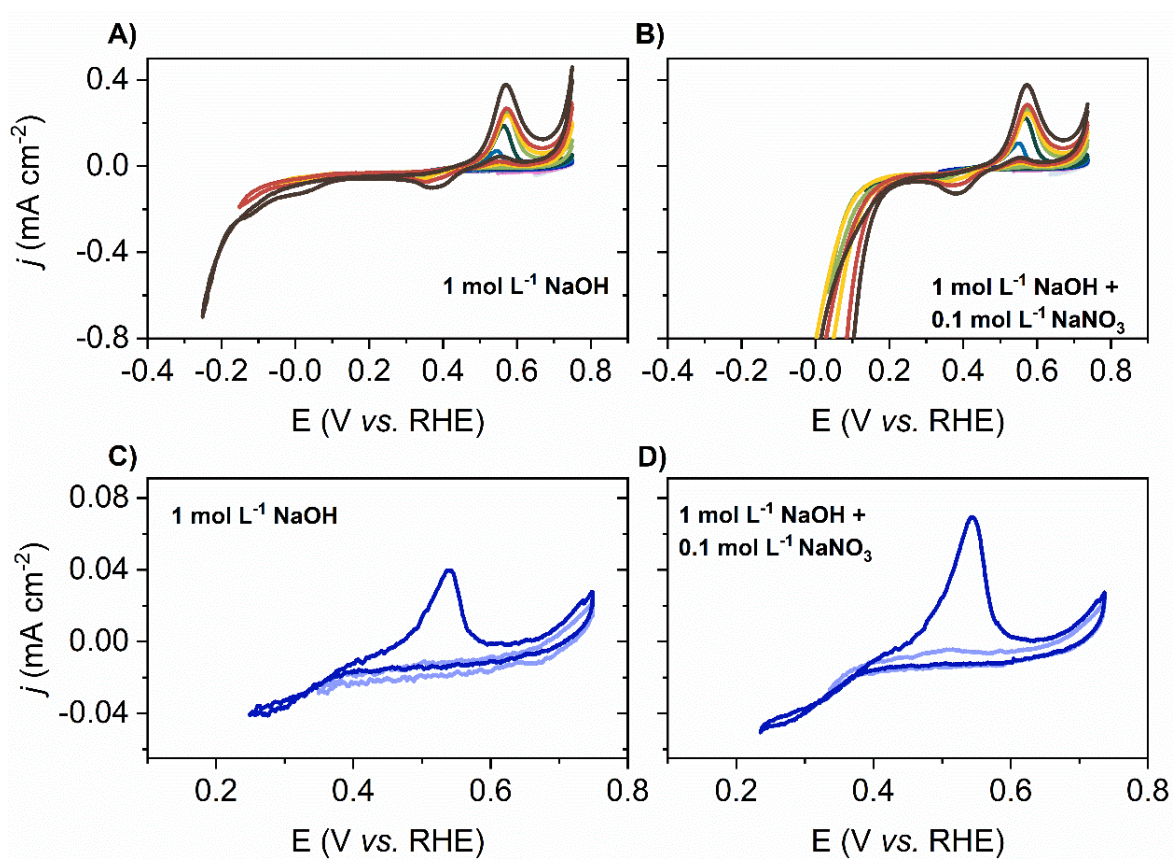


Figure 2.4. Ten successive cyclic voltammograms increasing the cathodic limit without (A) and with (B) 0.1 mol L^{-1} NaNO_3 (scan rate 20 mV s^{-1}). (C) and (D) highlight the two consecutive CVs where the Cu oxidation appears for the first time without and with NaNO_3 respectively.

The highest FE and yield rate towards ammonia for the Cu₂O NCs is observed at -0.3 V vs. RHE, due to the balance between hydrogen coverage and the NO₃RR intermediates at more positive potentials. To identify the nitrate-reduction products and evaluate the catalyst efficiency, we performed 1 h electrolysis in a solution containing 1.0 mol L^{-1} NaOH and 14 mmol L^{-1} NaNO₃ in a potential range of -0.1 to -0.6 V vs. RHE (step potential 0.1 V). Figure 2.5A displays the FE values for NH₃ and NO₂⁻ (bars in Figure 2.5A), and the NH₃ yield rate (purple line in Figure 2.5A) and the current density for each potential (Figure 2.5B). Both products were quantified by colorimetric methods⁶⁶ (Figure S2 A and B). At low overpotentials (e.g. -0.1 V vs. RHE) we observed the highest FE for NO₂⁻ followed by the smaller current density as shown in Figure 2.5B. As the potential is shifted from -0.1 to -0.3 V the FE for NO₂⁻ decreases from 62.6% to 7.5% while the FE for NH₃ increases from 24.3% to 93.6%. The decrease in FE for NO₂⁻ with increasing the cathodic potential was expected, as NO₂⁻ is an intermediate for the formation of NH₃.^{60,68} The FE and yield rate for NH₃ is the highest at -0.3 V vs. RHE (FE: $93.6 \pm 4.25\%$ and yield rate: $10.87 \pm 1.69 \mu\text{g h}^{-1} \text{ mg}_{\text{cat}}^{-1}$) accompanied by a current density three times higher than at -0.1 V. The maximum in FE and yield rate at -0.3 V is consistent with the location of the LSV peak in Figure 2.4A. We observed a decrease in FE and yield rate toward NH₃ between -0.4 V and -0.6 V vs. RHE, indicating a potential domain where the hydrogen adsorption competes for active sites with NO₃RR. The potential of the highest FE (-0.3 V vs. RHE) agrees with what was reported in the literature for shape controlled Cu₂O catalyst.³⁸

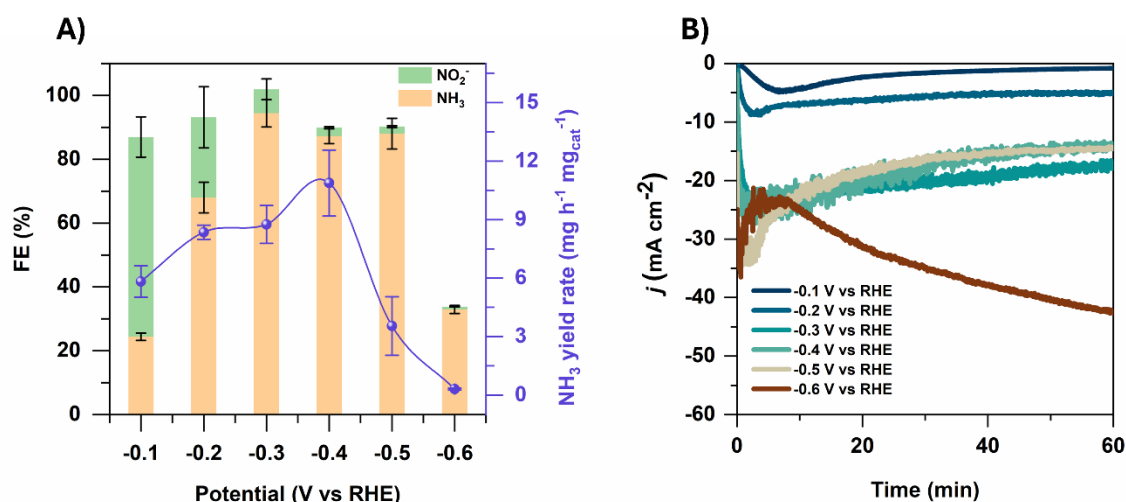


Figure 2.5. NO₃RR electrochemical performance of Cu₂O NCs. A) Potential-dependent NH₃ yield rate (purple line) and FE of NO₃RR to NO₂⁻ and NH₃ of Cu₂O NCs in green and orange bars in 1.0 mol L^{-1} NaOH + 14 mmol L^{-1} NaNO₃. B) Chronoamperometry curves 1 h longer of Cu₂O NCs at different applied potentials from -0.1 V to -0.6 V vs. RHE in 1.0 mol L^{-1} NaOH with 14 mmol L^{-1} of NO₃⁻ under magnetic stirring at 400 rpm.

Another important parameter for evaluating the performance of an electrocatalyst is its selectivity, especially for ammonia production.²⁷ In this case, we calculated the selectivity for NH_3 and NO_2^- at the same potential range, which is presented in Figure 2.6A. Nitrite selectivity decreases rapidly with increasing potential, while for NH_3 it reaches a plateau at -0.3 V vs. RHE and remains almost constant up to -0.6 V vs. RHE , which means that from -0.3 V vs. RHE , increasing the overpotential does not improve the catalyst selectivity toward ammonia. We show that nitrate is the nitrogen source for ammonia electrosynthesis through isotopic labeling, followed by product identification by ^1H NMR. By using $\text{Na}^{14}\text{NO}_3$ in the electrolyte, we found three- characteristic symmetrical ^1H signals of $^{14}\text{NH}_4^+$, while with $\text{Na}^{15}\text{NO}_3$ only the two symmetrical ^1H signals of $^{15}\text{NH}_4^+$ are observed (Figure 2.6B). These results suggest that NO_3^- is the main source of nitrogen for ammonia formation.

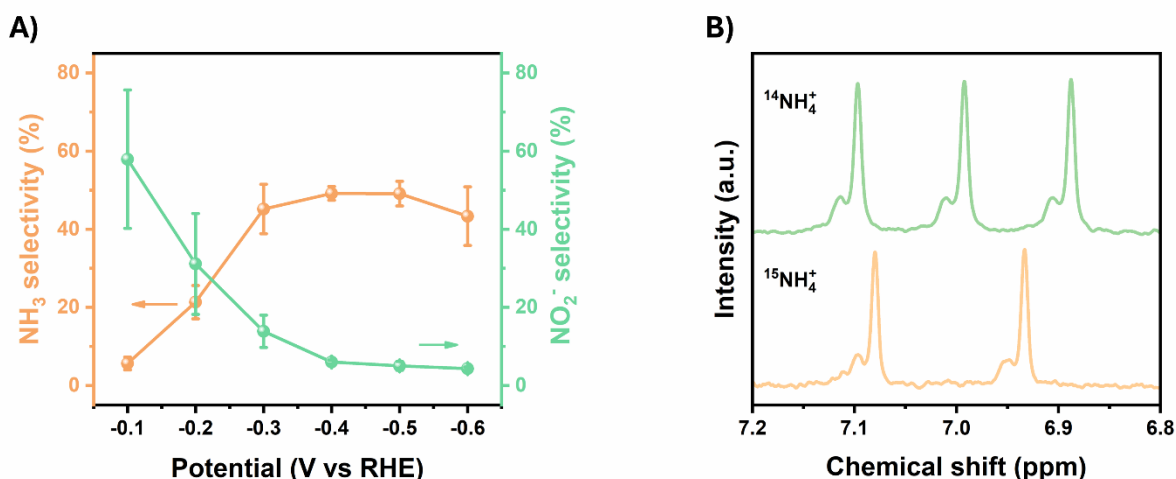


Figure 2.6. A) Selectivity of NO_2^- and NH_3 at different potentials. C) ^1H nuclear magnetic resonance (NMR) spectra of the electrolyte after NO_3RR over Cu_2O NCs at -0.3 V vs. RHE using $\text{Na}^{14}\text{NO}_3$ and $\text{Na}^{15}\text{NO}_3$ as the nitrogen source.

We evaluated the catalyst performance over 10h by doing an electrolysis at -0.2 V vs. RHE refreshing the electrolyte every 2h, the results are displayed in Figure 2.7. Surprisingly, after 4h applying the potential, we observed a gradual increase of the FE and the yield rate for ammonia from $\sim 73\%$ to $\sim 85\%$ and $3.7 \mu\text{g h}^{-1} \text{ mgcat}^{-1}$ to $6.5 \mu\text{g h}^{-1} \text{ mgcat}^{-1}$, respectively. This suggests dynamic changes in the material surface throughout the experiment until it reaches a plateau, potentially attributed to the reduction of the underneath layers of the Cu_2O NCs catalyst.

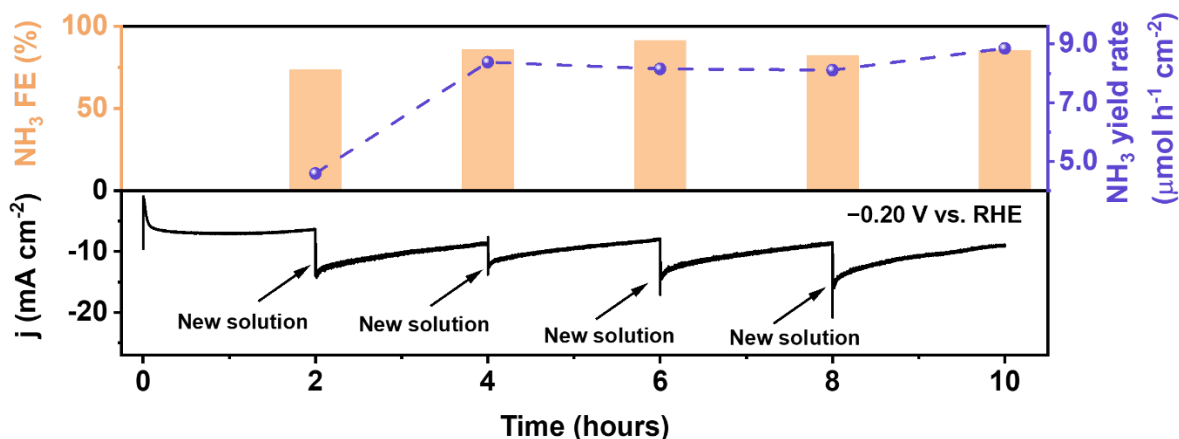


Figure 2.7. NO₃RR electrochemical performance of Cu₂O NCs at -0.2 V vs. RHE over 10 hours in 1.0 mol L^{-1} NaOH + 14 mmol L^{-1} NaNO₃. At the top image the orange bars correspond to NH₃ FE while the yield rate is represented by a black line. The current density over time is represented as a black line at the bottom image.

2.3.3 Post-Electrolysis and in situ Electrocatalyst Surface Characterization

We observed a substantial structural evolution of the Cu₂O NCs during the NO₃RR. Figures 2.8A and B display the FESEM and BF-STEM images of the catalyst after 1 h electrolysis at -0.3 V vs. RHE in NaOH 1.0 mol L^{-1} and NaNO₃ 14 mmol L^{-1} . The Cu₂O NCs' surface presents shape deformation accompanied by merged domains after the applied potential. In contrast to the smaller particles (~ 50 nm), larger particles (average size ranging from 150 to 600 nm) exhibited rougher surfaces and fewer morphological changes, keeping their cubic shape (Figure S2.3). This illustrates the susceptibility of the oxide surface to instability under cathodic potential, as the initially well-defined particles undergo a near-complete loss of their cubic morphology. Additionally, we observed some preserved nanoparticles in the TEM image (Figure 2.8B) possibly indicating that an underneath particle layer remains stable after the applied potential. The corresponding elemental mapping shows the distribution of the Cu and O (Figure 2.8C-D). The Cu map displayed a uniform distribution across the sample, as in as prepared sample in Figure 2.1D. However, the O map (Figure 2.8D) showed a lower intensity compared to the O map acquired before the electrochemistry (Figure 2.1E). Notably, the cubic domains, characterized by their preserved morphology, exhibit the highest oxygen intensity region. Supporting that the oxide underlayer, which remains unexposed to the electrolyte during the electrolysis is preserved. Based on this, it is improbable that the sustained FE over 10 hours is correlated with the well-defined pristine cubic morphology.

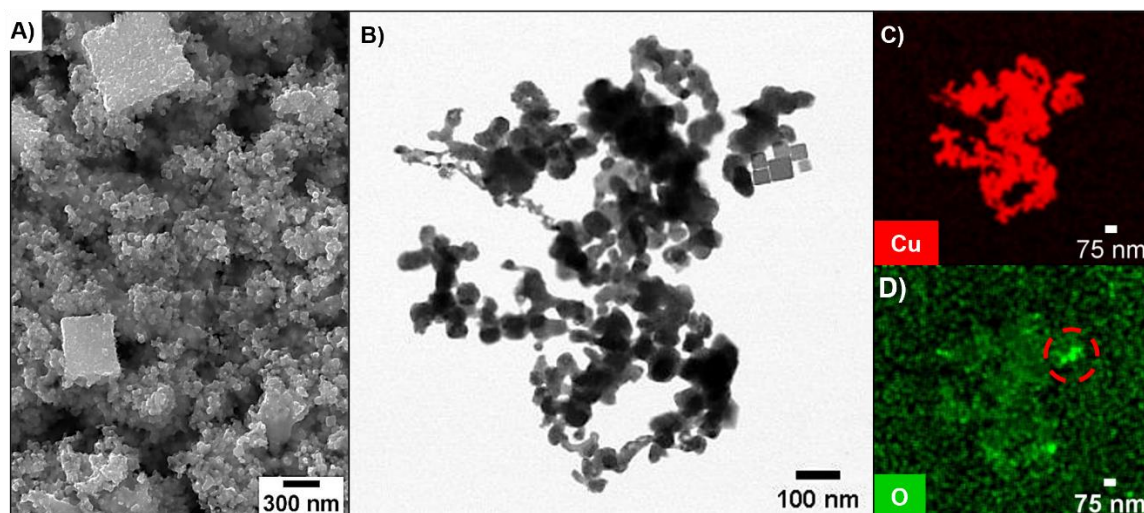


Figure 2.8. Structural and chemical characterization of the post-electrolysis Cu_2O NCs in $1.0 \text{ mol L}^{-1} \text{ NaOH} + 14 \text{ mmol L}^{-1} \text{ NaNO}_3$ at -0.3 V vs. RHE after 1 hour. A) FESEM image of the Cu_2O NCs on the glassy carbon substrate. B) BF-STEM image and corresponding EDS maps of C) Cu and D) O elements.

Employing AFM (Figure 2.9A) we upheld the proposition that the catalyst grains underwent sintering, due to an increase in the height to $2.3 \mu\text{m}$, compared to the previously measured on the fresh surface ($0.6 \mu\text{m}$) (Figure 2.2A). These results seem to be different from those observed for the electroreduction of CO_2 in Cu_2O nanocubes, which due to the experimental conditions ($0.1 \text{ mol L}^{-1} \text{ NaHCO}_3$, -0.9 V vs. RHE for 45 minutes) undergo the process of dissolution and re-deposition.⁵⁸

To track the chemical composition changes of the Cu_2O NCs we employed Raman spectroscopy. The surface mapping of the signal at 224 cm^{-1} of the Cu_2O in a $30 \times 30 \mu\text{m}$ area (Figure 2.9B) revealed an intensity 2.3 times lower than that observed in the fresh electrode (Figure 2.2B). This diminished signal across the analyzed area is attributed to catalyst non-homogeneity distribution. However, we observed distinct spots, as illustrated in Figure 2.9C, where a mixed oxide phase is evident, exhibiting signals at 150 cm^{-1} and 225 cm^{-1} associated with Cu_2O , along with a signal at 285 cm^{-1} ascribed to CuO . Additionally, there is a signal at 1086 cm^{-1} related to adsorbed nitrate, indicative of remaining species on the catalyst surface.^{66,69} To evaluate the catalyst's phases, facets distribution, and copper oxidation state, we additionally conducted XPS and GIXRD measurements in the post-electrolysis electrode (Figures 2.9D and 2.9E, respectively). The XPS measurement indicates in the $\text{Cu } 2p_{3/2}$ spectra the presence of two peaks centered at 932.5 and 952.4, both attributed to the Cu^+/Cu^0 oxidation state on the catalyst near-surface.⁷⁰ Moreover, a residual presence of Cu^{2+} is observed on the catalyst surface.³⁸ The

contribution of the Cu^0/Cu^+ peak corresponded to 87 %, while Cu^{2+} accounted for 13 %. The presence of CuO , can be attributed to oxidation upon exposure to atmospheric air or even to a surface oxidation by the alkaline electrolyte.⁶⁵ Furthermore, the GIXRD pattern evidenced the presence of polycrystalline metallic copper with crystallographic planes (111) at $2\theta = 43.26^\circ$, (200) at $2\theta = 50.35^\circ$, and (220) at $2\theta = 74.21^\circ$ confirming the reduction of Cu_2O post-electrolysis. However, we also identified a residual presence of Cu_2O with planes (111) and (220) at $2\theta = 36.32^\circ$ and 61.72° , respectively suggesting that the catalyst may have a combination of Cu^+/Cu^0 phases. Nevertheless, ex-situ XRD analysis may not provide the most accurate results for characterizing the post-electrolysis surface, primarily due to the inherent instability of Cu when exposed to air.

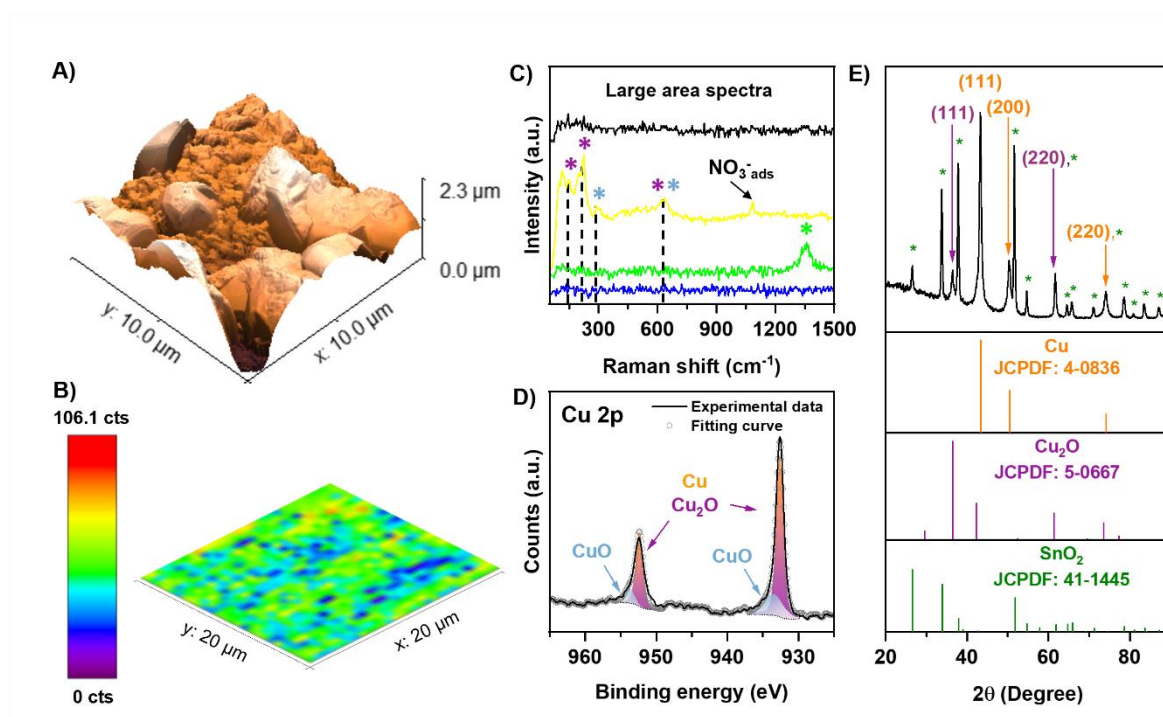


Figure 2.9. A) AFM image capturing a $30\ \mu\text{m} \times 30\ \mu\text{m}$ section of the Cu_2O NCs deposited on GC. B) Raman mapping of the $224\ \text{cm}^{-1}$ signal of Cu_2O NCs deposited on GC and C) the spectra of a specific area and the entire region analyzed. D) high-resolution $\text{Cu}\ 2\text{p}$ XPS spectra. E) GIXRD pattern of Cu_2O NCs deposited on FTO substrate. Cu , Cu_2O and SnO_2 standard are shown below.

To avoid the air exposure, we employed in situ Raman measurements (Figure 2.10), the spectra revealed two pronounced peaks at 295 and $340\ \text{cm}^{-1}$ attributed to CuO species,⁶⁶ the presence of these oxides persists throughout the entire evaluated potential range, both in the absence of nitrate and during NO_3RR (Figures 2.10A and B). Interestingly, we detected three

additional peaks centered at 150, 520, and 620 cm^{-1} related to Cu_2O species, evidencing the presence of a metallic and oxidized copper phase on the catalyst surface.⁶⁶ Therefore, we conducted in situ Cu K-edge X-ray absorption near edge spectroscopy (XANES) to investigate the Cu^x active site for NO_3RR . The in situ XANES spectra were collected at OCP, -0.2 V, -0.4 V, and -0.6 V vs. RHE (Figure S2.4A). To estimate the E_0 at each applied potential, the maxima of the first derivative curves were determined (Figure S2.4B). We observed the Cu K-edge peak at 8983 eV at open circuit voltage (OCP), attributed to Cu_2O ,⁷¹ and as the cathodic potential was applied this peak shifted towards the Cu^0 value at ~ 8980 eV⁴¹ (Figure S2.4). These results are consistent with the reduction of Cu_2O to Cu^0 during NO_3RR . We also hypothesized that the presence of remaining Cu_2O species is related to possible loss of electric contact due to a weak binding of some NCs with the substrate or by the presence of an underneath oxide particle layer that is not exposed to the electrolyte, even after 1h applying a negative potential. Anastasiadou and co-workers showed by quasi in situ XPS and XRD that after 20 minutes of NO_3RR almost all Cu_2O (111) and (100) sites were reduced to Cu, being ascribed as the active sites.³⁸ Our observations align with their research findings, indicating that the remaining oxide phase is minority on electrode surface. By analyzing the Raman results we could observe also that the presence of oxide phase could be related to some isolated spots on the surface that we assume not being the majority active sites of the catalyst.

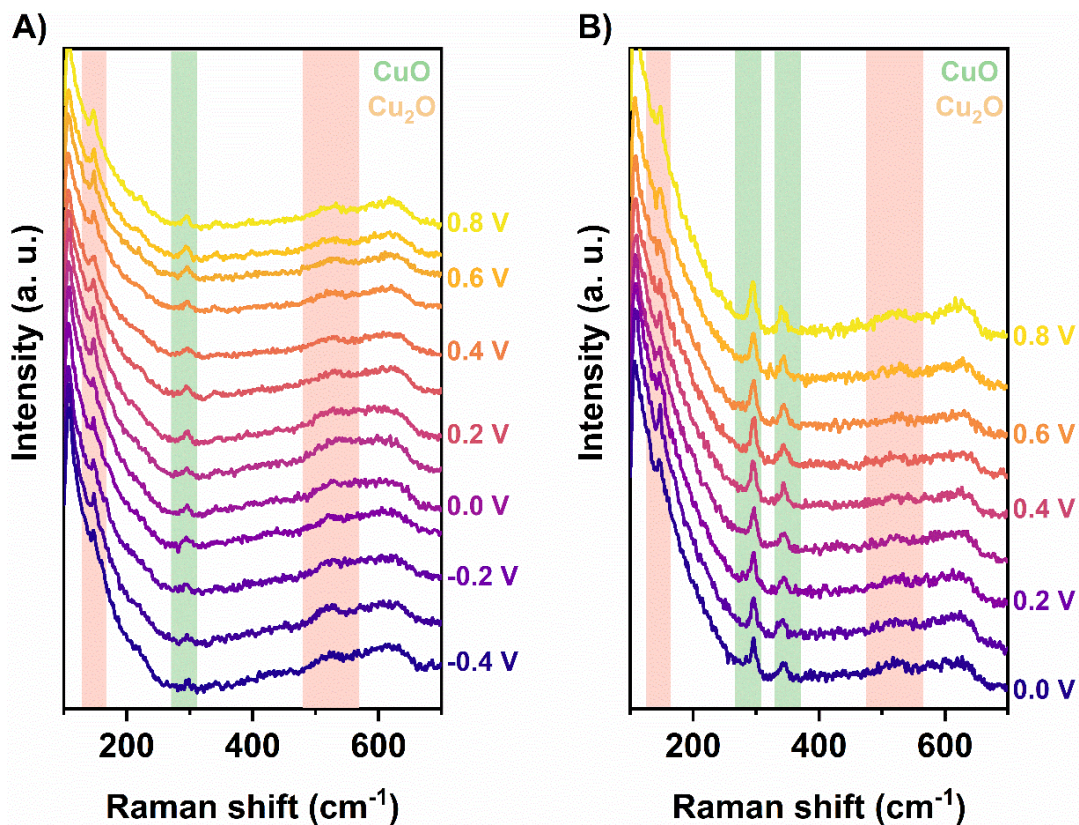


Figure 2.10. In situ Raman spectra A) without (potential range: 0.8 to -0.4 V *vs.* RHE) and B) with 0.1 mol L⁻¹ of NaNO₃ (potential range: 0.8 to 0 V *vs.* RHE) in 1.0 mol L⁻¹ NaOH electrolyte. Pink marks highlight the peaks related to Cu₂O (145, 520, 630 cm⁻¹) and green ones highlight peaks

Based on the foregoing results, we propose that the performance of the (100) oxide-derived Cu surface is associated with the Cu⁰ surface. The observed correlation is influenced by the variations in probing depth among the utilized techniques. Thus, under an applied potential the process initiates with a rapid surface reduction, inducing shape loss, and gradually extends to underneath layers over time. This phenomenon may account for the gradual increase in FE observed during the 10-hour electrolysis. It suggests that, following the initial 6 hours, the electrocatalyst achieves a Cu⁰ composition that exhibits higher activity than the mixture of oxide and metallic phases. Moller *et al.*⁷² have observed the same surface behavior during CO₂ electroreduction to C₂₊ products on Cu₂O NCs. The changes of the catalyst's structure and composition towards a Cu⁰-rich surface was identified as a pivotal factor contributing to sustained catalytic enhancement, demonstrated over a continuous period of 40 hours. They conclude that the emergence of defects in the Cu lattice during the reduction of the oxide contributes to the observed efficiency. Similarly, our findings show that the reconstructed Cu₂O NCs which may generate Cu uncoordinated atoms could act as the NO₃RR active sites.

Moreover, for NO₃RR, the Cu⁰ surface derived from Cu₂O has also been described as the active phase. Furthermore, the morphological evolution of the oxide might be responsible to create Cu⁰ sites that are more active and selective to ammonia than the polished Cu⁰ surface.^{38,54,57} Nonetheless, the influence of the pristine orientation of the Cu₂O catalyst on the reaction pathways is still unclear, and necessitates more control experiment to prove this correlation.

2.3.4 The Role of the Cu₂O NCs in the Reaction Mechanism

The role of these Cu₂O-based materials in the reaction mechanism of NO₃RR is ascribed to different factors. Wang and co-workers³² attribute the Cu-Cu₂O interface as the active site of their catalyst as it promotes the formation of the intermediate *NOH, which is further hydrogenated to produce hydroxylamine (NH₂OH). Fu et al. showed that the Cu₂O/Cu interface changes the mobility of key intermediate and electron transfer enhancing the NO₃RR activity.⁷³ In addition, Shi and co-workers demonstrated that the presence of oxygen vacancies and the electron transfer from Cu₂O to Cu in Cu/Cu₂O nanorods are important for the superior catalyst activity. Firstly, Cu vacancies sites promote the reduction of NO₃⁻ to NO₂⁻ that are further reduced to NH₃ due to the presence of adsorbed hydrogen atoms on the Cu₂O interface.⁷⁴ Contrarily, Daiyan *et al.*⁷⁵ found that oxygen vacancies formed in the Cu₂O lattice favor the formation of *HNO₂ intermediate, which is further reduced to *NO, *HNO, and *H₂NO, being the last one responsible for promoting the formation of NH₃ through a proton-electron pair transfer. Costa et al. also evaluated by applying in situ and ex situ techniques that the presence of oxygen vacancies on the Cu oxide derivate surface promotes the NO₃RR, through the NH₂OH intermediate formation. In this session, we aim to determine the role of Cu₂O-based electrocatalysts in NO₃RR with in situ FTIR and online DEMS.

We carried out in situ FTIR chronoamperometry experiments to identify and monitor the N-content species adsorbed on the catalyst surface, especially NO_x and NH₂OH, during the NO₃RR. We show in Figure 2.11A an overlapped absorption band between 1610-1690 cm⁻¹ that rises at 0.2 V vs. RHE, ascribed to the O-H bending mode of water molecules and/or the N-O stretching of adsorbed NO_x intermediates.^{21,27,76-78} Meanwhile, the absorption band around 1190 and 1050 cm⁻¹ is observed in the potential range of -0.6 V to -0.9 V vs. RHE. This is attributed to the -NH₂ stretch related to the hydroxylamine formation.^{60,79} The absence of the characteristic nitrite peak at 1231 cm⁻¹ indicates the rapid conversion of NO₂⁻ to NO and, consequently, from NO to NH₃, since the nitrite conversion is the rate-determining step in the reaction.^{11,21} For Cu

single crystals (111) and (100), this was only observed in acidic media.⁶⁰ The absence of the hydroxylamine-related band up to -0.6 V *vs.* RHE suggests that hydroxylamine is formed at a very low concentration up to this potential, and from this onwards, it was detected at all potentials. We also probe the formation of key volatile species by tracking the ionic currents related to different mass/charge (m/z) ratios with DEMS (Figure 2.11B). As expected, we detected an increase in the ionic current of $m/z = 2$ from -0.3 to -0.8 V *vs.* RHE assigned to H₂ formation. This confirms that part of the cathodic current observed in the LSV curve in the absence of nitrate (Figure 2.3A dashed orange line) is associated with HER. The same increase was observed for $m/z = 17$, which could be related to an ammonia fragment NH₃,⁸⁰ however, since the experiment was performed in an aqueous electrolyte this fragment can also be ascribed to a water fragment, which was also monitored through the $m/z = 18$ (Figure S2.5). For that reason, since ammonia was already quantified through other methods, we assume that this fluctuation is an overlap of both species which the main contribution in the ionic current for the fragment $m/z = 17$ is related to the presence of water. The $m/z = 28$ corresponds to N₂, and the increase in the ionic current is first detected from -0.6 V *vs.* RHE, explaining the decrease of the NH₃ FE (Figure 2.5A). Additionally, the ionic current of $m/z = 29$ was first detected at -0.4 V *vs.* RHE and can be related to the formation of both N₂H₂ and N₂H₄ (N₂H⁺ fragment with $m/z = 29$). These species are further converted into N₂, which is better discussed below. The ionic current of $m/z = 30$ also increases from -0.4 V *vs.* RHE, being related to both N₂H_x species and NO, also detected by in situ FTIR. We also probe $m/z = 33$ related to NH₂OH, which is first detected from -0.6 V *vs.* RHE, in accordance with in situ FTIR as well. This result suggests that between -0.3 to -0.5 V *vs.* RHE, NH₂OH is rapidly converted to NH₃, making it challenging to detect. Thus, in these conditions, NH₂OH is considered the key intermediate in alkaline electrolytes, as well as NO_x species. These observations align with Daiyan and co-workers who focus on the role of Cu₂O-based electrocatalysts in NO₃RR on sequential hydrogenations of *NO intermediate.⁷⁵

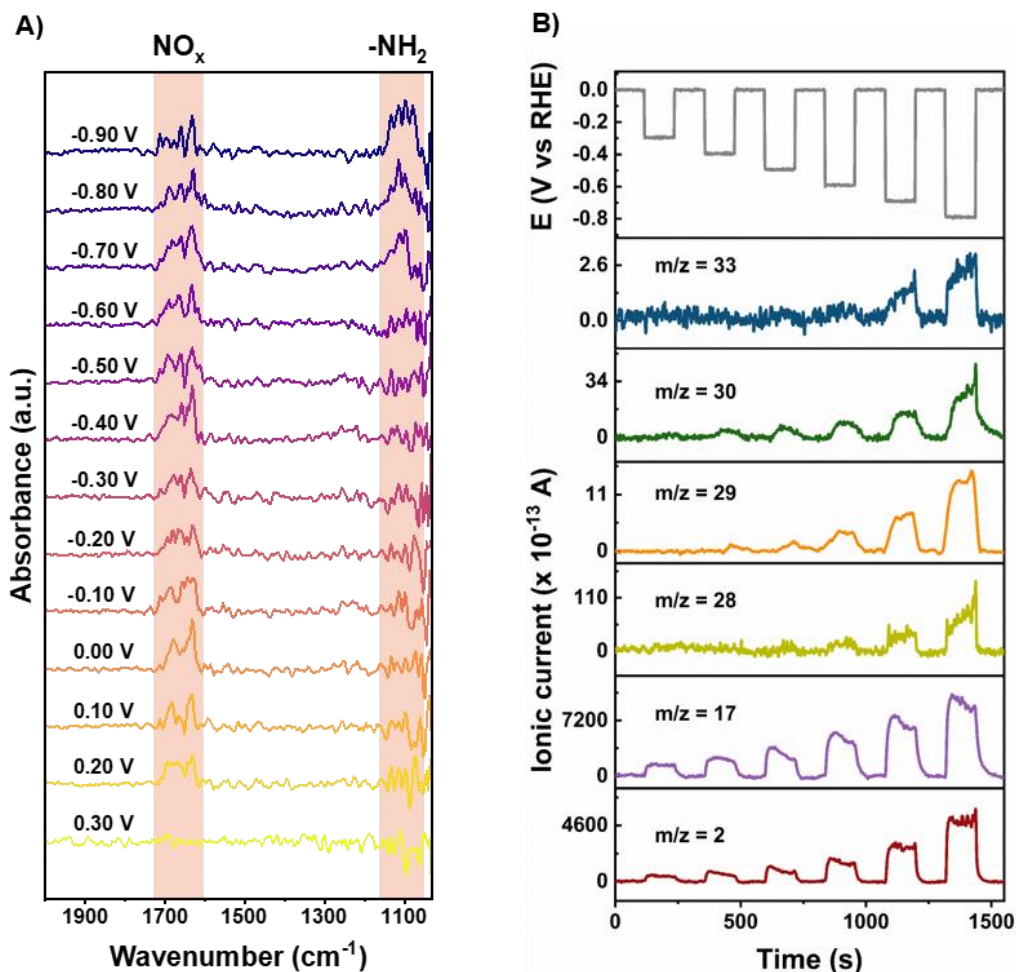


Figure 2.11. A) in situ FTIR spectra of Cu_2O NCs in 1 mol L^{-1} NaOH electrolyte containing 14 mmol L^{-1} NaNO_3 . The peak centered at $1,190 \text{ cm}^{-1}$ related to $-\text{NH}_2$ from NH_2OH and the peak centered at 1690 cm^{-1} is related to NO_x adsorbed species both are highlighted in orange) online DEMS of Cu_2O NCs recorded in 1 mol L^{-1} NaOH + 14 mmol L^{-1} NaNO_3 as electrolyte. The applied potential vs. time is represented at the top, followed by the ionic current of possible ionic fragments presents in the reaction. The $m/z = 2$ corresponds to the dihydrogen fragment, while $m/z = 17$ represents ionic fragments from NH_3 and H_2O . Additionally, $m/z = 28$ (N_2), 29 (N_2H_2 or/and N_2H_4), 30 (N_2H_x or/and NO), and 33 (NH_2OH) correspond to ionic fragments of possible intermediates of NO_3RR .

From the above results, two possible nitrate electroreduction pathways were observed, an ammonia route (from hydroxylamine as an intermediate) and a hydrazine route. The rate-determining step in the reactions is the conversion of NO_3^- to NO_2^- , followed by the reduction of NO_2^- to NO .^{11,68,81} From this, two possible paths are proposed: NO is reduced to NH_2OH and then to NH_3 , as proposed by Pérez-Gallent and co-workers⁶⁰; NO is deoxygenated, hydrogenated, and coupled with two NH species, leading to the formation of N_2H_4 . This route was proposed by Hwang and collaborators with N_2H_4 as an intermediate to produce ammonia.⁸²

However, in hydrazine reduction experiments, ammonia was not detected even at more negative potentials Figure 2.12.

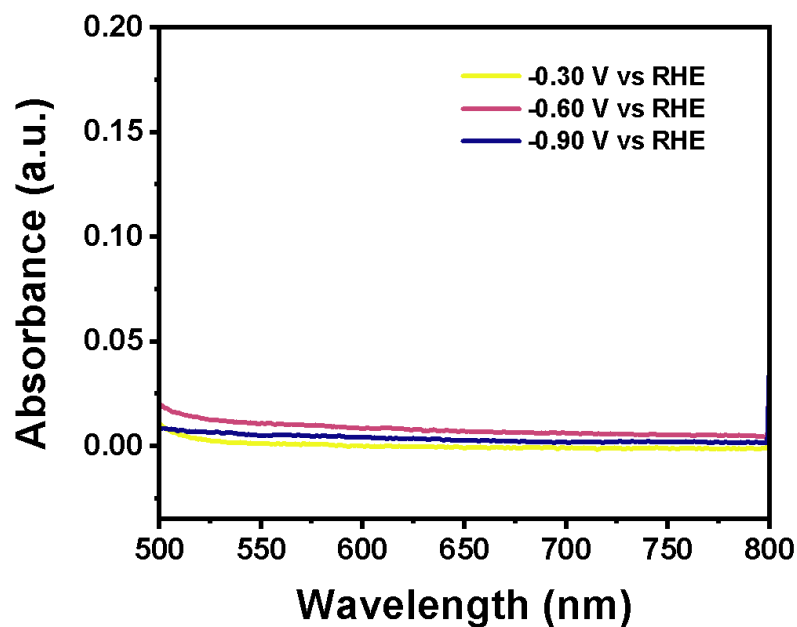


Figure 2.12. UV-vis spectrum of ammonia quantification by chronoamperometry at -0.30 V, -0.60 V and -0.90 V vs. RHE in 1.0 mol L^{-1} NaOH and 0.20 mol L^{-1} N_2H_4 .

For this reason, we attribute the role of Cu_2O NCs in NO_3RR to ammonia to the facilitated hydrogenation of NO species. A simplified mechanistic scheme is shown in Figure 2.13.

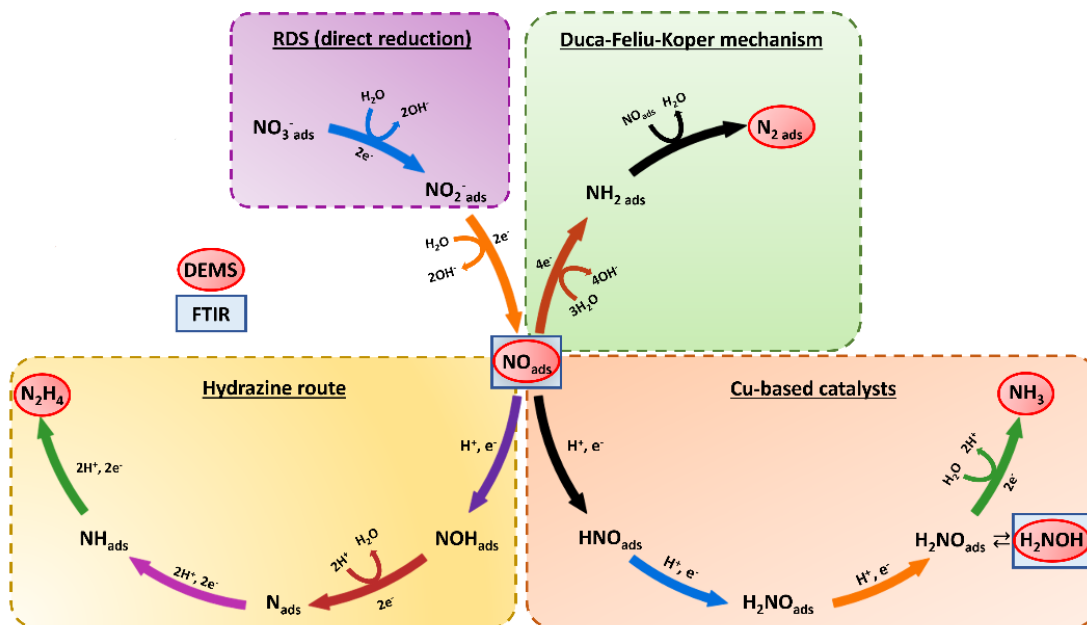


Figure 2.13. Possible mechanism for NO_3RR by Cu_2O NCs electrocatalyst.

2.4. Conclusions

This study identifies and correlates chemical and structural factors that contribute to the NO_3RR . Using ex situ and in situ characterizations we demonstrate that during NO_3RR a well-defined surface of Cu_2O NCs is rapidly converted into an oxide-derived Cu^0 on the near surface followed by a gradual reduction of the underneath layers. This surface reconstruction leads to the generation of defects in the Cu lattice, acting as the main active sites for the reaction. Despite the structural and compositional changes, the catalyst presented at lower overpotential (-0.2 V vs. RHE) an increase in FE from 73% to 92 % after the initial 6 hours, maintaining this performance for 10 hours, highlighting that the active site is not the pristine oxide surface. Furthermore, we established an experimental mechanism investigation to attribute the role of Cu_2O NCs derivate surface in NO_3RR to ammonia, in which we found that their main contribution to NH_3 formation lies in facilitating NO hydrogenation to form NH_2OH . These findings underscore the paramount significance of comprehending the structural and compositional evolution of the catalyst during NO_3RR . This insight provides an indispensable basis for discerning trends in the activity/stability of this reaction on Cu-based catalysts, establishing a basis for the systematic optimization of electrocatalysts with enhanced efficiency

Chapter 3: Rotating Ring disk (RRDE) approach for detection of reactive oxygen species (ROS)

3.1. Introduction

The electrochemical approach, such as Rotating Ring Disk Electrode (RRDE) technique stands as a precise and sensitive method for directly detecting stable intermediates during electrochemical reactions.^{83,84} Through a controlled mass transport, species generated on the disk can be detected on a polarized ring. For instance, the selectivity of materials during the oxygen reduction reaction (ORR) has been extensively investigated.⁸⁵ Electrochemical processes, such as the elucidation of catalyst selectivity during CO₂ electroreduction and the study of the performance of materials for hydrogen evolution reaction also exemplify the effectiveness of the technique.^{86,87} Furthermore, the RRDE experiments have been employed for qualitative studies into the two-electron water oxidation reaction (2e⁻ WOR) for H₂O₂ production.^{88,89} However, during water oxidation other species aside from O₂ and H₂O₂ can be generated.^{90,91} Thus, characterizing these species can provide deeper insights into electrocatalyst selectivity.

Here, we used the rotating ring disk electrode (RRDE) technique to identify and quantify the generation of reactive oxygen species (ROS) during the water oxidation. Through an examination of the current contribution attributed to O₂, O₃ and H₂O₂ across defined potential ranges we isolated the electrochemical response of each species. To validate our proposed methodology, we conducted a characterization of Pt (poly) electrode previously investigated for anodic production of O₃ and H₂O₂.^{92,93} Our analytical approach reveals that under an overpotential, the measured faradic current measured is not solely attributable to OER but also to the production of H₂O₂ and O₃, and the surface identity plays an important role on the species distribution rates.

3.2. Methods

3.2.1 Electrochemical measurements

Electrochemical measurements were performed using a Metrohm Autolab PGSTAT302N electrochemical workstation configured with three electrodes. The counter and reference electrodes employed were platinum wire and Hg/HgSO₄, respectively. The working electrode was a 6mm Pt(poly) disk. We use 0.1 mol L⁻¹ of H₂SO₄, NaHCO₃, Na₂CO₃ and NaOH as support electrolyte. For each electrolyte, the current was measured over a potential range of 0.1 to 1.2 V vs. RHE under three different conditions. The first condition was the electrolyte saturated with O₂. The second condition, the electrolyte saturated with a mixture of O₂ and O₃,

the ozone was produced by an MP-8000 Water Ozone Generator supplied with oxygen. In the third condition the electrolyte was saturated with Ar, to which 1 mmol L⁻¹ of H₂O₂ was added. A fluoropolymer-based cell was used to avoid contamination from glass components in the alkaline electrolyte. To prevent any potential contamination from prior experiments, the cell underwent a rinsing process with deionized (DI) water, followed by boiling DI water. OER and ROS measurements were carried out by cycling the metal electrode in different potential ranges. All the reported currents were normalized by the geometric area of the 6 mm disk (0.283 cm²). The RRDE setup was composed of a platinum ring. Before every experiment the ring by using 0.05 μm Al₂O₃ slurry on a microfiber polishing pad and cleaned by sonicating for 5 min in isopropanol (1x) followed by sonication in water (2x).

3.2.2 RRDE Collection efficiency (N) determination

Based on the geometrical area of the RRDE used the theoretical collection efficiency is 24%. To compare with the theoretical value, we calibrated the collection efficiency for liquid and gaseous species. For liquid, we used the 1e⁻ reversible reaction [Fe (III)(CN)₆]³⁻ + e⁻ ↔ [Fe (II)(CN)₆]⁴⁻. For gaseous calibration, we choose the hydrogen evolution reaction (HER).

3.2.3 Ozone quantification

The ozone concentration was determined by the indigo method.⁹⁴ Indigo is a blue dye that presents absorbance at 600 nm and reacts stoichiometric with ozone. To prepare the indigo stock solution, potassium indigotrisulfonate salt was dissolved in 20 mmol L⁻¹ phosphoric acid to a concentration of 1 mmol L⁻¹. To construct the calibration curve, a series of standard solutions with known concentrations of the dye (10, 20, 30, 50, 70, 100, and 130 μmol L⁻¹) were prepared by diluting the stock solution. The ozone concentration in the sample was determined using the calibration curve. The decrease in absorbance at 600 nm was directly proportional to the ozone concentration.

3.3. Results and Discussion

3.3.1 RRDE collection efficiency (N)

To determine the collection efficiency (N) of the RRDE measurements for O₂, O₃ and H₂O₂ we used simple reaction. For gaseous species we choose hydrogen evolution reaction (HER) as reference since HER in Pt only produces H₂ without any other side reactions (Figure 3.1A). Thus, a Pt disk was scanned into HER region while potential of ring (Pt) was held at 0.2 V vs RHE. As shown in Figure 3.1B the current ratio between the ring and disk reaches ~10%, 2.4 times lower than the geometrical N (24%). This decrease in collection efficiency could be attributed to the formation of nanobubbles, which saturate the ring, blocking the electroactive surface and causing a collection failure.⁹⁵ Despite this difference, this ratio was consistent in all experiments where O₂ reduction was monitored. Since hydrogen and oxygen reduction on Pt is a clear process, we assume for a gas evolution reaction from the disk that just only 10% of the products are measured on the ring.⁴⁵ To calibrate the H₂O₂ (liquid product) we used [Fe (CN)₆]^{3-/4-} redox couple (Figure 3.1C). The polycrystalline Pt disk was cycled into a cathodic potential to reduce [Fe (CN)₆]⁴⁻ to [Fe (CN)₆]³⁻ while the Pt ring potential was held at 1.2 V vs RHE, high enough to oxidize the Fe [(CN)₆]³⁻ species. In this condition, the ring disk current ratio was ~24% in agreement with the theoretical geometrical N (Figure 3.1D). Thus, all the ring disk current ratios for H₂O₂ were normalized by 24%. As shown in Figure 3.1 B and D, the collection efficiency is not significantly impacted by the rotation rate for both gaseous and liquid species.

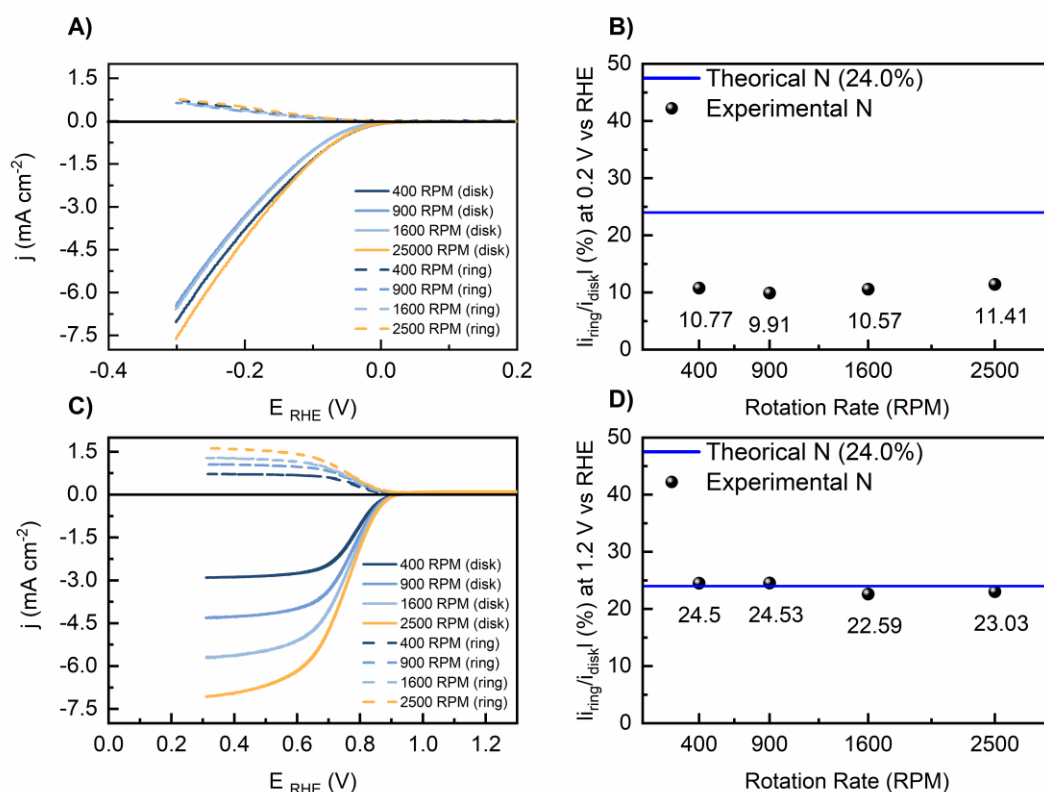


Figure 3.1. RRDE method to determine the collection efficiency (N) for gas and liquid products in 0.1 mol L⁻¹ NaOH, scan rate 50 mv s⁻¹. A) calibration for gas using HER with polycrystalline Pt and, B) the collection efficiency for different rotation rates. C) Calibration for liquid products using Fe(CN)₆^{3-/4-} redox couple and D) the collection efficiency for different rates.

3.3.2 O₂, O₃, and H₂O₂ identification

To verify the potential to be applied on the platinum ring to deconvolute the current contribution for each species we performed cyclic voltammetry between 0.1 and 1.2V vs RHE in the presence of O₂, O₃, and H₂O₂. Figure 3.2A illustrates the cyclic voltammograms (CVs) of the Pt disk electrode at different rotation rates, recorded in O₂-saturated (green lines), O₂/O₃-saturated 0.1 mol L⁻¹ H₂SO₄ and Ar-saturated (orange lines) 0.1 mol L⁻¹ H₂SO₄ + 1 mmol L⁻¹ H₂O₂ at a scan rate of 50 mV s⁻¹. We corrected the background current by the electrode CV under inert atmosphere (Ar). At more negatives potentials on the Pt metal surface (0.5 to 0.1V vs RHE) all three species present a cathodic diffusion-limiting current. In contrast, when the electrode is swept to the positive direction H₂O₂ oxidation takes place and presents a diffusion-limited oxidation current around 1.0 to 1.2V vs RHE. The oxidation and reduction processes presented the same rates, once the anodic and cathodic current have the same magnitude. At

0.94V vs RHE the current crosses zero indicating that the rates for both processes are equal with opposite signs. For O₃, between 0.9 and 1.2V vs RHE, there is a cathodic diffusion limiting current while the O₂ reduction current is zero. However, the O₃ reduction rates at more positive potentials are different from the rates between 0.5 and 0.1V vs RHE, which we correlated to the partial conversion of O₂ to O₃ in the ozone generator as confirmed by the O₃ quantification (Figure S3.1) and by calculation the number of electrons transferred in these two regions through the Koutecky- Levich plot (Figure S3.2).

Figure 3.2B illustrates the three potential selected to discern the generation of O₂, O₃, and H₂O₂. The black dots represent the respective current contributions of each species at 0.4, 0.94, and 1.2V vs RHE. Notably, at 0.4 and 1.2 V vs RHE, an overlay from all three or two species are present.

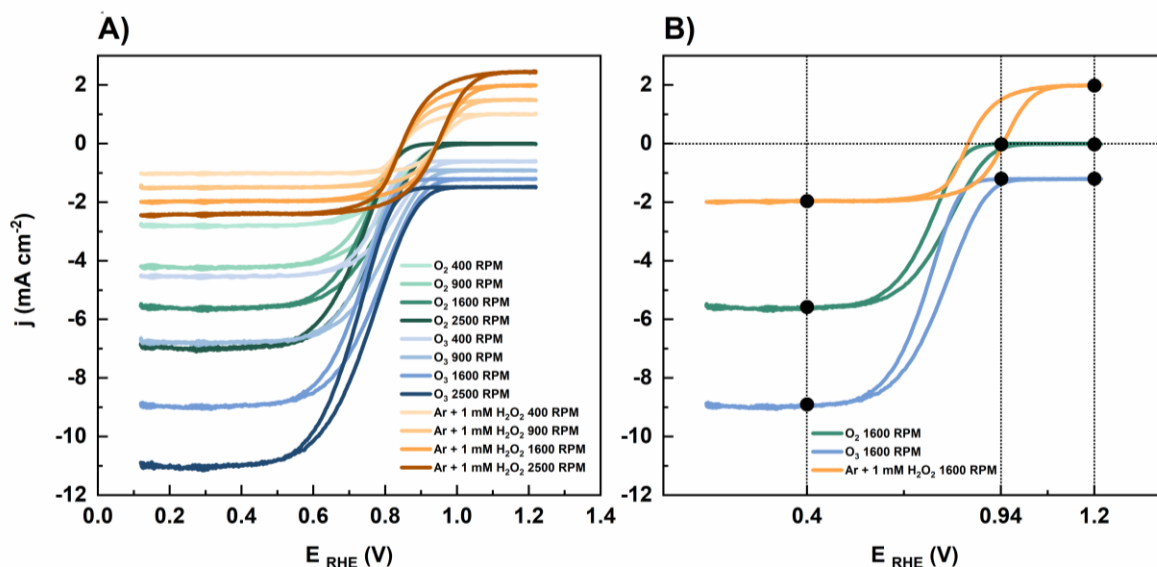


Figure 3.2. A) Cyclic voltammograms on polycrystalline Pt in O₂-saturated 0.1 mol L⁻¹ H₂SO₄ (green lines), O₃-saturated 0.1 mol L⁻¹ (blue lines) and Ar-saturated 0.1 mol L⁻¹ H₂SO₄ + 1 mmol L⁻¹ H₂O₂ (orange lines), at different rotation rates. B) highlighted current density regions at 0.4V, 0.94V and 1.2V vs RHE at 1600RPM. Scan rate: 50 mV s⁻¹.

To isolate the partial current for each species, we employed the following equations, considering the electrochemical response of each species at the three selected potentials measured on the ring. These responses were corrected for the determined collection efficiencies of the ring for gaseous (N_g) and liquid (N_l) species (Figure 3.1):

$$j_{O_3} = |j_{0.94V}| \cdot N_g \quad (3.1)$$

$$j_{H_2O_2} = (j_{1.2V} + \frac{|j_{0.94V}|}{2.4}) \cdot N_g \quad (3.2)$$

$$j_{O_2} = (j_{0.4V} \cdot N_g) + j_{H_2O_2} + (C \cdot j_{O_3}) \quad (3.3)$$

By applying 0.94V vs RHE the current density for O₂ and H₂O₂ are zero and the only contribution will be a cathodic diffusion limiting current related to the O₃ + 2H⁺ + 2e⁻ → 2H₂O + ½ O₂ reaction. Thus, the partial current density for O₃ can be determined as the absolute value of the current at 0.94V (equation 3.1). At 1.2V vs RHE both H₂O₂ and O₃ exhibit electrochemical response with opposite signs. Thus, the partial current density for H₂O₂ is calculated by the sum of the current measured at 1.2V vs RHE and the module of the current at 0.94V vs RHE divided by 2.4, which is a correction of the absolute current due the difference between the gaseous and liquid collection efficiency (equation 3.2). Is important to note that there is a hysteresis where the current crosses zero in the presence of H₂O₂, and the potential depends on the anodic or cathodic sweep. For RRDE purposes, where the Pt ring is maintained in a steady state, the electrode surface should be conditioned initially by starting with a metallic surface, as depicted in the anodic scan in Figure 3.2b. The evaluation of the O₂ partial current density is determined by subtracting the current partial current density of H₂O₂ ($j_{H_2O_2}$) and the partial current density at 0.94 V vs RHE adjusted by a correction factor (C), from the current density at 0.4 V vs. RHE (Equation 3.3). The C factor is related to the difference in current density for ozone reduction, where at 0.4V vs RHE, it is almost three times greater than the current density measured at 0.94V vs RHE (Figure 3.3). At 0.4V the ozone reduction involves 6e⁻ (O₃ + 6H⁺ + 6e⁻ → 3H₂O) while at 0.94V ozone is reduced via 2e⁻ (O₃ + 2H⁺ + 2e⁻ → 2H₂O + ½ O₂).

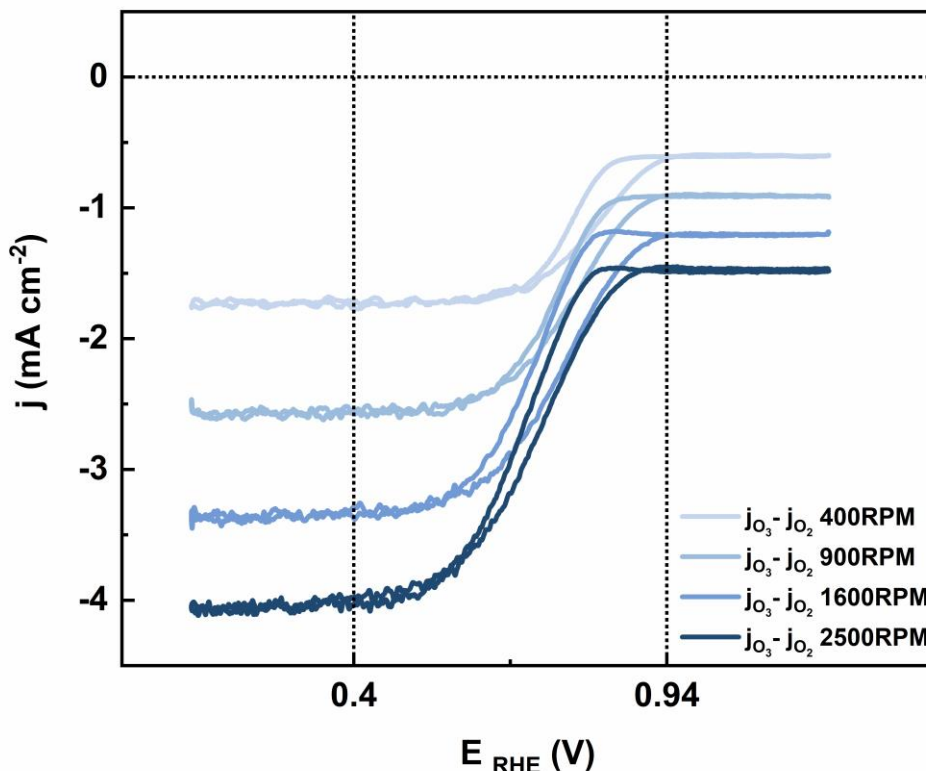


Figure 3.3. Cyclic voltammograms on polycrystalline Pt in O_3 -saturated 0.1 mol L⁻¹, at different rotation rates. at 1600RPM. Scan rate: 50 mV s⁻¹. The plotted currents are from the subtraction from the current densities measured under O_2 saturation.

To validate the method and investigate catalyst selectivity for O_2 , O_3 and H_2O_2 production via water splitting, we used as working electrode Pt(poly), a known catalyst capable of generating these species,⁹² in Ar-saturated 0.1 mol L⁻¹ H_2SO_4 electrolyte. Figure 3.4 (top, black) shows the faradaic current measured between 1.4V and 2.1V vs RHE along with the respective selectivity for O_3 (top middle plot), H_2O_2 (bottom middle plot), and O_2 (bottom plot). As expected, nearly 100% of the Faradaic current is related to O_2 production. However, by probing different potential on the ring and deconvoluting the current contributions of the oxygenated species, we quantified that approximately 1.4% of the faradaic current measured during the water oxidation on the disk is related to O_3 , production while around 0.55% is attributed to H_2O_2 . The presented results demonstrate that even less active materials for ROS can generate these species. For practical applications such as fuel cells, where Pt is still considered one of the best catalysts, the production rate of ROS can accelerate the degradation of the device's components.^{96,97} Thus, the in situ measurement of ROS by using the described

method can provide insights about different electrocatalysts, aiding in predictions of the durability of electrochemical devices, for example.

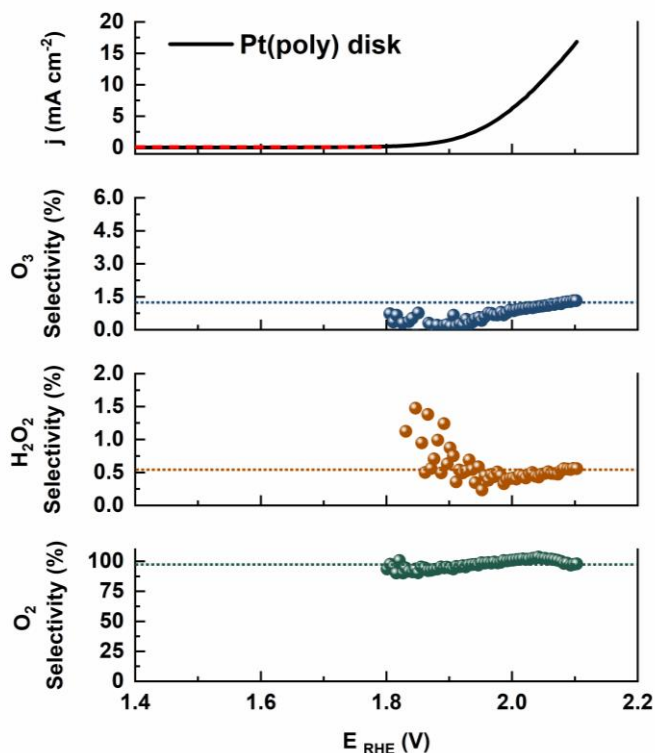


Figure 3.4. Simultaneous monitoring of electrode current (top, black), O₃ selectivity (top middle plot), H₂O₂ selectivity (bottom middle plot), and O₂ selectivity (bottom plot) during a cyclic voltammetry experiment Pt(poly) in 0.1 mol L⁻¹ H₂SO₄ electrolyte. The scan rate for both RRDE was 50 mv s⁻¹, the rotation rate was 900RPM.

For electrochemical water remediation purposes, neutral and alkaline conditions are preferable due to their environmental compatibility and slower electrode corrosion rates compared to acidic mediums.^{14,98} Additionally, NaHCO₃ and Na₂CO₃ electrolytes have been shown enhanced selectivity for reactive oxygen species (ROS) generation.⁸⁸ Thus, to broaden the applicability of RRDE method to distinguish the three oxygenated species across different electrolytes with different pHs, we replicated the experimental protocol described (0.1 mol L⁻¹ H₂SO₄) to 0.1 mol L⁻¹ NaHCO₃ (pH = 8.3) (Figure S3.3), 0.1 mol L⁻¹ Na₂CO₃ (pH = 10.70) (Figure S3.4) and NaOH (pH = 13) (Figure S3.5) electrolytes. Figure 3.5A illustrates how pH affects the current density related to the 2e⁻ reduction, measured at 0.94V vs RHE. At pH 8.3 in 0.1 mol L⁻¹ NaHCO₃ we observed a nearly 50% decrease in the cathodic diffusion limiting

current density compared to that measured in $0.1 \text{ mol L}^{-1} \text{ H}_2\text{SO}_4$. This reduction becomes more pronounced at $\text{pH} = 10.7$ ($0.1 \text{ mol L}^{-1} \text{ Na}_2\text{CO}_3$) and at $\text{pH} 13$ the current density approaches zero and remains unaffected by the rotation rate. We attributed this current drop to the chemical stability of ozone in less acidic pHs. To confirm the availability of O_3 in the electrolyte, we quantified the saturated electrolytes using the indigo method. Figure 3.5B displayed the O_3 concentration dependence across different pH's. As expected, the decline in O_3 diffusion limiting current was a consequence of the decrease in the O_3 bulk concentration. This decrease is related to the instability of ozone at pHs above 6, where it chemically decomposes according to the reaction $:\text{O}_3 + \text{H}_2\text{O} \rightarrow \text{O}_2 + \bullet\text{OH} + \text{OH}^-$.⁹⁹

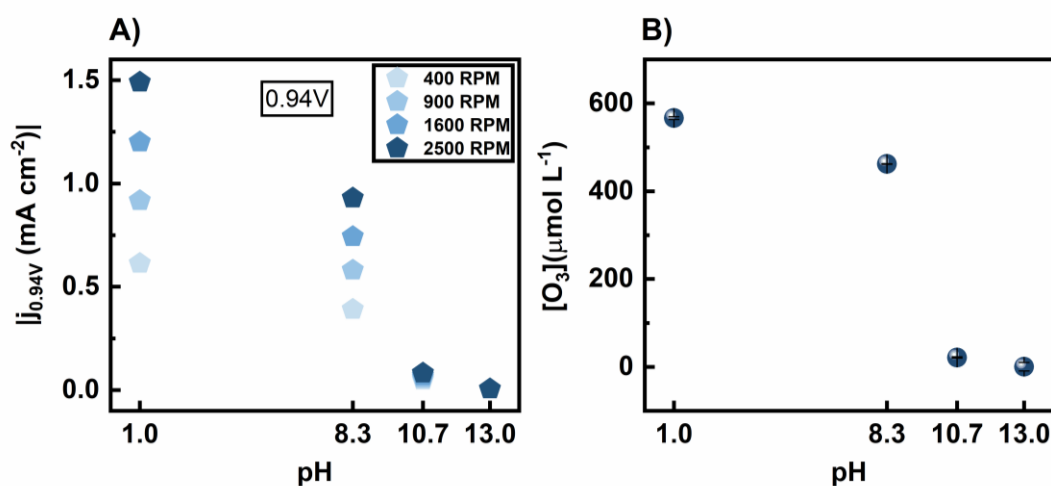


Figure 3.5. A) Absolute diffusion limiting current at 0.94V vs RHE in different pH's under O_3 saturation. B) O_3 bulk concentration determined by the Indigo method⁹⁴ in different pH's.

3.4. Conclusions

In this study, we developed an in-situ method using RRDE to identify and quantify the presence of O_3 , H_2O_2 and O_2 during water oxidation by employing a RRDE setup. By applying simple current deconvolution was possible to isolate the contribution of each of the three oxygenated species. Additionally, this approach enabled the identification of ROS formation on Pt electrode which is considered an electrocatalysts with low selectivity for these molecules.

Moreover, the presented approach shows a pH versatility which works well in a range between 1 and 8.3. This pH flexibility allows the method to be applied to a wide variety of systems, including fundamental studies on electrochemical devices, evaluations of catalyst

capabilities for water remediation systems, and the optimization of catalytic processes in different environmental conditions. Additionally, this method enhances the accuracy and efficiency of detecting reactive oxygen species, which are often unstable and prone to rapid decomposition under certain environmental conditions. By preventing the underestimation of their production, this method significantly contributes to advancements in electrochemical research and practical applications in electrochemical devices for energy storage and conversion such as water treatment technologies.

Chapter 4: Study of Metal oxides stability during reactive oxygen species generation (ROS)

4.1. Introduction

Due to increasing global energy demand and availability of alternative energy sources (i.e., wind and solar energy), the need for sustainable, well understood, electrocatalytic systems have also increased due to their potential to provide solutions to support a viable energy economy¹⁰⁰. The oxygen evolution reaction (OER) has been a major area of study within electrocatalysis to produce hydrogen gas from water and is considered the limiting reaction for water splitting due to the coupled reaction that involves $4e^-$ and $4H^+$ with slow kinetics and a high overpotential 1.23 V vs reversible hydrogen electrode (RHE).^{101,102} Besides the thermodynamic barrier of the reaction, the most common anode materials suffer substantial corrosion and deactivation that affect the lifetime and viability of the catalyst⁴⁰. In the context of an OER system employing a metal oxide electrocatalyst, a noteworthy phenomenon emerges wherein the evolved oxygen gas (O_2) is not derived from the oxygen atoms within water, but rather originates intrinsically from the metal oxide lattice.³⁹ Kasian et al.⁴¹ showed experimentally that the corrosion phenomena in IrO_2 anodes in OER condition is followed by the appearance of metal oxide lattice oxygen evolution resulting in a structural and compositional changes which affect the catalyst lifetime. Binniger et al.³⁹, have proved using thermodynamic considerations an universal correlation between oxygen evolution onset potential and metal oxide instability. According to their claims, the O_2 evolution reaction could originate from either adsorbed oxygen anions from the electrolyte or from oxygen anions in the metal oxide lattice, what they called Lattice Oxygen Evolution Reaction (LOER).

The lattice corrosion process have been explored mostly for more efficient OER metals oxides such RuO_2 and IrO_2 ^{41,103} but has not been heavily studied for less OER active materials, specifically metal oxides that are more selective toward the production of reactive oxygen species (ROS), such as, H_2O_2 , $\bullet OH$, $\bullet OOH$ and O_3 .^{14,104} Lead dioxide (PbO_2), tin oxide (SnO_2), titanium oxide (TiO_2) are known as active catalyst to produce these species¹⁰⁵⁻¹⁰⁷. ROS has been suggested to be able to remediate resistant pollutants in water due to their oxidative nature¹⁴. Being responsible for breaking down organic molecules selectively to different compounds that may have market value or burning these pollutants to CO_2 and water.^{34,108} The generation of ROS can be categorized into two distinct approaches: ex-situ and in-situ, as already described in the section 1.1.⁷ In the ex-situ process involves the generation of hydroxyl radicals through Fenton chemistry by adding external reagents, such as H_2O_2 and Fe^{2+} . On the other hand, the in-situ method consists in generating these hydroxyl radicals on the catalyst surface through water oxidation, without any chemical input, reducing the operational cost. In

this case the anode material nature will impacts on the selectivity for the ROS.^{7,34,109} Thus, the electrochemical generation of highly oxidative species that can act as mediators to break down organic pollutants emerges as a promising and simpler strategy for water remediation systems,³⁴ particularly for trace resistant pollutants as Bisphenol A (BPA) and Per- and Polyfluoroalkyl substances (PFAS).^{110,111} However, considering that the universal instability of metal oxide during OER regime can extend to metal oxides used for ROS production, it is essential to understand how these materials are affected. Gaining insights into their behavior can help develop strategies to avoid or minimize anode deactivation and, consequentially, overcome the economic challenges associated with the stability of electrocatalysts applied for water cleaning process.

To understand these trends in electrodes used for water remediation, we probed the correlation between corrosion of metal oxides (PbO₂, TiO₂ SnO₂ and FTO) and their selectivity for ROS production. Using a Rotating Ring Disk Electrode (RRDE) setup, we monitored in situ the oxygen evolution and hydrogen peroxide production while applying an anodic potential. To study structure-stability relationships under the same conditions, we used a Stationary Probe Rotating Disk Electrode (SPRDE) coupled to a plasma mass spectroscopy (ICP-MS).⁴³ This approach provided access to the dissolution rates of these metal oxides during the OER and ROS regime. Together, these results suggest that the primary corrosion effects remain closely linked to the OER, even on less active materials for oxygen evolution, which can be tied to the high overpotentials requirement to produce ROS.

4.2. Methods

4.2.1 Metal Oxides Preparation

The electrodeposition of PbO₂ was conducted on a 6mm glassy carbon disk substrate within an electrochemical cell filled with a solution containing 0.1 mol L⁻¹ HClO₄ and 0.1 mol L⁻¹ Pb(ClO₄)₂ · H₂O in a three-electrode configuration. A glassy carbon rod and Hg/HgSO₄ served as the counter and reference electrodes, respectively, under galvanostatic conditions ($j = 2.15 \text{ mA cm}^{-2}$ for 800s). The electrodeposition was conducted under mass transport control at 1600RPM.

TiO₂ electrode was prepared by anodizing a pure 6mm titanium disk. The disk electrode was polished by using 0.3 and 0.05 μm Al₂O₃ slurry on a microfiber polishing pad and cleaned by sonicating the disk for 5 min in isopropanol (1x) followed by sonication in water (2x). The

oxide layer was made in a three-electrode cell in 0.1 mol L^{-1} NaOH under galvanostatic regime at $j = 1.77 \text{ mA cm}^{-2}$ for 1200s. The counter and the reference electrode were a glassy carbon rod and Hg/HgSO₄, respectively. The anodization was conducted under mass transport control at 1600 RPM.

For SnO₂, the same cleaning and electrochemical procedure as described for TiO₂ were used. A 6mm Sn disk was anodized by applying a constant current (1.77 mA cm^{-2}) for 1200s. All the anodization processes were conducted under mass transport control at 1600 RPM.

The 6 mm SnO₂/F (Fluorine-doped Tin Oxide) disk was procured from Solaronix. The FTO layer was deposited onto fused quartz disks, ensuring a uniform electrode resistivity of 10 ohms/square.

4.2.2 Characterization

Electrode surface characterization was made by scanning electron microscopy (SEM). The images were acquired in a ZEISS Gemini SEM 300 Magnification between 10-1M, Acceleration Voltage 0.02-30kV and probe current between 3pA-20nA. For the images collection the microscope was operated at 5.00 kV, the aperture used was 30 μm with a working distance of 10 mm between the beam and the sample.

4.2.3 Electrochemical Measurements

Electrochemical measurements were performed using a Metrohm Autolab PGSTAT302N electrochemical workstation configured with three electrodes. The counter and reference electrodes employed were a glassy carbon rod and Hg/HgSO₄, respectively. The working electrodes consisted of metal oxides prepared in different substrates, PbO₂, TiO₂, SnO₂, and SnO₂/F. We use 0.1 mol L^{-1} of NaOH as support electrolyte. A fluoropolymer-based cell was used to avoid contamination from glass components in the alkaline electrolyte. To prevent any potential contamination from prior experiments, the cell underwent a rinsing process with deionized (DI) water, followed by boiling DI water. OER and ROS measurements were carried out by cycling the metal oxide electrodes up to 1.8V versus RHE. All the reported currents were normalized by the geometric area of the substrate (0.283 cm^2).

4.2.4 Quantification of O₂ and H₂O₂ Trough (RRDE)

Since the pH of the electrolyte used in this work is around 13 was not possible to track the formation of O₃ and the equations were simplified. Thus, to quantify the oxygen and hydrogen peroxide production and determine the Faradaic efficiency for both, we just measured two potential regions. for FE measurements of O₂ and H₂O₂ we held the ring potential at 0.4 V and 1.2 V vs RHE, respectively. At 0.4 V vs RHE O₂ is reduced under diffusional control. For H₂O₂, at 1.2V vs RHE is a sufficiently high potential for H₂O₂ oxidation in the diffusion-limiting region and remaining below the thermodynamic potential for O₂ evolution (1.23V vs RHE).

$$FE_{Oxygen} = \frac{O_2 \text{ evolution current (ring}_{0.4V})}{Total \text{ current (disk)}} \cdot Collection \text{ efficiency}$$

$$FE_{Hydrogen \ Peroxide} = \frac{H_2O_2 \text{ evolution current (ring}_{1.2V})}{Total \text{ current (disk)}} \cdot Collection \text{ efficiency}$$

4.2.5 In situ Inductively Coupled Plasma Mass Spectrometry (ICP-MS)

To evaluate the metal oxide electrode stability, we employed a Stationary Probe Rotating Disk Electrode (SPRDE) setup (Figure a), able to collect a fraction of dissolved ions from the electrode surface and analyze them at the Inductively Coupled Plasma Mass Spectrometry (ICPMS) instrument as described in a previous report (These measurements were conducted at Argonne National Laboratory (ANL)).⁴³ The probe was positioned less than 1 mm from the edge of the electrode. The ion collection efficiency (N) is an important parameter that depends on the rotation rate, with 100 RPM (the same rate used in this work) N is approximately 25%. To ensure the overall cell volume remains constant, a refill bottle pumps electrolyte into the cell at the same rate as the electrolyte is pumping out from the cell to the ICP-MS instrument which is around 7.5 uL s⁻¹, this configuration has a delay time around 5.5 s. To keep consistency between the measurements an external trigger signal from the potentiostat is sent to initiate the ICP-MS procedure. Metal ions present on the above-mentioned surfaces such as Pb (208 amu), Ti (49 amu), and Sn (120 amu), were detected with a PerkinElmer NexION 300D spectrometer. Electrochemical measurements were conducted at the same experimental protocol as described in 3.2.3 section.

Stationary Probe Rotating Disk Electrode (SPRDE)

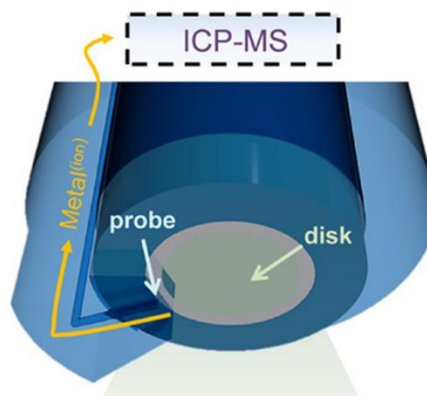


Figure 4.1. Schematic representation of the Stationary Probe Rotating Disk Electrode (SPRDE) used in this work. Adapted from [43]

4.3. Results and Discussion

Electrochemical water remediation stands out as a sustainable method for water purification and the recovery of valuable molecules. However, the high cost of electrocatalysts capable of producing reactive oxygen species (ROS) in situ, such as boron-doped diamond (BDD), currently renders the technology economically unattractive.¹¹² Nevertheless, the utilization of cheaper materials shows promise, as it is already known that some metal oxides can generate these species. However, the stability and durability of these materials for long-term applications remain unclear and require further investigation. Thus, gaining insights into the activity and stability of materials used for water remediation can aid in the design of more cost-effective electrocatalysts.³⁷

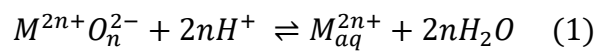
Binniger at al.³⁹ stated that during oxygen evolution condition on metal oxides the electrocatalyst universally suffers from instability due to the LOER. Considering the possibility that ROS production pathways can share similar active sites on metal oxides as the OER, we can extend the universal thermodynamic considerations to different oxygenated species production. Following the Binniger at al.³⁹ thermodynamic analyzes we aimed to establish a possible correlation between ROS formation and the participation of lattice oxygen anions in the reaction, which we named LROS. These processes are described below by the half-reactions in terms of chemical potential for each species.

Table 1 shows the OER and ROS half reactions from the electrolyte that should be considered and their thermodynamic potential.

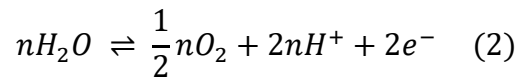
Table 1. Half reactions and their thermodynamic potentials for reactive oxygen species in water.^{91,113}

OER and ROS	Thermodynamic Potential (V vs. NHE)
$H_2O \rightleftharpoons \frac{1}{2}O_2 + 2H^+ + 2e^-$	1.23
$3H_2O \rightleftharpoons O_3 + 6H^+ + 6e^-$	1.51
$2H_2O \rightleftharpoons H_2O_2 + 2H^+ + 2e^-$	1.78
$H_2O \rightleftharpoons \bullet OH + H^+ + e^-$	2.59
$2H_2O \rightleftharpoons \bullet OOH + 3H^+ + 3e^-$	1.66

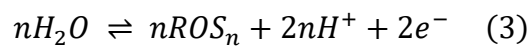
As already described in the literature,³⁹ considering a metal oxide MO_n interfacing an electrolyte, the first step involves chemical dissolution of the metal (Equation 1). This occurs under equilibrium conditions, where initially, the electrolyte doesn't have any metal ions, and due to a difference in the concentration, the metal can dissolve until achieve the equilibrium concentration.



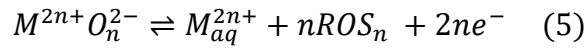
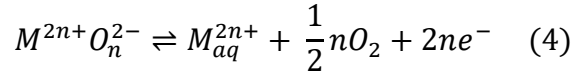
The second process to be considered is the OER from the water splitting (Equation 2)



In this step we can introduce a genal equation for ROS generation from water, where $nROS_n$ represents H_2O_2 , $\bullet OH$, $\bullet OOH$ and O_3 : (Equation 3)



The third assumption is the lattice oxygen evolution (LOER) or lattice reactive oxygen species generation (LROS)



According to the chemical equilibrium between the species involved in the metal chemical dissolution OER, and LOER (Equation 6a, 7b and 8c) the half equation for each species could be expressed in terms of their (electro)chemical potentials as already showed by Binninger et al.³⁹.

$$\mu_{MO_n}^{eq} + 2n\mu_{H^+}^{eq} = \mu_{M_{aq}^{2n+}}^{eq} + n\mu_{H_2O}^{eq} \quad (6a)$$

$$n\mu_{H_2O}^{eq} = \frac{1}{2}n\mu_{O_2}^{eq} + 2\mu_{H^+}^{eq} + 2n\mu_{e^-}^{eq} \quad (7b)$$

$$\mu_{MO_n}^{eq} = \mu_{M_{aq}^{2n+}}^{eq} + \frac{1}{2}n\mu_{O_2}^{eq} + 2n\mu_{e^-}^{eq} \quad (8c)$$

Thus, using this same assumption we can express these three processes for other oxygenated species, in this case for the ROS. Where we tried to respect the same equilibrium conditions for all the species listed below. For ozone (O_3) we have the follow correlation:

$$3\mu_{MO_n}^{eq} + 6n\mu_{H^+}^{eq} = 3\mu_{M_{aq}^{2n+}}^{eq} + 3n\mu_{H_2O}^{eq} \quad (9a)$$

$$3\mu_{H_2O}^{eq} = n\mu_{O_3}^{eq} + 6\mu_{H^+}^{eq} + 6n\mu_{e^-}^{eq} \quad (10b)$$

$$3\mu_{MO_n}^{eq} = 3\mu_{M_{aq}^{2n+}}^{eq} + n\mu_{O_3}^{eq} + 6n\mu_{e^-}^{eq} \quad (11c)$$

The hydrogen peroxide (H_2O_2),

$$2\mu_{MO_n}^{eq} + 4n\mu_{H^+}^{eq} = 2\mu_{M_{aq}^{2n+}}^{eq} + 2n\mu_{H_2O}^{eq} \quad (12a)$$

$$2n\mu_{H_2O}^{eq} = n\mu_{H_2O_2}^{eq} + 2\mu_{H^+}^{eq} + 2n\mu_{e^-}^{eq} \quad (13b)$$

$$2\mu_{MO_n}^{eq} + 2n\mu_{H^+}^{eq} = 2\mu_{M_{aq}^{2n+}}^{eq} + n\mu_{H_2O_2}^{eq} + 2n\mu_{e^-}^{eq} \quad (14c)$$

The hydroxyl radical ($\bullet OH$),

$$\mu_{MO_n}^{eq} + 2n\mu_{H^+}^{eq} = \mu_{M_{aq}^{2n+}}^{eq} + n\mu_{H_2O}^{eq} \quad (15a)$$

$$n\mu_{H_2O}^{eq} = n\mu_{\bullet OH}^{eq} + \mu_{H^+}^{eq} + \mu_{e^-}^{eq} \quad (16b)$$

$$\mu_{MO_n}^{eq} + n\mu_{H^+}^{eq} = \mu_{M_{aq}^{2n+}}^{eq} + n\mu_{\bullet OH}^{eq} + \mu_{e^-}^{eq} \quad (17c)$$

The hydroperoxy radical ($\bullet OOH$),

$$2\mu_{MO_n}^{eq} + 4n\mu_{H^+}^{eq} = 2\mu_{M_{aq}^{2n+}}^{eq} + 2n\mu_{H_2O}^{eq} \quad (18a)$$

$$2n\mu_{H_2O}^{eq} = n\mu_{\bullet OOH}^{eq} + 3\mu_{H^+}^{eq} + 3\mu_{e^-}^{eq} \quad (19b)$$

$$2\mu_{MO_n}^{eq} + n\mu_{H^+}^{eq} = 2\mu_{M_{aq}^{2n+}}^{eq} + n\mu_{\bullet OOH}^{eq} + 3\mu_{e^-}^{eq} \quad (20c)$$

The presented equations show that chemical equilibrium of OER, ROS, metal oxide dissolution, LOER and LROS are linked by their (electro)chemical potential. In this condition the LOER and LROS are not expressive since the equilibrium a and b are kept. However, when an overpotential is applied to promote OER and/or ROS, the equilibrium condition is not more hold. Thus, the equilibrium condition in the equation b for any specie generated is dislocated to the right side, and consequently condition a and c cannot be satisfied anymore, unless at least one of those two processes are dislocated to a non-equilibrium regime as well. Therefore, the LOER and LROS will be thermodynamically more favorable. Using the (electro)chemical

potentials from equation 1, the metal dissolution could be expressed in terms Gibbs free energy of the reaction (Equation 21).

$$\Delta G_{Dissolution}^R = \mu_{M_{aq}^{2n+}} + n\mu_{H_2O} - \mu_{MO_n} - 2n\mu_{H^+} \leq 0. \quad (21)$$

As mentioned, the metal dissolution in the electrolyte will always happen due to the concentration gradient between the metal oxide and electrolyte, which explain the $\Delta G_{Dissolution}^R \leq 0$.³⁹ So, under the OER and ROS condition the thermodynamic driven force for the ΔG_{LOER}^R and ΔG_{LROS}^R is equal or even more negative than the thermodynamic driven for the for the ΔG_{OER}^R and ΔG_{ROS}^R .

$$\Delta G_{OER}^R = \frac{1}{2}n\mu_{O_2} + 2n\mu_{H^+} + 2\mu_{e^-} - n\mu_{H_2O} \quad (22)$$

$$\begin{aligned} \Delta G_{LOER}^R &= \frac{1}{n} \left(\mu_{M_{aq}^{2n+}} + \frac{1}{2}n\mu_{O_2} - 2n\mu_{e^-} - \mu_{MO_n} \right) \\ \Rightarrow \Delta G_{LOER}^R &= \Delta G_{OER}^R + \frac{1}{n} \Delta G_{Dissolution}^R \leq \Delta G_{OER}^R \quad (23) \end{aligned}$$

The same is valid for ROS:

$$\Delta G_{ROS}^R = nROS_n + 2n\mu_{H^+} + 2\mu_{e^-} - n\mu_{H_2O} \quad (24)$$

$$\begin{aligned} \Delta G_{LROS}^R &= n \left(\mu_{M_{aq}^{2n+}} + nROS_n - 2n\mu_{e^-} - \mu_{MO_n} \right) \\ \Rightarrow \Delta G_{LROS}^R &= \Delta G_{ROS}^R + n\Delta G_{Dissolution}^R \leq \Delta G_{ROS}^R \quad (25) \end{aligned}$$

Under an overpotential condition for OER and/or ROS the oxygens atoms from the lattice will participate effectively in the reaction. Thus, the metal oxide will always be thermodynamically unstable. Considering the electrochemical potential for each possible species generated (Table 1). The OER will be more favorable than ROS formation, this means that $\Delta G_{LOER}^R \leq \Delta G_{LROS}^R$. However, practically this might not work for every metal oxide, particularly for metal oxides that have high overpotential for OER, for example PbO_2 and SnO_2 .¹⁴ Comninellis et al.³⁴ proposed a mechanism related to hydroxyl radicals from water adsorbed on the surface of the anode. If the hydroxyl radicals interact with the lattice oxygen

(chemisorbed) the material was considered “active”, on the other hand “non-active” anodes the interaction of the radical with the lattice is not effective (physisorbed). According to this mechanism, anodes with low oxygen evolution overpotential, such as RuO_2 and IrO_2 , are prone to LOER, while anodes that present a higher overpotential for OER, such as PbO_2 the LOER and LROS may impact less the dissolution rate of the metal, since these species can be formed early not being necessary to go to high overpotentials for OER.

To experimentally test this theoretical correlation on metal oxides that are more selective for ROS, we quantified the possible formation of H_2O_2 , and we also monitored O_2 using RRDE measurements. To differentiate these species, we screened the potential range where we have faradaic current related to oxidation or reduction for H_2O_2 and reduction of O_2 . Figure 4.2 shows the diffusion-limiting currents at different rotation rates for two distinct experimental conditions. The green lines represent an O_2 -saturated 0.1 mol L^{-1} NaOH solution, while the orange lines correspond to an Ar-saturated 0.1 mol L^{-1} NaOH solution with 1 mmol L^{-1} of H_2O_2 . As shown in Figure 3.2 at potentials below 0.6 V vs RHE either O_2 or H_2O_2 have contribution on the cathodic current. However, at potentials above 0.9 V vs. RHE, an anodic current is observed only in the presence of 1 mmol L^{-1} H_2O_2 . The thermodynamic potential for H_2O_2 generation by 2e^- water oxidation 1.76 V vs RHE being sufficiently positive to oxidize H_2O_2 to O_2 (0.68 V vs RHE) between 0.9 V and 1.4 V vs RHE. Thus, since O_2 does not exhibit any electrochemical answer at higher potentials than 0.9 V vs RHE, to probe H_2O_2 we fixed the potential on the Pt ring electrode at 1.2 V vs RHE while for O_2 quantification the potential was held at 0.4 V vs RHE. As already stated in Chapter 3.

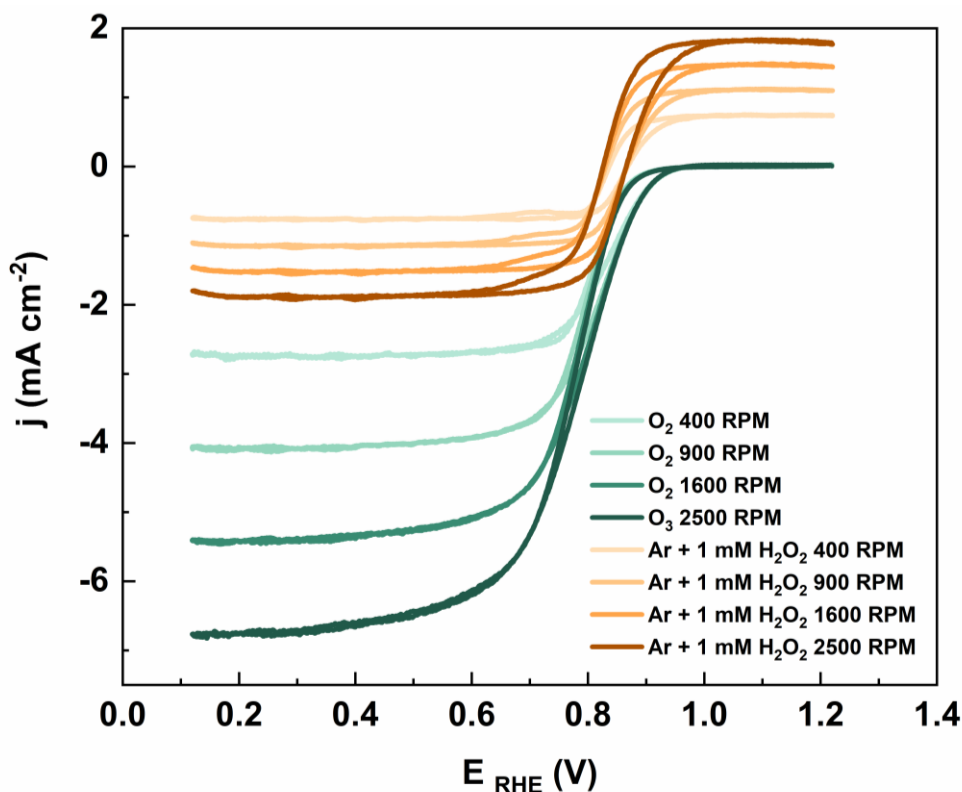


Figure 4.2. Cyclic voltammograms in O₂ saturated 0.1 M NaOH (dashed lines) and 0.1 mol L⁻¹ NaOH containing 1 mmol L⁻¹ H₂O₂ (under Ar) (solid lines) using polycrystalline Pt electrode, under mass transport control.

The RRDE and in situ ICP-MS measurements were performed using 6mm disks of PbO₂, TiO₂, SnO₂ and SnO₂/F (Figure S4.1, S4.2 and S4.3). The RRDE experiment was performed at 900RPM while the ICP-MS measurements were made in 100RPM.

Figure 4.3 displays the results of simultaneously monitoring the rates of O₂ and H₂O₂ production through the RRDE and the rates of metal dissolution using the SPRDE coupled to an ICP-MS spectrometer of TiO₂, PbO₂ in 0.1 mol L⁻¹ NaOH. In Figure 4.3A, although we observe oxidation currents for PbO₂ only above 1.9 V vs RHE, monitoring the ring current at two different potentials reveals close to 100% selectivity towards O₂ evolution + ROS and below 0.2% for H₂O₂ up to 2.2 V, while the onset of metal dissolution occurs above 2.1V vs RHE. At potentials below 1.9V vs. RHE, we couldn't measure any significant current on the ring when it was held at 0.4V vs. RHE, which might suggest no formation of •OH. However, despite the lack of current below 1.9V vs. RHE, we cannot discard the formation of •OH species on the PbO₂ surface, as this could be related to the detection limit of the technique. Additionally, no metal dissolution was probed below this same potential. However, when this electrocatalyst

is applied for organic degradation, the reported current densities typically range between 5 mA cm⁻² and 140 mA cm⁻².^{15,114-116} Based on our results, these current densities are sufficiently high to trigger the metal dissolution. Which is a concern for environmental application due to the release of heavy metal.¹¹⁷ By examining the formation of oxygenated species, we find that the selectivity for OER+ROS above 2.0V vs. RHE is close to 100%. Given that thermodynamically OER is more favorable than ROS, we can assume that the species detected on the ring in the overpotential regime are mostly O₂. Thus, the observed electrode corrosion agrees with the theoretical explanation about the LOER process.³⁹

TiO₂ is also considered a candidate to produce ROS from water oxidation.^{106,118} For example, though theoretical analysis the onset potential for H₂O₂ generation on a TiO₂ anode is around 2.27 V.¹⁰⁶ Experimentally this onset potential is even higher.¹¹⁸ Figure 4.3B displays the faradaic current, the metal oxide selective for O₂ + ROS and H₂O₂ and Ti corrosion over the applied potential. The results showed that even at significantly higher overpotentials than those applied for PbO₂, where TiO₂ anodes can generate H₂O₂, only a small current was observed above 2.5 V vs RHE. Under these experimental conditions, neither O₂ nor H₂O₂ was detected on the ring. Additionally, analysis of the dissolution rate as a function of potential revealed no significant Ti dissolution, even at potentials above 3V vs. RHE, indicating excellent stability of the metal oxide at high potentials. The absence of both OER on the electrode and metal dissolution further supports the theoretical assumption of the stability of the electrocatalyst during oxygenated species generation.³⁹

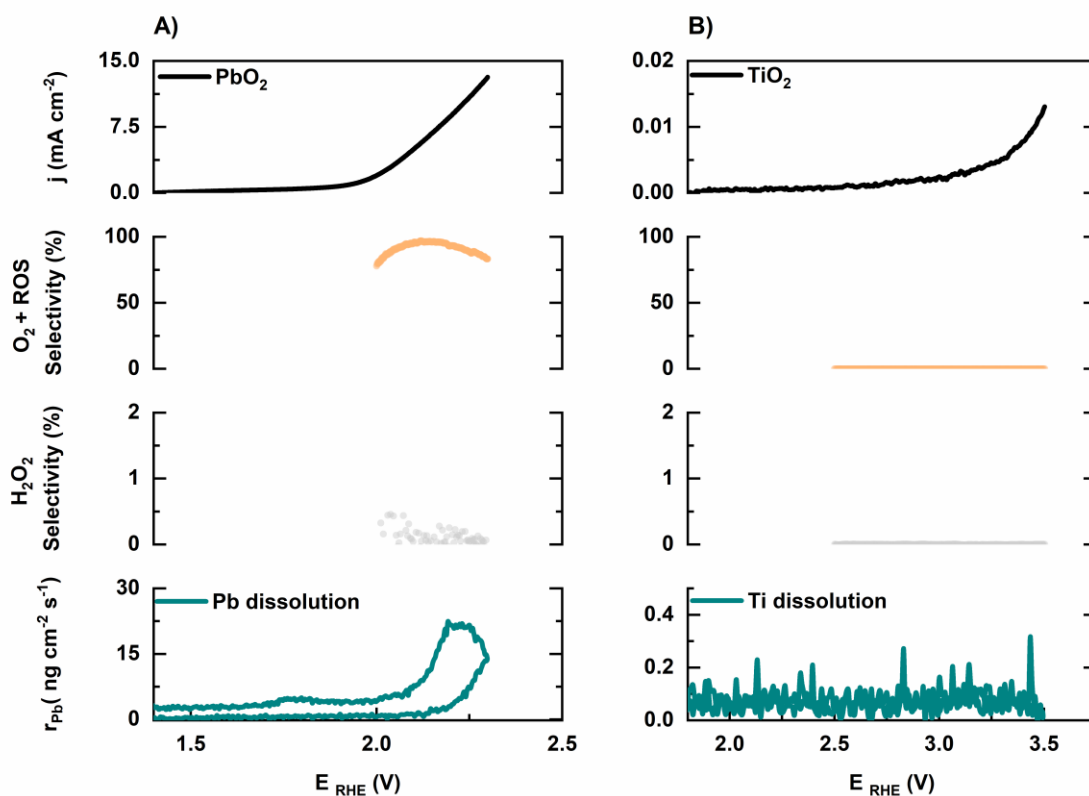


Figure 4.3. Simultaneous monitoring of electrode current (top, black), O₂ selectivity (top, middle plots), H₂O₂ selectivity (bottom middle plots), and metal dissolution rates during a cyclic voltammetry experiment on A) PbO₂ and B) TiO₂, surfaces in 0.1 mol L⁻¹ NaOH electrolyte. The scan rate for both RRDE and in situ ICP-MS were 50 mv s⁻¹.

We also conducted the investigation of H₂O₂ production on SnO₂ that are considered an active oxide for two-electron water oxidation (Figure 4.4A).^{106,119} Similar to TiO₂, a discernible current density was only observed above 2.5 V vs RHE. Examining the currents obtained when the ring was held at 0.4V vs RHE, we noted an 100% yield above 3.2V vs RHE, and the selectivity for H₂O₂ was approximately 1.5% at the same potential, this means that the selectivity for O₂ is still close to 100%. Metal dissolution was triggered at 2.7V vs. RHE, where the OER begins. As observed for lead dioxide this trend underscores the susceptibility of the metal oxide to instability during both OER and ROS production. Therefore, in this case, the detection of H₂O₂ suggests that both LOER and LORS can contribute to the metal instability. Additionally, we examined the impact of fluorine doping on the activity-stability relationship of SnO₂. Differentially from pure SnO₂, FTO (Figure 4.4B) presented an onset potential for oxygen evolution around 2.2V vs RHE while H₂O₂ selectivity hit the maximum value (~2%) around the same potential and decreases at higher overpotential indicating an optimal potential

window for H₂O₂ production. Furthermore, the dopant enhances the stability of FTO, as evidenced by measuring the dissolution rate of Sn during the anodic scan. Even under overpotential conditions, the loss of Sn was at least 100 times lower than that observed in undoped SnO₂. This outcome aligns with expectations, given the widespread use of FTO as a substrate owing to its inherent stability.¹²⁰ These results suggest that O₂ evolution is still present even on materials that require very high overpotentials, and the metal dissolution might be intrinsically tied to the formation of O₂, and ROS as expected from thermodynamic considerations described.

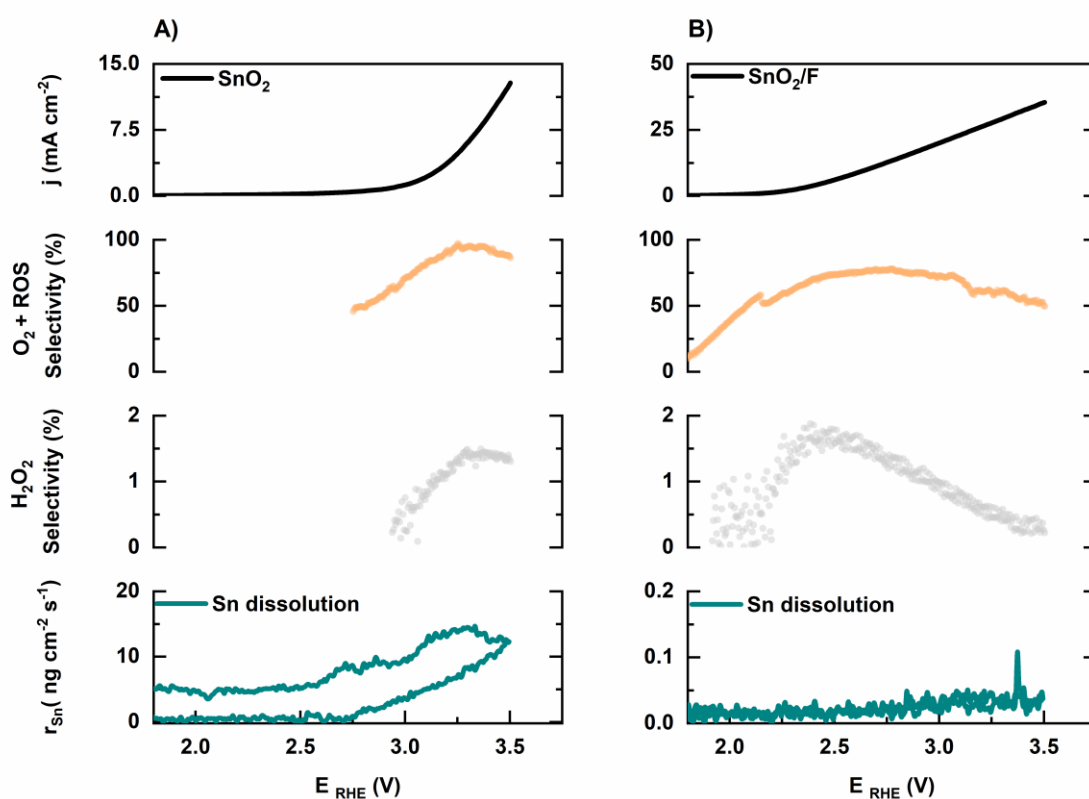


Figure 4.4. Simultaneous monitoring of electrode current (top, black), O₂ selectivity (top, middle plots), H₂O₂ selectivity (bottom middle plots), and metal dissolution rates during a cyclic voltammetry experiment on A) SnO₂ and B) FTO, surfaces in 0.1 mol L⁻¹ NaOH electrolyte. The scan rate for both RRDE and in situ ICP-MS were 50 mV s⁻¹.

4.4. Conclusions

In this study, we have introduced a comprehensive approach for the simultaneous measurement of activity, selectivity, and stability across various metal oxides with the capability to generate ROS, showcasing their potential as catalysts for water remediation. Having access

to the relationship between these three variables gives the ability to think of strategies to control them. Specifically, our findings illustrate that incorporating a dopant into the metal oxide structure enhances both activity and stability while mitigating electrode corrosion. Furthermore, insights gained from stability assessments during operation offer a strategic advantage by averting the use of catalysts prone to releasing heavy metals, thereby preventing contributions to water contamination, as exemplified by PbO_2 . This multifaceted methodology Which can be align with other physical chemical characterization technics holds promise for advancing the development of efficient and environmentally friendly catalysts for water remediation applications.

Chapter 5: Final Remarks

5.1. General Conclusion

In this work, we underscore the critical importance of comprehending the activity and stability of materials used in electrochemical water remediation. Considering the rapid population growth and industrial expansion in recent years, which have heightened concerns about environmental sustainability due to increased release of pollutants. The demand for water cleaning processes tends to increase. Electrochemical water remediation stands out due to its versatility which allows either reduction or oxidation of these pollutants. Additionally, this technology offers a sustainable alternative capable of purifying water while simultaneously producing valuable products. Overall, the presented results aimed to cover key aspects of electrochemical reduction and oxidation reactions that are critical for the rational design of materials that exhibit improved performance.

In Chapter 2, we studied the dynamic changes on the structure and composition of well-defined Cu_2O NCs during electroreduction of nitrate to ammonia. After the reaction, electron microscopies revealed the loss of the cubic shape with the formation of sintered domains. In situ Raman, X-ray diffraction (XRD) and in situ Cu K-edge X-ray absorption near edge spectroscopy (XANES) indicated the Cu_2O reduction to oxide-derived Cu^0 (OD-Cu). Nevertheless, a remaining Cu_2O phase was noticed after 1-hour electrolysis at -0.3 V vs. RHE. This observation indicated that the activity and selectivity of the initially well-defined Cu_2O NCs are not solely dependent on the initial structure. Instead, it underscored the emergence of an OD-Cu rich surface, evolving from near-surface to underlying layers over time, playing a crucial role in the reaction pathways. By employing online differential electrochemical mass spectrometry (DEMS) and in situ Fourier transform infrared spectroscopy (FTIR) we experimentally probed the presence of key intermediates (NO and NH_2OH) and byproducts of NO_3RR (N_2 and N_2H_x) for NH_3 formation. These results show a complex relationship between activity and stability of nanostructured Cu_2O oxide catalyst for NO_3RR .

In Chapter 3, we applied the RRDE method to quantify ROS generated during water oxidation. This approach enabled us to identify and quantify in situ species such as O_3 and H_2O_2 , which are crucial for water purification technologies. Based on the results, this approach can also provide insights that help predict the durability of electrochemical used in various energy storage and conversion processes. Furthermore, the method demonstrated effectiveness across a pH range of 1 to 8.3, reinforcing its versatility and broad applicability.

In Chapter 4, we combined the RRDE method described in Chapter 3 with in-situ ICP-MS to investigate the activity and stability trends of metal oxides used in the electrochemical oxidation of pollutants capable of generating ROS. Our findings revealed that the intrinsic thermodynamic link between oxygen evolution and metal corrosion extends to the production of other oxygenated species, which might influence material performance. Finally, we showed that it is possible to mitigate metal corrosion while maintaining catalytic activity by introducing a dopant into the metal oxide structure.

Overall, this thesis underscores the importance of integrating analytical techniques with electrochemical systems to investigate the activity, selectivity, and stability of electrocatalysts. The demonstrated approaches can be utilized to probe various catalysts for water remediation, regardless of whether they involve reduction or oxidation reactions. More importantly, understanding how these processes are interconnected allows us to devise strategies to control and potentially regenerate the functionality of active sites lost during operation.

References

- 1 Hosseiny, S. H., Bozorg-Haddad, O. & Bocchiola, D. in *Economical, Political, and Social Issues in Water Resources* 189-216 (Elsevier, 2021).
- 2 Sharma, S. & Bhattacharya, A. Drinking water contamination and treatment techniques. *Applied water science* **7**, 1043-1067 (2017).
- 3 Organization, W. H. Safer water, better health. (2019).
- 4 Madhav, S. *et al.* Water pollutants: sources and impact on the environment and human health. *Sensors in water pollutants monitoring: Role of material*, 43-62 (2020).
- 5 Singh, N. & Goldsmith, B. R. Role of Electrocatalysis in the Remediation of Water Pollutants. *Acs Catalysis* **10**, 3365-3371, doi:10.1021/acscatal.9b04167 (2020).
- 6 Zhang, Z., Sarkar, D., Biswas, J. K. & Datta, R. Biodegradation of per- and polyfluoroalkyl substances (PFAS): A review. *Bioresour Technol* **344**, 126223, doi:10.1016/j.biortech.2021.126223 (2022).
- 7 Nidheesh, P. V., Zhou, M. & Oturan, M. A. An overview on the removal of synthetic dyes from water by electrochemical advanced oxidation processes. *Chemosphere* **197**, 210-227, doi:10.1016/j.chemosphere.2017.12.195 (2018).
- 8 Hublikar, L. V., Shilar, F. A., Mathada, B. S. & Ganachari, S. V. Comprehensive investigation of green solutions for sustainable wastewater remediation: a review. *Journal of Molecular Liquids*, 124532 (2024).
- 9 Ogundele, O., Oyegoke, D. & Anaun, T. Exploring the potential and challenges of electro-chemical processes for sustainable waste water remediation and treatment. *Acadlore Trans. Geosci* **2**, 80-93 (2023).
- 10 Chaplin, B. P. The Prospect of Electrochemical Technologies Advancing Worldwide Water Treatment. *Acc Chem Res* **52**, 596-604, doi:10.1021/acs.accounts.8b00611 (2019).
- 11 Anastasiadou, D., van Beek, Y., Hensen, E. J. M. & Costa Figueiredo, M. Ammonia electrocatalytic synthesis from nitrate. *Electrochemical Science Advances* **3**, e2100220-e2100220, doi:10.1002/elsa.202100220 (2022).
- 12 Li, P. P., Jin, Z. Y., Fang, Z. W. & Yu, G. H. A single-site iron catalyst with preoccupied active centers that achieves selective ammonia electrosynthesis from nitrate. *Energy & Environmental Science* **14**, 3522-3531, doi:10.1039/d1ee00545f (2021).
- 13 Duca, M. & Koper, M. T. M. Powering denitrification: the perspectives of electrocatalytic nitrate reduction. *Energy & Environmental Science* **5**, 9726-9742, doi:10.1039/c2ee23062c (2012).

- 14 Panizza, M. & Cerisola, G. Direct and mediated anodic oxidation of organic pollutants. *Chem Rev* **109**, 6541-6569, doi:10.1021/cr9001319 (2009).
- 15 Rahmani, A. *et al.* The integration of PbO₂-based EAOPs with other advanced oxidation processes for improved treatment of water and wastewater. *Current Opinion in Electrochemistry* **37**, 101204, doi:ARTN 101204, 10.1016/j.coelec.2022.101204 (2023).
- 16 Shi, H. *et al.* Degradation of Perfluorooctanesulfonate by Reactive Electrochemical Membrane Composed of Magneli Phase Titanium Suboxide. *Environ Sci Technol* **53**, 14528-14537, doi:10.1021/acs.est.9b04148 (2019).
- 17 Weber, R. S. Electrochemical upvaluing of waste plastic. *Current Opinion in Electrochemistry* **46**, 101493, doi:ARTN 101493, 10.1016/j.coelec.2024.101493 (2024).
- 18 Lu, J., Hou, R., Wang, Y., Zhou, L. & Yuan, Y. Surfactant-sodium dodecyl sulfate enhanced degradation of polystyrene microplastics with an energy-saving electrochemical advanced oxidation process (EAOP) strategy. *Water Res* **226**, 119277, doi:10.1016/j.watres.2022.119277 (2022).
- 19 Möhle, S. *et al.* Modern electrochemical aspects for the synthesis of value-added organic products. *Angewandte Chemie International Edition* **57**, 6018-6041 (2018).
- 20 Lin, L. *et al.* Nitrate contamination in drinking water and adverse reproductive and birth outcomes: a systematic review and meta-analysis. *Sci Rep* **13**, 563, doi:10.1038/s41598-022-27345-x (2023).
- 21 Wang, Z., Richards, D. & Singh, N. in *Catalysis Science and Technology* Vol. 11 705-725 (Royal Society of Chemistry, 2021).
- 22 Jia, R. *et al.* Boosting Selective Nitrate Electroreduction to Ammonium by Constructing Oxygen Vacancies in TiO₂. *ACS Catalysis* **10**, 3533-3540, doi:10.1021/acscatal.9b05260 (2020).
- 23 Min, B. *et al.* Powering the Remediation of the Nitrogen Cycle: Progress and Perspectives of Electrochemical Nitrate Reduction. *Ind Eng Chem Res* **60**, 14635-14650, doi:10.1021/acs.iecr.1c03072 (2021).
- 24 Gao, J. *et al.* Electrocatalytic Upcycling of Nitrate Wastewater into an Ammonia Fertilizer via an Electrified Membrane. *Environ Sci Technol* **56**, 11602-11613, doi:10.1021/acs.est.1c08442 (2022).
- 25 Shi, N. *et al.* Upcycling wastewater nitrate into ammonia fertilizer via concurrent electrocatalysis and membrane extraction. *Chemical Engineering Journal* **455**, 140959, doi:10.1016/j.cej.2022.140959 (2023).
- 26 Hu, T., Wang, C. H., Wang, M. T., Li, C. M. & Guo, C. X. Theoretical Insights into Superior Nitrate Reduction to Ammonia Performance of Copper Catalysts. *Acs Catalysis* **11**, 14417-14427, doi:10.1021/acscatal.1c03666 (2021).

- 27 Wang, Y., Wang, C., Li, M., Yu, Y. & Zhang, B. in *Chemical Society Reviews* Vol. 50 6720-6733 (Royal Society of Chemistry, 2021).
- 28 Fan, K. *et al.* Active hydrogen boosts electrochemical nitrate reduction to ammonia. *Nat Commun* **13**, 7958, doi:10.1038/s41467-022-35664-w (2022).
- 29 Xiong, Y. *et al.* Electrochemical nitrate reduction: ammonia synthesis and the beyond. *Advanced Materials* **36**, 2304021 (2024).
- 30 Bai, L. *et al.* Electrocatalytic Nitrate and Nitrite Reduction toward Ammonia Using Cu₂O Nanocubes: Active Species and Reaction Mechanisms. *Journal of the American Chemical Society* **146**, 9665-9678 (2024).
- 31 Costa, G. F. *et al.* Identifying the active site of Cu/Cu₂O for electrocatalytic nitrate reduction reaction to ammonia. *Chem Catalysis* **4**, 100850, doi:10.1016/j.checat.2023.100850 (2024).
- 32 Wang, Y., Zhou, W., Jia, R., Yu, Y. & Zhang, B. Unveiling the Activity Origin of a Copper-based Electrocatalyst for Selective Nitrate Reduction to Ammonia. *Angew Chem Int Ed Engl* **59**, 5350-5354, doi:10.1002/anie.201915992 (2020).
- 33 Chaplin, B. P. Critical review of electrochemical advanced oxidation processes for water treatment applications. *Environmental Science: Processes & Impacts* **16**, 1182-1203, doi:10.1039/C3EM00679D (2014).
- 34 Comninellis, C. Electrocatalysis in the Electrochemical Conversion/Combustion of Organic Pollutants for Waste-Water Treatment. *Electrochimica Acta* **39**, 1857-1862, doi:Doi 10.1016/0013-4686(94)85175-1 (1994).
- 35 Sirés, I., Low, C. T. J., Ponce-de-León, C. & Walsh, F. C. The characterisation of PbO₂-coated electrodes prepared from aqueous methanesulfonic acid under controlled deposition conditions. *Electrochimica Acta* **55**, 2163-2172, doi:https://doi.org/10.1016/j.electacta.2009.11.051 (2010).
- 36 Le, T. X. H., Haflich, H., Shah, A. D. & Chaplin, B. P. Energy-Efficient Electrochemical Oxidation of Perfluoroalkyl Substances Using a Ti₄O₇ Reactive Electrochemical Membrane Anode. *Environmental Science & Technology Letters* **6**, 504-510, doi:10.1021/acs.estlett.9b00397 (2019).
- 37 Lopes, P. P. A Framework for the Relationships between Stability and Functional Properties of Electrochemical Energy Materials. *ACS Materials Au* **3**, 8-17, doi:10.1021/acsmaterialsau.2c00044 (2023).
- 38 Anastasiadou, D. *et al.* Morphology Changes of CuO Catalysts During Nitrate Electroreduction to Ammonia. *Chemcatchem* **15**, doi:10.1002/cctc.202201503 (2023).
- 39 Binniger, T. *et al.* Thermodynamic explanation of the universal correlation between oxygen evolution activity and corrosion of oxide catalysts. *Sci Rep* **5**, 12167, doi:10.1038/srep12167 (2015).

- 40 Klyukin, K., Zagalskaya, A. & Alexandrov, V. Role of Dissolution Intermediates in Promoting Oxygen Evolution Reaction at RuO (110) Surface. *Journal of Physical Chemistry C* **123**, 22151-22157, doi:10.1021/acs.jpcc.9b03418 (2019).
- 41 Kasian, O. *et al.* Degradation of iridium oxides oxygen evolution from the lattice: correlating atomic scale structure with reaction mechanisms. *Energy & Environmental Science* **12**, 3548-3555, doi:10.1039/c9ee01872g (2019).
- 42 Queiroz, A. C. *et al.* Electrochemical Mass Spectrometry: Evolution of the Cell Setup for On-Line Investigation of Products and Screening of Electrocatalysts for Carbon Dioxide Reduction. *ChemElectroChem* **9**, e202101408 (2022).
- 43 Lopes, P. P. *et al.* Relationships between Atomic Level Surface Structure and Stability/Activity of Platinum Surface Atoms in Aqueous Environments. *Acs Catalysis* **6**, 2536-2544, doi:10.1021/acscatal.5b02920 (2016).
- 44 Messias, I. *et al.* Electrochemical mass spectrometry study of the pyridine/pyridinium in the CO₂ electroreduction reaction on copper electrodes. *Electrochimica Acta* **436**, 141445, doi:https://doi.org/10.1016/j.electacta.2022.141445 (2022).
- 45 Chung, D. Y. *et al.* Dynamic stability of active sites in hydr(oxy)oxides for the oxygen evolution reaction. *Nature Energy* **5**, 222-230, doi:10.1038/s41560-020-0576-y (2020).
- 46 Wang, Y. *et al.* Enhanced Nitrate-to-Ammonia Activity on Copper-Nickel Alloys via Tuning of Intermediate Adsorption. *J Am Chem Soc* **142**, 5702-5708, doi:10.1021/jacs.9b13347 (2020).
- 47 Jeon, T. H. *et al.* Cobalt–Copper Nanoparticles on Three-Dimensional Substrate for Efficient Ammonia Synthesis via Electrocatalytic Nitrate Reduction. *The Journal of Physical Chemistry C* **126**, 6982-6989, doi:10.1021/acs.jpcc.1c10781 (2022).
- 48 Wang, J. *et al.* Cu-Doped Iron Oxide for the Efficient Electrocatalytic Nitrate Reduction Reaction. *Nano Lett* **23**, 1897-1903, doi:10.1021/acs.nanolett.2c04949 (2023).
- 49 Fu, Y. *et al.* Enhancing Electrochemical Nitrate Reduction to Ammonia over Cu Nanosheets via Facet Tandem Catalysis. *Angew Chem Int Ed Engl* **62**, e202303327, doi:10.1002/anie.202303327 (2023).
- 50 Fang, L. *et al.* Boosting nitrate electroreduction to ammonia via generated stacking faults in oxide-derived copper. *Chemical Engineering Journal* **446**, 137341-137341, doi:ARTN 137341, 10.1016/j.cej.2022.137341 (2022).
- 51 Yu, J. Q. *et al.* Precisely Controlled Synthesis of Hybrid Intermetallic-Metal Nanoparticles for Nitrate Electroreduction. *Acs Appl Mater Inter* **13**, 52073-52081, doi:10.1021/acsami.1c09301 (2021).

- 52 Niu, Z. D. *et al.* Optimizing Oxidation State of Octahedral Copper for Boosting Electroreduction Nitrate to Ammonia. *Acs Applied Energy Materials* **5**, 3339-3345, doi:10.1021/acsaem.1c03969 (2022).
- 53 Yoshioka, T., Iwase, K., Nakanishi, S., Hashimoto, K. & Kamiya, K. Electrocatalytic Reduction of Nitrate to Nitrous Oxide by a Copper-Modified Covalent Triazine Framework. *Journal of Physical Chemistry C* **120**, 15729-15734, doi:10.1021/acs.jpcc.5b10962 (2016).
- 54 Wang, X. H. *et al.* Oxygen-Vacancy-Rich Cu₂O Hollow Nanocubes for Nitrate Electroreduction Reaction to Ammonia in a Neutral Electrolyte. *Inorg Chem* **61**, 15678-15685, doi:10.1021/acs.inorgchem.2c02716 (2022).
- 55 Yuan, J., Xing, Z., Tang, Y. & Liu, C. Tuning the Oxidation State of Cu Electrodes for Selective Electrosynthesis of Ammonia from Nitrate. *ACS Appl Mater Interfaces* **13**, 52469-52478, doi:10.1021/acsaem.1c10946 (2021).
- 56 Zhao, J. *et al.* Constructing Cu-CuO heterostructured skin on Cu cubes to promote electrocatalytic ammonia production from nitrate wastewater. *J Hazard Mater* **439**, 129653, doi:10.1016/j.jhazmat.2022.129653 (2022).
- 57 Zhou, N. *et al.* Potential-Induced Synthesis and Structural Identification of Oxide-Derived Cu Electrocatalysts for Selective Nitrate Reduction to Ammonia. *Acs Catalysis* **13**, 7529-7537, doi:10.1021/acscatal.3c01315 (2023).
- 58 Grosse, P. *et al.* Dynamic Changes in the Structure, Chemical State and Catalytic Selectivity of Cu Nanocubes during CO₂ Electroreduction: Size and Support Effects. *Angew Chem Int Ed Engl* **57**, 6192-6197, doi:10.1002/anie.201802083 (2018).
- 59 Popovic, S. *et al.* Stability and Degradation Mechanisms of Copper-Based Catalysts for Electrochemical CO₂ Reduction. *Angew Chem Int Ed Engl* **59**, 14736-14746, doi:10.1002/anie.202000617 (2020).
- 60 Pérez-Gallent, E., Figueiredo, M. C., Katsounaros, I. & Koper, M. T. M. Electrocatalytic reduction of Nitrate on Copper single crystals in acidic and alkaline solutions. *Electrochimica Acta* **227**, 77-84, doi:10.1016/j.electacta.2016.12.147 (2017).
- 61 Ren, Z. H., Shi, K. G. & Feng, X. F. Elucidating the Intrinsic Activity and Selectivity of Cu for Nitrate Electroreduction. *Acs Energy Letters* **8**, 3658-3665, doi:10.1021/acsaem.1c02319 (2023).
- 62 Qin, J. *et al.* Electrochemical Synthesis of Ammonium from Nitrates via Surface Engineering in Cu₂O(100) Facets. *ACS Applied Energy Materials* **5**, 71-76, doi:10.1021/acsaem.1c02319 (2021).
- 63 Wang, Y., Qin, X. P. & Shao, M. H. First-principles mechanistic study on nitrate reduction reactions on copper surfaces: Effects of crystal facets and pH. *Journal of Catalysis* **400**, 62-70, doi:10.1016/j.jcat.2021.05.022 (2021).

- 64 Wu, Z. Z. *et al.* Identification of Cu(100)/Cu(111) Interfaces as Superior Active Sites for CO Dimerization During CO₂ Electroreduction. *J Am Chem Soc* **144**, 259-269, doi:10.1021/jacs.1c09508 (2022).
- 65 Herzog, A. *et al.* Operando Investigation of Ag-Decorated Cu₂O Nanocube Catalysts with Enhanced CO₂ Electroreduction toward Liquid Products. *Angew Chem Int Ed Engl* **60**, 7426-7435, doi:10.1002/anie.202017070 (2021).
- 66 Deng, Y. L., Handoko, A. D., Du, Y. H., Xi, S. B. & Yeo, B. S. Raman Spectroscopy of Copper and Copper Oxide Surfaces during Electrochemical Oxygen Evolution Reaction: Identification of Cu Oxides as Catalytically Active Species. *Acs Catalysis* **6**, 2473-2481, doi:10.1021/acscatal.6b00205 (2016).
- 67 Soukup, L., Gregora, I., Jastrabik, L. & Konakova, A. Raman-Spectra and Electrical-Conductivity of Glassy-Carbon. *Mat Sci Eng B-Solid* **11**, 355-357, doi:Doi 10.1016/0921-5107(92)90240-A (1992).
- 68 Reyter, D., Bélanger, D. & Roué, L. Study of the electroreduction of nitrate on copper in alkaline solution. *Electrochimica Acta* **53**, 5977-5984, doi:10.1016/j.electacta.2008.03.048 (2008).
- 69 Winkler, M. E. G., Goncalves, R. H. & Rubira, A. F. FTIR-Assisted Electroreduction of CO₂ and H₂O to CO and H₂ by Electrochemically Deposited Copper on Oxidized Graphite Felt. *ACS Omega* **7**, 45067-45076, doi:10.1021/acsomega.2c05486 (2022).
- 70 Devaraj, M. *et al.* Fabrication of novel shape Cu and Cu/CuO nanoparticles modified electrode for the determination of dopamine and paracetamol. *Journal of Molecular Liquids* **221**, 930-941, doi:10.1016/j.molliq.2016.06.028 (2016).
- 71 Gaur, A., Shrivastava, B. & Joshi, S. in *Journal of Physics: Conference Series*. 012084 (IOP Publishing).
- 72 Möller, T. *et al.* Electrocatalytic CO₂ Reduction on CuOx Nanocubes: Tracking the Evolution of Chemical State, Geometric Structure, and Catalytic Selectivity using Operando Spectroscopy. *Angewandte Chemie* **132**, 18130-18139, doi:10.1002/ange.202007136 (2020).
- 73 Fu, W. Y. *et al.* Tuning mobility of intermediate and electron transfer to enhance electrochemical reduction of nitrate to ammonia on CuO/Cu interface. *Chemical Engineering Journal* **433**, 133680-133680, doi:ARTN 133680, 10.1016/j.cej.2021.133680 (2022).
- 74 Shi, Y. *et al.* In-situ reconstructed Cu/Cu₂O heterogeneous nanorods with oxygen vacancies for enhanced electrocatalytic nitrate reduction to ammonia. *Chemical Engineering Journal* **479**, 147574, doi:10.1016/j.cej.2023.147574 (2024).
- 75 Daiyan, R. *et al.* Nitrate reduction to ammonium: from CuO defect engineering to waste NO_x-to-NH₃ economic feasibility. *Energy & Environmental Science* **14**, 3588-3598, doi:10.1039/d1ee00594d (2021).

- 76 Han, S. H. *et al.* Ultralow overpotential nitrate reduction to ammonia via a three-step relay mechanism. *Nature Catalysis* **6**, 402-414, doi:10.1038/s41929-023-00951-2 (2023).
- 77 Zhang, R. *et al.* Electrochemical nitrate reduction in acid enables high-efficiency ammonia synthesis and high-voltage pollutes-based fuel cells. *Nat Commun* **14**, 8036, doi:10.1038/s41467-023-43897-6 (2023).
- 78 Wen, W., Yan, P., Sun, W., Zhou, Y. & Yu, X. Y. Metastable Phase Cu with Optimized Local Electronic State for Efficient Electrocatalytic Production of Ammonia from Nitrate. *Advanced Functional Materials* **33**, doi:10.1002/adfm.202212236 (2022).
- 79 Liu, H. *et al.* Efficient Electrochemical Nitrate Reduction to Ammonia with Copper-Supported Rhodium Cluster and Single-Atom Catalysts. *Angew Chem Int Ed Engl* **61**, e202202556, doi:10.1002/anie.202202556 (2022).
- 80 Kreml, K. *et al.* Quantitative operando detection of electro synthesized ammonia using mass spectrometry. *ChemElectroChem* **9**, e202101713 (2022).
- 81 Dima, G. E., de Voys, A. C. A. & Koper, M. T. M. Electrocatalytic reduction of nitrate at low concentration on coinage and transition-metal electrodes in acid solutions. *Journal of Electroanalytical Chemistry* **554**, 15-23, doi:10.1016/S0022-0728(02)01443-2 (2003).
- 82 Jung, W. S. & Hwang, Y. J. Material strategies in the electrochemical nitrate reduction reaction to ammonia production. *Materials Chemistry Frontiers* **5**, 6803-6823, doi:10.1039/d1qm00456e (2021).
- 83 Kerschbaumer, A. *et al.* How to use a rotating ring-disc electrode (RRDE) subtraction method to investigate the electrocatalytic oxygen reduction reaction? *Catalysis Science & Technology* **13**, 834-843 (2023).
- 84 Harraz, D. M., Weng, S. & Surendranath, Y. Electrochemically Quantifying Oxygen Reduction Selectivity in Nonaqueous Electrolytes. *ACS Catalysis* **13**, 1462-1469, doi:10.1021/acscatal.2c04564 (2023).
- 85 Zhou, R., Zheng, Y., Jaroniec, M. & Qiao, S.-Z. Determination of the Electron Transfer Number for the Oxygen Reduction Reaction: From Theory to Experiment. *ACS Catalysis* **6**, 4720-4728, doi:10.1021/acscatal.6b01581 (2016).
- 86 Goyal, A., Marcandalli, G., Mints, V. A. & Koper, M. T. M. Competition between CO₂ Reduction and Hydrogen Evolution on a Gold Electrode under Well-Defined Mass Transport Conditions. *Journal of the American Chemical Society* **142**, 4154-4161, doi:10.1021/jacs.9b10061 (2020).
- 87 Tackett, B. M., Raciti, D., Brady, N. W., Ritzert, N. L. & Moffat, T. P. Potentiometric Rotating Ring Disk Electrode Study of Interfacial pH during CO₂ Reduction and H₂ Generation in Neutral and Weakly Acidic Media. *The Journal of Physical Chemistry C* **126**, 7456-7467, doi:10.1021/acs.jpcc.2c01504 (2022).

- 88 Gill, T. M., Vallez, L. & Zheng, X. The Role of Bicarbonate-Based Electrolytes in H₂O₂ Production through Two-Electron Water Oxidation. *ACS Energy Letters* **6**, 2854-2862, doi:10.1021/acseenergylett.1c01264 (2021).
- 89 Zhang, K. *et al.* Near-Complete Suppression of Oxygen Evolution for Photoelectrochemical H₂O Oxidative H₂O₂ Synthesis. *Journal of the American Chemical Society* **142**, 8641-8648, doi:10.1021/jacs.9b13410 (2020).
- 90 Johnson, D. C., Napp, D. T. & Bruckenstein, S. Electrochemical reduction of ozone in acidic media. *Analytical Chemistry* **40**, 482-488, doi:10.1021/ac60259a031 (1968).
- 91 Lee, W., Kim, S. & Cho, K. Quantitative Evaluations on Ozone Evolution Electrocatalysts by Scanning Electrochemical Microscopy for Oxidative Water Treatment. *Environmental Science & Technology*, doi:10.1021/acs.est.2c05290 (2022).
- 92 Foller, P. C. & Tobias, C. W. The Anodic Evolution of Ozone. *Journal of The Electrochemical Society* **129**, 506, doi:10.1149/1.2123890 (1982).
- 93 Chen, C. & Fuller, T. H₂O₂ Formation under Fuel-Cell Conditions. *ECS Transactions* **11**, 1127, doi:10.1149/1.2781025 (2007).
- 94 Bader, H. & Hoigné, J. Determination of ozone in water by the indigo method. *Water Research* **15**, 449-456, doi:https://doi.org/10.1016/0043-1354(81)90054-3 (1981).
- 95 Vos, J. G. & Koper, M. T. M. Examination and prevention of ring collection failure during gas-evolving reactions on a rotating ring-disk electrode. *Journal of Electroanalytical Chemistry* **850**, 113363, doi:https://doi.org/10.1016/j.jelechem.2019.113363 (2019).
- 96 Trogadas, P., Parrondo, J., Mijangos, F. & Ramani, V. Degradation mitigation in PEM fuel cells using metal nanoparticle additives. *Journal of Materials Chemistry* **21**, 19381-19388 (2011).
- 97 de Bruijn, F. A., Dam, V. & Janssen, G. Durability and degradation issues of PEM fuel cell components. *Fuel cells* **8**, 3-22 (2008).
- 98 Furuya, Y. *et al.* Influence of Electrolyte Composition and pH on Platinum Electrochemical and/or Chemical Dissolution in Aqueous Acidic Media. *ACS Catalysis* **5**, 2605-2614, doi:10.1021/cs5016035 (2015).
- 99 Rodríguez-Peña, M. *et al.* New insights about the electrochemical production of ozone. *Current Opinion in Electrochemistry* **27**, 100697, doi:https://doi.org/10.1016/j.coelec.2021.100697 (2021).
- 100 Lewis, N. S. & Nocera, D. G. Powering the planet: chemical challenges in solar energy utilization. *Proc Natl Acad Sci U S A* **103**, 15729-15735, doi:10.1073/pnas.0603395103 (2006).

- 101 Li, H. Y. *et al.* Ti-Doped SnO₂ Supports IrO₂ Electrocatalysts for the Oxygen Evolution Reaction (OER) in PEM Water Electrolysis. *Acs Sustainable Chemistry & Engineering* **11**, 1121-1132, doi:10.1021/acssuschemeng.2c06368 (2023).
- 102 Vij, V. *et al.* Nickel-Based Electrocatalysts for Energy-Related Applications: Oxygen Reduction, Oxygen Evolution, and Hydrogen Evolution Reactions. *Acs Catalysis* **7**, 7196-7225, doi:10.1021/acscatal.7b01800 (2017).
- 103 Hodnik, N. *et al.* New Insights into Corrosion of Ruthenium and Ruthenium Oxide Nanoparticles in Acidic Media. *Journal of Physical Chemistry C* **119**, 10140-10147, doi:10.1021/acs.jpcc.5b01832 (2015).
- 104 Ahmed, Y., Zhong, J., Yuan, Z. & Guo, J. Roles of reactive oxygen species in antibiotic resistant bacteria inactivation and micropollutant degradation in Fenton and photo-Fenton processes. *J Hazard Mater* **430**, 128408, doi:10.1016/j.jhazmat.2022.128408 (2022).
- 105 Jeong, J., Kim, J. Y. & Yoon, J. The role of reactive oxygen species in the electrochemical inactivation of microorganisms. *Environ Sci Technol* **40**, 6117-6122, doi:10.1021/es0604313 (2006).
- 106 Shi, X. *et al.* Understanding activity trends in electrochemical water oxidation to form hydrogen peroxide. *Nat Commun* **8**, 701, doi:10.1038/s41467-017-00585-6 (2017).
- 107 Zhou, M., Dai, Q., Lei, L., Ma, C. a. & Wang, D. Long Life Modified Lead Dioxide Anode for Organic Wastewater Treatment: Electrochemical Characteristics and Degradation Mechanism. *Environmental Science & Technology* **39**, 363-370, doi:10.1021/es049313a (2004).
- 108 Guo, L. *et al.* Advances in Selective Electrochemical Oxidation of 5-Hydroxymethylfurfural to Produce High-Value Chemicals. *Adv Sci (Weinh)* **10**, e2205540, doi:10.1002/advs.202205540 (2023).
- 109 An, J. *et al.* Revealing Decay Mechanisms of H₂O₂-Based Electrochemical Advanced Oxidation Processes after Long-Term Operation for Phenol Degradation. *Environ Sci Technol* **54**, 10916-10925, doi:10.1021/acs.est.0c03233 (2020).
- 110 Liu, C., Zhang, A. Y., Si, Y., Pei, D. N. & Yu, H. Q. Photochemical Anti-Fouling Approach for Electrochemical Pollutant Degradation on Facet-Tailored TiO₂ Single Crystals. *Environ Sci Technol* **51**, 11326-11335, doi:10.1021/acs.est.7b04105 (2017).
- 111 Song, D. *et al.* Degradation of Perfluorooctanoic Acid by Chlorine Radical Triggered Electrochemical Oxidation System. *Environ Sci Technol* **57**, 9416-9425, doi:10.1021/acs.est.3c02025 (2023).
- 112 Wenderich, K., Nieuweweme, B. A. M., Mul, G. & Mei, B. T. Selective Electrochemical Oxidation of H₂O to H₂O₂ Using Boron-Doped Diamond: An Experimental and Techno-Economic Evaluation. *ACS Sustainable Chemistry & Engineering* **9**, 7803-7812, doi:10.1021/acssuschemeng.1c01244 (2021).

- 113 Koppenol, W. H. & Butler, J. Energetics of interconversion reactions of oxyradicals. *Advances in Free Radical Biology & Medicine* **1**, 91-131, doi:10.1016/8755-9668(85)90005-5 (1985).
- 114 Schümann, U. & Gründler, P. Electrochemical degradation of organic substances at PbO₂ anodes: Monitoring by continuous CO₂ measurements. *Water Research* **32**, 2835-2842, doi:https://doi.org/10.1016/S0043-1354(98)00046-3 (1998).
- 115 Li, L. *et al.* Effect of Current Density on Preparation and Properties of TF/β-PbO₂ in MSA Media. *ACS Omega* **8**, 12062-12068, doi:10.1021/acsomega.2c07879 (2023).
- 116 Duan, X., Ma, F., Yuan, Z., Chang, L. & Jin, X. Electrochemical degradation of phenol in aqueous solution using PbO₂ anode. *Journal of the Taiwan Institute of Chemical Engineers* **44**, 95-102, doi:https://doi.org/10.1016/j.jtice.2012.08.009 (2013).
- 117 Guo, H. *et al.* How to improve lead dioxide anodes performance in organic wastewater treatment: Review and prospect. *Process Safety and Environmental Protection* **164**, 189-207, doi:https://doi.org/10.1016/j.psep.2022.06.012 (2022).
- 118 Xue, S.-g. *et al.* Selective Electrocatalytic Water Oxidation to Produce H₂O₂ Using a C,N Codoped TiO₂ Electrode in an Acidic Electrolyte. *Acs Appl Mater Inter* **12**, 4423-4431, doi:10.1021/acsomega.9b16937 (2020).
- 119 Park, S. Y. *et al.* CaSnO₃: An Electrocatalyst for Two-Electron Water Oxidation Reaction to Form H₂O₂. *ACS Energy Letters* **4**, 352-357, doi:10.1021/acseenergylett.8b02303 (2019).
- 120 Korjenic, A. & Raja, K. S. Electrochemical stability of fluorine doped tin oxide (FTO) coating at different pH conditions. *Journal of The Electrochemical Society* **166**, C169-C184 (2019).

Appendix

Chapter 2



Figure S2.1. Custom-made experimental setup for online DEMS measurements during nitrate electroreduction studies. [42]

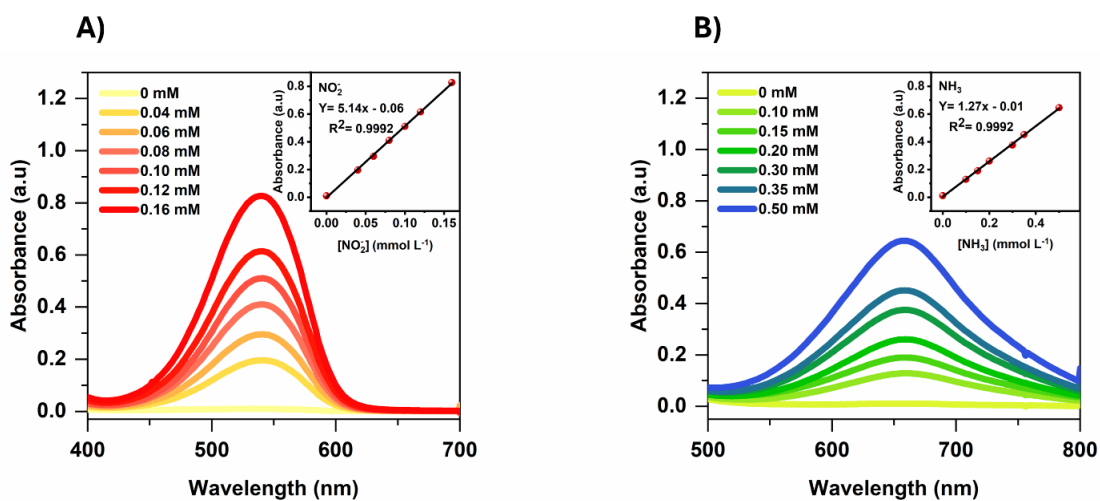


Figure S2.2. A) UV-vis spectra of NO_2^- and NH_3 quantifications. The inserts represent the linear relationship between maximum absorbance wavelength and species concentration for NH_3 at 657 nm and NO_2^- at 540 nm.

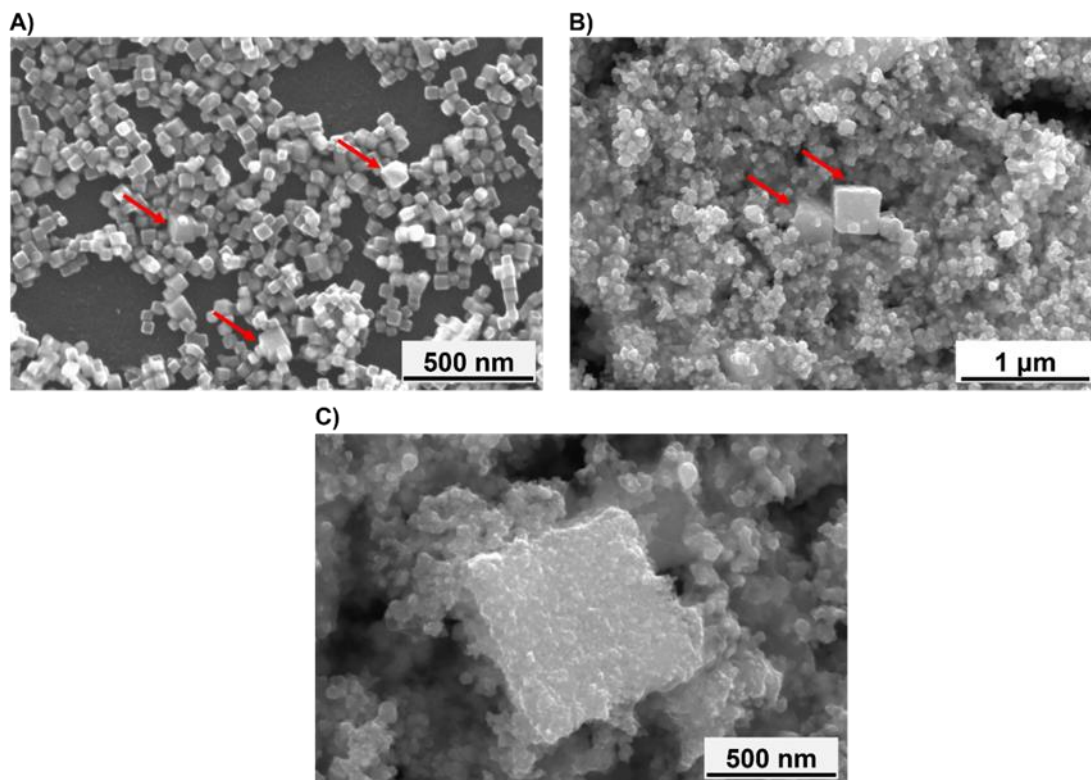


Figure S2.3. SEM images of the electrocatalyst A) before and B-C) after 1-hour of NO_3RR at -0.3 V vs. RHE in 1.0 mol L^{-1} NaOH with 14 mmol L^{-1} of NaNO_3 at medium and high magnification, respectively. The red arrows indicate larger nanocubes particles domains.

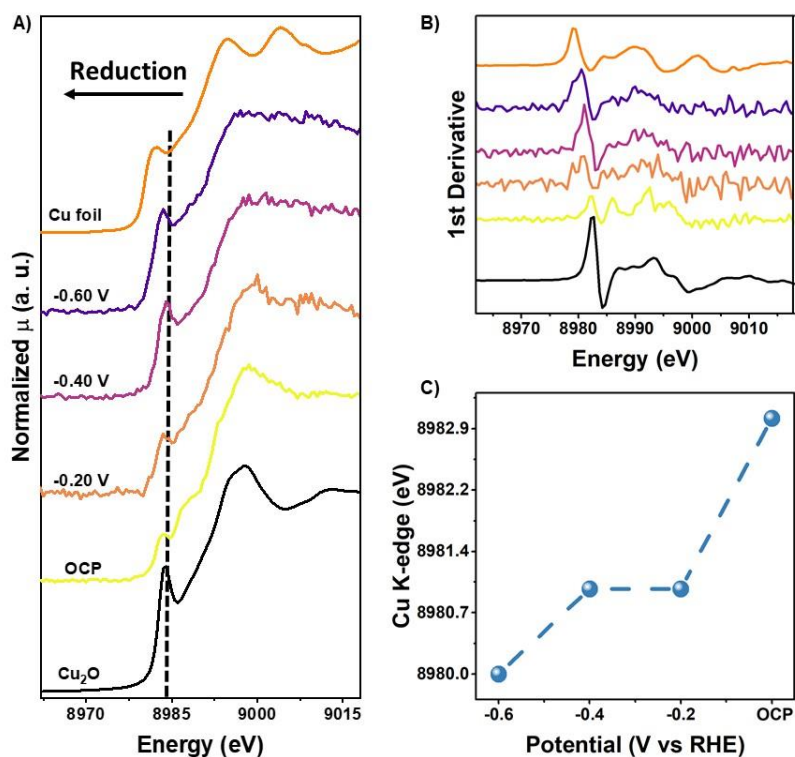


Figure S2.4. A) Normalized in situ XANES spectra of Cu_2O NCs at different applied potentials in 1.0 mol L^{-1} NaOH and 14 mmol L^{-1} , and the spectra of the standards Cu and Cu_2O ; B) the

corresponding first derivative curves of the in situ XANES spectra; and C) dependence of the Cu K-edge energy as a function of the electrochemical potential.

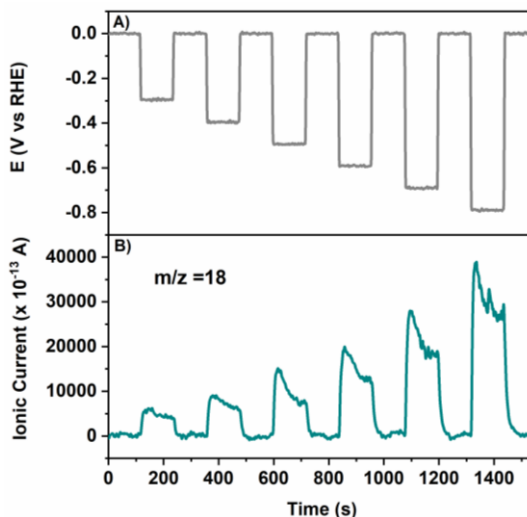


Figure S2.5. Online DEMS of Cu₂O NCs recorded in 0.1 mol L⁻¹ NaOH + 14 mmol L⁻¹ NaNO₃ electrolyte. A) Applied potential vs. time. B) Ionic current vs. time of the fragment m/z = 18 of H₂O molecules.

Chapter 3

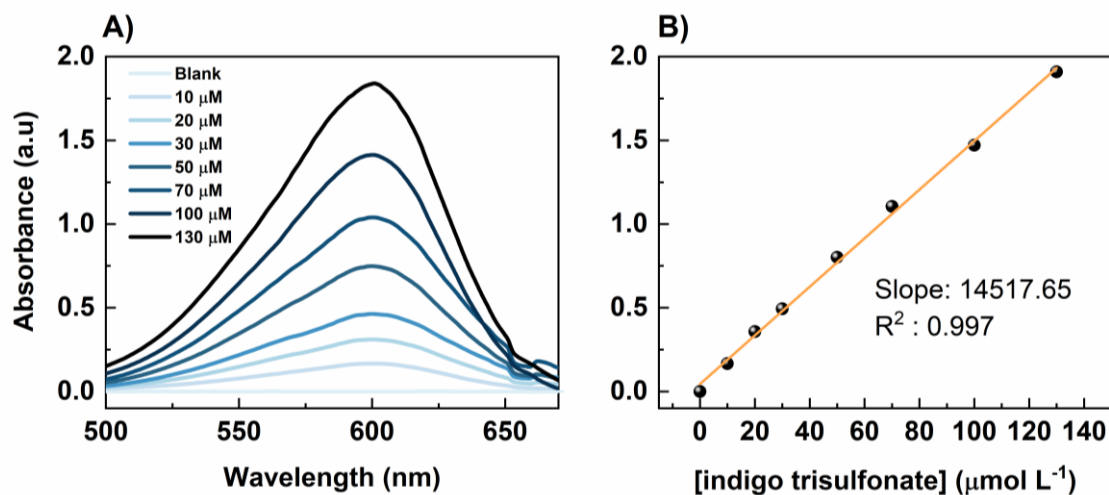


Figure S3.1. A) UV-vis spectra of Indigo calibration curve and B) representation of the linear relationship between maximum absorbance wavelength (600nm) and species concentration.

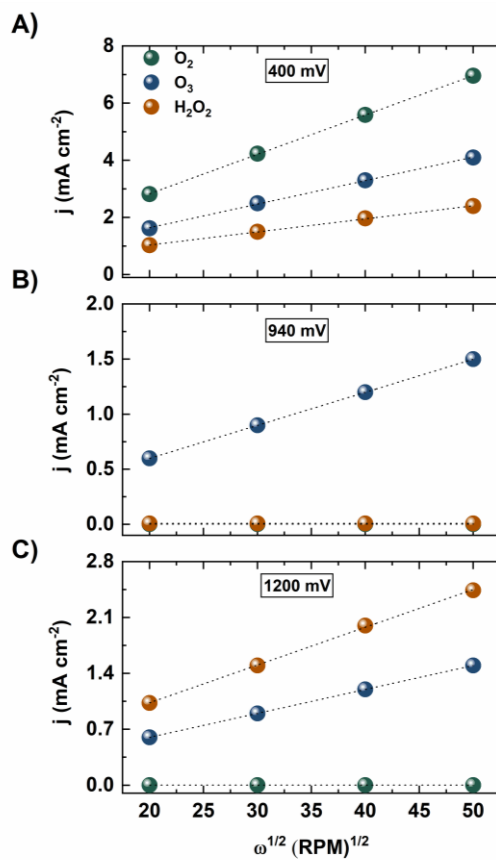


Figure S3.2. Koutecky-Levich plots for O₂, O₃ and H₂O₂ at A) 400 mV, B) 940mV, and C) 1200 mV in different rotation rates. On Pt electrode in 0.1 mol L⁻¹ H₂SO₄ electrolyte.

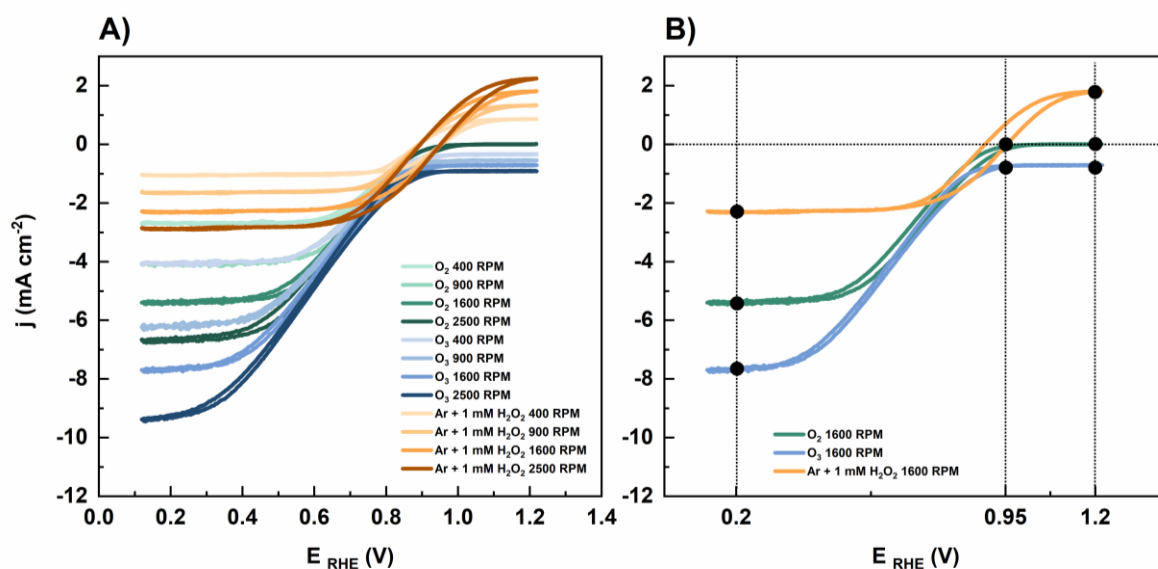


Figure S3.3. A) Cyclic voltammograms on polycrystalline Pt in O₂-saturated 0.1 mol L⁻¹ NaHCO₃ (green lines), O₃-saturated 0.1 mol L⁻¹ (blue lines) and Ar-saturated 0.1 mol L⁻¹ NaHCO₃ + 1 mmol L⁻¹ H₂O₂ (orange lines), at different rotation rates. B) highlighted current density regions at 0.4V, 0.94V and 1.2V vs RHE at 1600RPM. Scan rate: 50 mV s⁻¹.

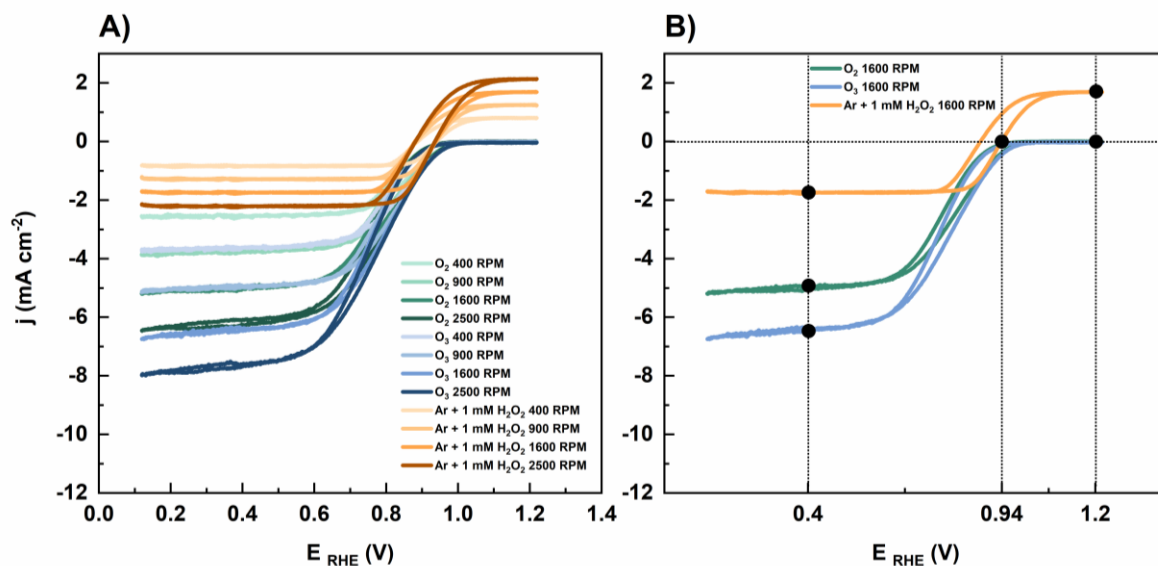


Figure S3.4. A) Cyclic voltammograms on polycrystalline Pt in O₂-saturated 0.1 mol L⁻¹ Na₂CO₃ (green lines), O₃-saturated 0.1 mol L⁻¹ (blue lines) and Ar-saturated 0.1 mol L⁻¹ Na₂CO₃ + 1 mmol L⁻¹ H₂O₂ (orange lines), at different rotation rates. B) highlighted current density regions at 0.4V, 0.94V and 1.2V vs RHE at 1600RPM. Scan rate: 50 mV s⁻¹.

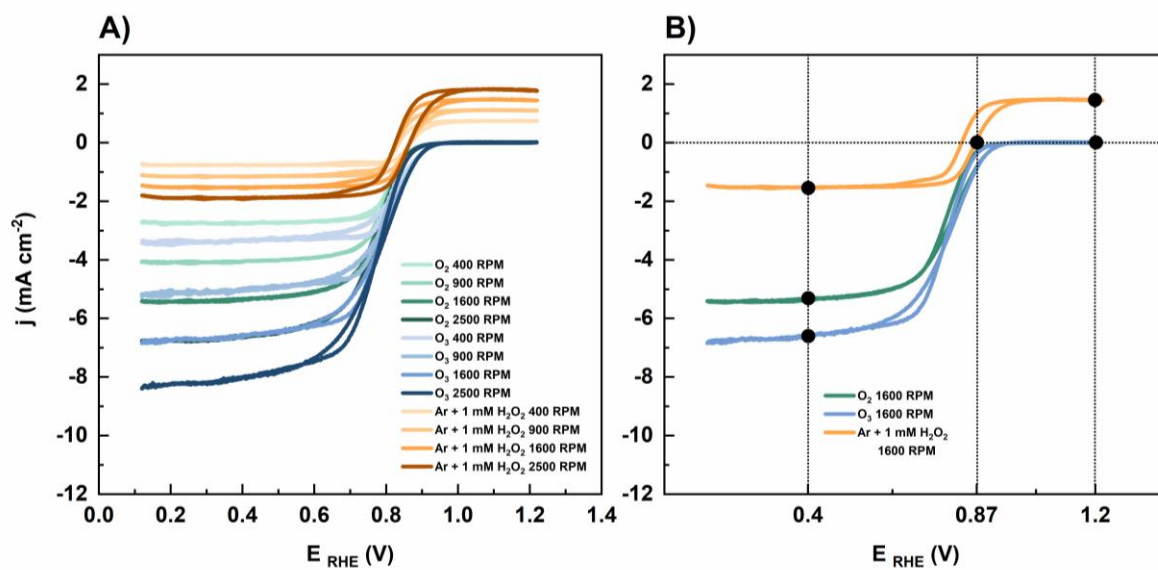


Figure S3.5. A) Cyclic voltammograms on polycrystalline Pt in O₂-saturated 0.1 mol L⁻¹ NaOH (green lines), O₃-saturated 0.1 mol L⁻¹ (blue lines) and Ar-saturated 0.1 mol L⁻¹ NaOH + 1 mmol L⁻¹ H₂O₂ (orange lines), at different rotation rates. B) highlighted current density regions at 0.4V, 0.94V and 1.2V vs RHE at 1600RPM. Scan rate: 50 mV s⁻¹.

Chapter 4

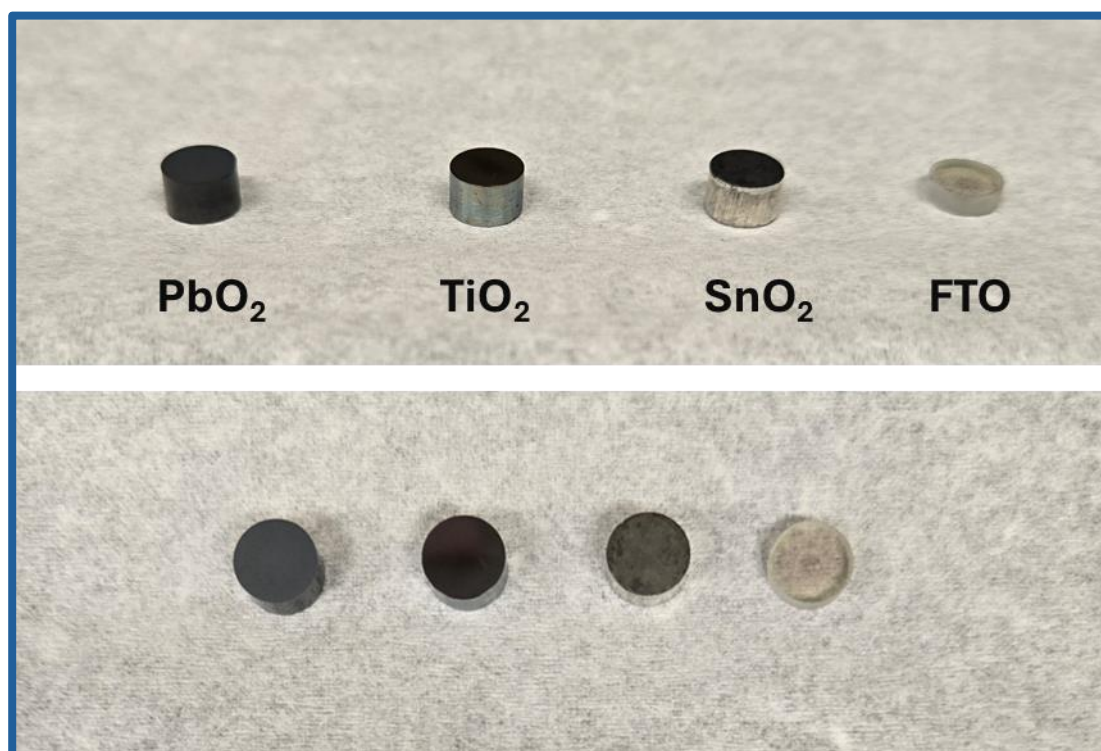


Figure S4.1. Digital images of 6mm disks electrodes, with the metal oxides layer on top of the disk substrates.

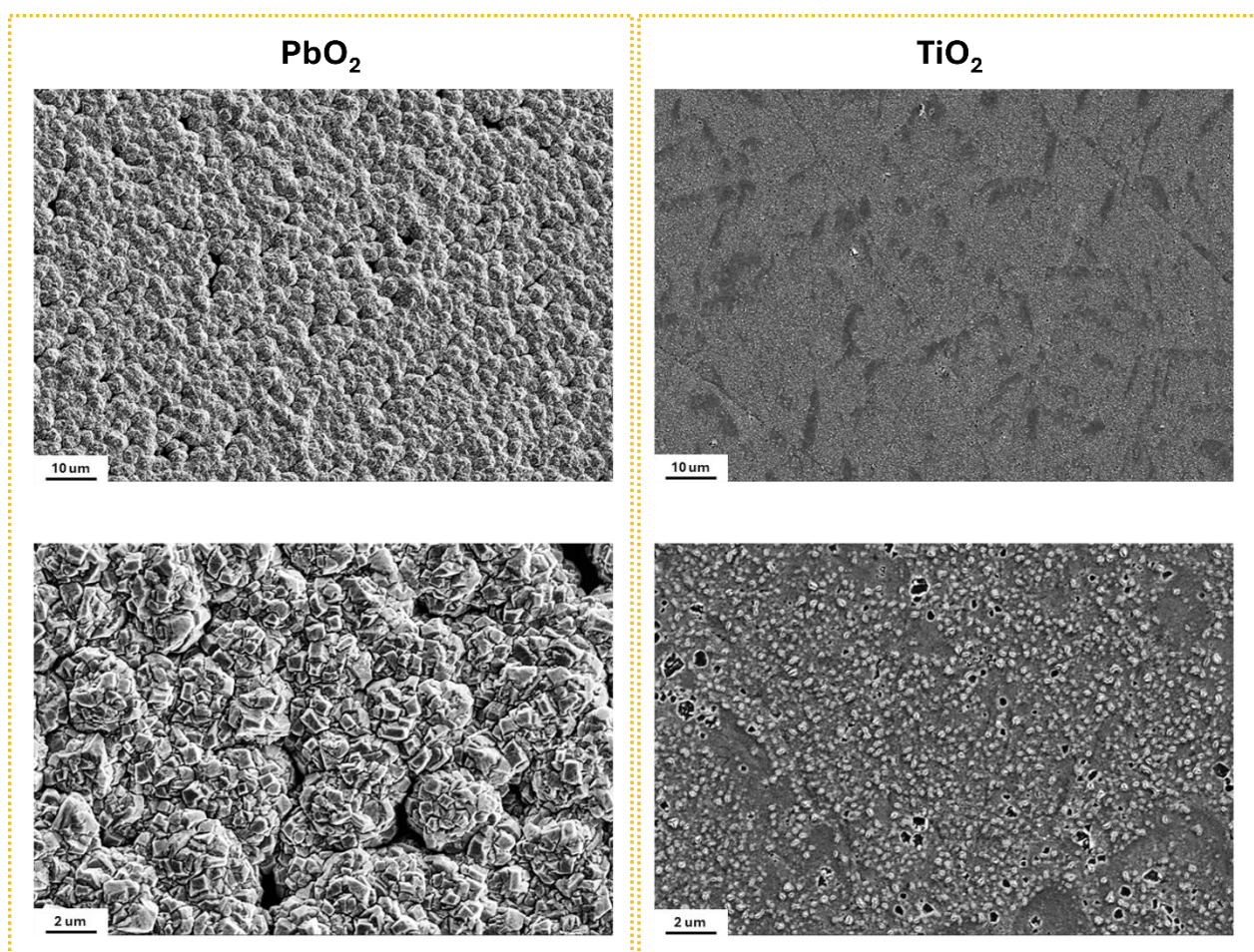


Figure S4.2. SEM images of PbO_2 on the left side and TiO_2 on the right-side surface in different magnifications.

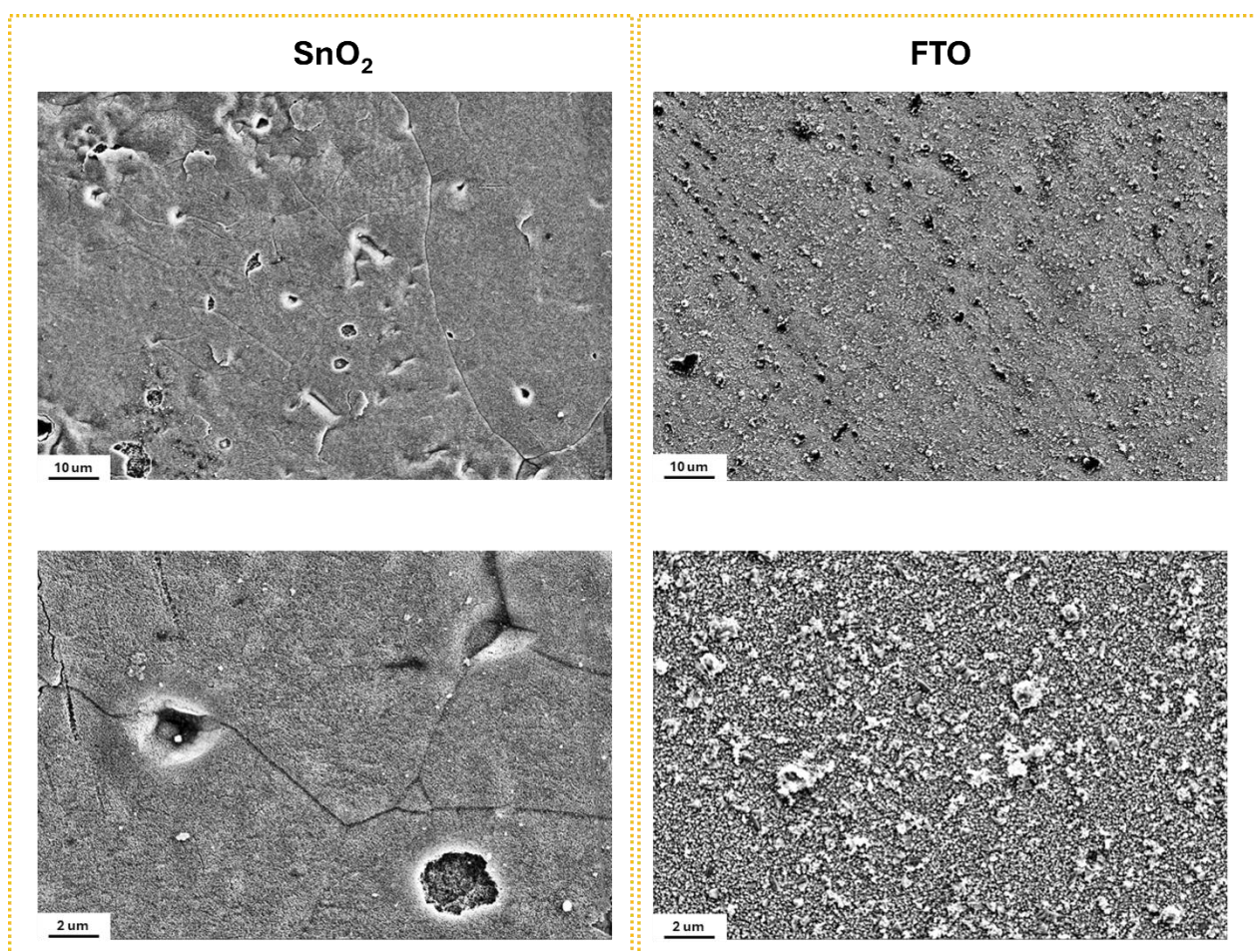


Figure S4.3. SEM images of SnO_2 on the left side and FTO on the right-side surface in different magnifications.

DECLARAÇÃO

As cópias dos documentos de minha autoria ou de minha coautoria, já publicados ou submetidos para publicação em revistas científicas ou anais de congressos sujeitos a arbitragem, que constam da minha Dissertação/Tese de Mestrado/Doutorado, intitulada “Estudo da Correlação entre Atividade e Estabilidade de Óxidos Metálicos como Eletrocatalisadores na Remoção de Contaminantes de Água” não infringem os dispositivos da Lei nº 9.610/98, nem o direito autoral de qualquer editora.

Campinas, 17 de Agosto de 2024



Autor - Igor Messias

R.G. nº 10.686-159-5



Orientador – Raphael Nagao

RG nº 283176702